

Experimental Investigation and Modelling of Bacterial Growth and Inactivation: E. coli Exposed to Laser-synthesized Silver Nanoparticles

Krce, Lucija

Doctoral thesis / Disertacija

2020

Degree Grantor / Ustanova koja je dodijelila akademski / stručni stupanj: **University of Split, Faculty of Science / Sveučilište u Splitu, Prirodoslovno-matematički fakultet**

Permanent link / Trajna poveznica: <https://um.nsk.hr/um:nbn:hr:166:803690>

Rights / Prava: [In copyright](#)/[Zaštićeno autorskim pravom.](#)

Download date / Datum preuzimanja: **2024-12-28**

Repository / Repozitorij:

[Repository of Faculty of Science](#)



University of Split
Faculty of Science
Biophysics Doctoral Programme

Lucija Krce

**Experimental Investigation and Modelling of Bacterial
Growth and Inactivation: *E. coli* Exposed to Laser-synthesized
Silver Nanoparticles**

Doctoral thesis

Split, June 2020

Sveučilište u Splitu
Prirodoslovno-matematički fakultet
Poslijediplomski sveučilišni doktorski studij
Biofizika

Lucija Krce

**Eksperimentalno istraživanje i modeliranje bakterijskog rasta
i inaktivacije: *E. coli* izložena laserski sintetiziranim srebrnim
nanočesticama**

Doktorski rad

Split, lipanj 2020.

Sveučilište u Splitu, Prirodoslovno-matematički fakultet
Odjel za fiziku, Poslijediplomski sveučilišni doktorski studij Biofizika

Experimental Investigation and Modelling of Bacterial Growth and Inactivation: *E. coli* Exposed to Laser-synthesized Silver Nanoparticles

Doktorski rad autorice Lucije Krce kao dio obaveza potrebnih da se dobije doktorat znanosti, izrađen pod vodstvom mentora prof. dr. sc. Ivice Avianija.
Dobiveni akademski naziv i stupanj: doktorica prirodnih znanosti iz polja fizika.

Povjerenstvo za ocjenu i obranu doktorskog rada u sastavu:

1. prof. dr. sc. Ante Bilušić _____

2. dr. sc. Nikša Krstulović _____

3. izv. prof. dr. sc. Marija Raguž _____

potvrđuje da je disertacija obranjena dana _____.

Voditelj studija:

prof. dr. sc. Mile Dželalija

DEKAN:

prof. dr. sc. Nikola Koceić-Bilan

University of Split
Faculty of Science

Doctoral thesis

EXPERIMENTAL INVESTIGATION AND MODELLING OF BACTERIAL GROWTH AND INACTIVATION: *E. COLI* EXPOSED TO LASER- SYNTHESIZED SILVER NANOPARTICLES

Lucija Krce

Thesis performed at:
University of Split, Faculty of Science, Croatia

Abstract

The aim of this thesis is to elaborate on the mode of antibacterial action by colloidal silver nanoparticles against *Escherichia coli* as a model organism. Two approaches were used to investigate the bactericidal mechanism of silver nanoparticles (AgNPs): experimental probing and modelling of the treated bacterial cell growth. AgNPs were synthesized by laser ablation in water and the obtained colloid was thoroughly characterized. An upgradable interaction-based growth model was developed to understand the effect of AgNPs on bacterial cell dynamics. The model explains untreated and AgNP-treated *Escherichia coli* growth in batch culture. Subsequently, fluorescence probing and atomic force microscopy and spectroscopy were used to experimentally study the AgNP bactericidal mechanism. This study shows that the mode of antibacterial action of silver nanoparticles includes penetration of AgNPs inside the cell/membrane, membrane permeabilization, reduction of the cell's Young modulus and possible cell leakage while undistinguished reactive oxygen species level was detected inside lethally treated cells.

(97 pages, 24 figures, 1 table, 130 references, 1 appendix, original in English)

Thesis deposited in:

National and University Library in Zagreb

University Library in Split

Library of the Faculty of Science, University of Split

Keywords: bacterial growth, *E. coli*, growth rate, logistic model, silver nanoparticles, antibacterial activity, modelling bacterial growth, laser-synthesized nanoparticles, mode of antibacterial action, nano-bio interactions, reactive oxygen species, atomic force microscopy, Young modulus.

Supervisor: Prof. Ivica Aviani, Ph.D.

Reviewers: 1. Prof. Ante Bilušić, Ph.D.

2. Nikša Krstulović, Ph.D.

3. Assoc. Prof. Marija Raguž, Ph.D.

Thesis accepted: 24. 6. 2020.

Sveučilište u Splitu
Prirodoslovno-matematički fakultet

Doktorski rad

EKSPERIMENTALNO ISTRAŽIVANJE I MODELIRANJE BAKTERIJSKOG RASTA I INAKTIVACIJE: *E. COLI* IZLOŽENA LASERSKI SINTETIZIRANIM SREBRNIM NANOČESTICAMA

Lucija Krce

Rad je izrađen na:

Sveučilištu u Splitu, Prirodoslovno-matematičkom fakultetu, Hrvatska

Sažetak

Cilj ove teze je razjasniti način antibakterijskog djelovanja koloidnih nanočestica srebra na stanice *Escherichia coli* kao modelnog organizma. Istraživanje baktericidnog mehanizma srebrnih nanočestica provedeno je eksperimentalnim i teorijskim metodama kako bi se čim bolje opisao rast tretiranih bakterijskih stanica. Srebrne nanočestice su sintetizirane laserskom ablacijom u vodi, a dobiveni koloid je temeljito karakteriziran. Uveden je model rasta temeljen na interakcijama kako bi se razumio učinak nanočestica na dinamiku rasta bakterijskih stanica. Model objašnjava rast netretiranih i tretiranih bakterijskih stanica u tekućoj kulturi. Za eksperimentalno proučavanje baktericidnog mehanizma nanočestica korištene su fluorescentna spektroskopija te mikroskopija i spektroskopija atomskom silom. Istraživanje pokazuje da antibakterijsko djelovanje srebrnih nanočestica na bakterijske stanice uključuje njihov prodor unutar stanice/membrane, permeabilizaciju membrane, smanjenje Youngovog modula s vremenom te moguće istjecanje unutarstaničnog materijala, dok je inducirana razina reaktivnih kisikovih vrsta u smrtonosno tretiranim stanicama zanemariva.

(97 stranica, 24 slike, 1 tablica, 130 literaturnih navoda, 1 prilog, jezik izvornika: engleski)

Rad je pohranjen u:

Nacionalnoj sveučilišnoj knjižnici u Zagrebu

Sveučilišnoj knjižnici u Splitu

Knjižnici Prirodoslovno-matematičkog fakulteta Sveučilišta u Splitu

Ključne riječi: bakterijski rast, *E. coli*, brzina rasta, logistički model, srebrne nanočestice, antibakterijska aktivnost, modeliranje bakterijskog rasta, laserski sintetizirane nanočestice, način antibakterijskog djelovanja, nano-bio interakcije, reaktivne kisikove vrste, mikroskopija atomskom silom, Youngov modul.

Mentor: prof. dr. sc. Ivica Aviani

Ocjenjivači: 1. prof. dr. sc. Ante Bilušić

2. dr. sc. Nikša Krstulović

3. izv. prof. dr. sc. Marija Raguž

Rad prihvaćen: 24. 6. 2020.

Mojim roditeljima.

ACKNOWLEDGMENTS

Tijekom izrade doktorata, mnogi su me profesori, suradnici i kolege učili i pomagali. Svima im želim zahvaliti.

Prvi među njima je moj mentor, prof. dr. sc. Ivica Aviani. Profesore, hvala što ste me učili fizici i životu. Hvala Vam što ste vjerovali u mene i hrabro se zaputili u još jedno područje fizike. Hvala što ste znali prepoznati prave smjerove tijekom našeg istraživanja, hvala Vam na svim znanjima i iskustvima koje ste mi pružili!

Hvala prof. dr. sc. Anti Bilušiću. Ante (evo, po prvi put na *ti*), tvoja su mi nesebična potpora i ulaganja pomogli nebrojeno puta tijekom mog studiranja. Od srca ti hvala!

Hvala dr. sc. Nikši Krstuloviću. Nikša, hvala što si uvijek imao vremena da hitno napraviš i pošalješ uzorke i strpljenja za moje bezbrojne telefonske pozive.

Hvala kolegama (posebno mojim prijateljima) s mog Odjela za fiziku. Velikim dijelom zbog vas na posao dolazim radosna.

Hvala Odjelima za kemiju i biologiju. Otvorili ste mi vrata svojih laboratorija, a time sam osim dobrih kolega s vremenom stekla i divne prijatelje. Matilda, doc. dr. sc. Šprung, ti si najbitnija od tih prijatelja. Hvala ti na neumornoj podršci.

Hvala prof. dr. sc. Vesni Svetličić koja me je uvela u prekrasan svijet bio AFM-a.

Hvala mojim prijateljima. Uz njih je bilo lako zaboraviti na PhD kada je trebalo.

Najvažnije, hvala mojim roditeljima, mojoj obitelji. Hvala mojoj mami koja baš uvijek sve razumije, papi koji uvijek sve čini za *svoje ženske*, seki koja je najdragocjeniji dar od mojih roditelja i baki čija je ljubav prema svojoj *dici* nemjerljiva.

Mama i pape, bez vaše nepresušne potpore, u svakom mogućem obliku, ne bi bilo ni truda ni rezultata. Ovo je zbog vas! Ovo je vaše!

Hvala svima, ovdje neimenovanima, koji su prepoznali trenutke kada mi je trebala pomoć i pružili mi je.

ABSTRACT

Silver has long been used as an antimicrobial agent. Specifically, silver nanoparticles (AgNPs) have been in the scientific spotlight due to their outstanding antibacterial properties. This study aims to elucidate the mode of antibacterial action of laser-synthesized colloidal AgNPs against *Escherichia coli* (*E. coli*) as a model organism. Laser ablation in water is used to synthesize AgNPs, which is a physical top-down green synthesis technique, and the obtained colloid is thoroughly characterized. Investigating the bactericidal mechanism of AgNPs involves two approaches: modelling treated bacterial cell growth and experimental probing. To understand the effect of AgNPs on bacterial cell dynamics, a simple upgradable interaction-based growth model is developed to explain untreated *E. coli* growth in batch culture. The novel model is described by two nonlinear mutually dependent differential equations, depicting the time evolution of bacteria and concentration of nutrients. The negative bacterium–bacterium interaction term is specific for the model and leads to population decay. The model is applied to *E. coli* growth curves obtained by optical density measurements for different inoculum sizes and nutrients concentrations. The proposed model comprehensively describes experimental growth curves and, due to universality of the equations, can be applied to other bacterial strains. Further development of this model facilitates studying the effects of AgNPs on bacterial cells in liquid culture. The most significant effect of AgNPs treatment on a bacterial population is an increase in apparent bacterial lag time. This is well described by the further-developed growth model as are entire growth curves for different treatment concentrations. The main assumption of the model is that the treated bacteria uptake the nanoparticles and become inactivated, resulting in a decrease of both nanoparticles and bacteria concentration. Lag time assumes an infinitive value for lethal treatment and this growth phase is not postponed bacterial growth. The model proves that the lag phase is a dynamic state where bacterial growth and death rates have proximate values. Results strongly suggest that the predominant mode of antibacterial action from laser-synthesized AgNPs is membrane penetration. Experimental probing of the AgNPs bactericidal mechanism mostly involves fluorescence data acquisition and processing, as well as atomic force microscopy and spectroscopy. Spectrofluorometry is used to obtain the time development of reactive oxygen species (ROS) inside AgNP-treated bacterial cells. An integrated atomic force and fluorescence microscopy system is used in the study of cell morphology, the Young modulus, viability and integrity before and during treatment. Lethal treatment shows that not all bacterial cells are permeabilized with cells mostly retaining their morphology and indicating cell lysis. The Young modulus of untreated cells exhibits a distinctly bimodal distribution. The softer parts of the untreated cells are randomly distributed, whereas treated cells exhibit an exponential softening of stiffer parts over time. AgNPs and bacteria show a

masking effect on the raw ROS fluorescence signal via absorbance and scattering and the contribution of cellular ROS resolved from the total fluorescence signal.

Overall, this study shows that the laser-synthesized-AgNP mode of antibacterial action includes penetration of AgNPs inside cell membranes, membrane permeabilization, time-dependent cell softening and possible cell leakage, with insignificant ROS levels detected inside lethally treated cells.

PUBLICATIONS

The following publications constitute the main part of the thesis:

- [1] Krce L, Šprung M, Maravić A, Aviani I. A simple interaction-based *E. coli* growth model. *Phys Biol* 2019;16:066005. <https://doi.org/10.1088/1478-3975/ab3d51>.
- [2] Krce L, Šprung M, Maravić A, Umek P, Salamon K, Krstulović N, Aviani I. Bacteria Exposed to Silver Nanoparticles Synthesized by Laser Ablation in Water: Modelling *E. coli* Growth and Inactivation. *Materials (Basel)* 2020;13:653. <https://doi.org/10.3390/ma13030653>.
- [3] Krce L, Šprung M, Rončević T, Maravić A, Čikeš Čulić V, Blažeka D, Krstulović N, Aviani I. Probing the Mode of Antibacterial Action of Silver Nanoparticles Synthesized by Laser Ablation in Water: What Fluorescence and AFM Data Tell Us. *Nanomaterials* 2020;10:1040. <https://doi.org/10.3390/nano10061040>.

CONTENTS

I.	INTRODUCTION.....	1
1.	General Concept.....	1
2.	Antimicrobial Resistance.....	3
3.	Antibacterial Activity of Nanoparticles.....	4
4.	Production and Characterization of Silver Nanoparticles.....	5
4.1.	LAL in liquids.....	6
4.2.	Characterization of AgNPs.....	6
5.	Modelling Untreated and Treated <i>E. coli</i> Growth and Inactivation.....	8
6.	Proposals Concerning the Silver Nanoparticle Mode of Antibacterial Action.....	9
6.1.	Atomic force microscopy of AgNPs-treated cells.....	11
6.2.	ROS detection.....	12
7.	Aims and Scopes of the Study.....	13
8.	References.....	15
II.	A SIMPLE INTERACTION-BASED <i>E. COLI</i> GROWTH MODEL.....	27
III.	BACTERIA EXPOSED TO SILVER NANOPARTICLES SYNTHESIZED BY LASER ABLATION IN WATER: MODELLING <i>E. COLI</i> GROWTH AND INACTIVATION.....	42
IV.	PROBING THE MODE OF ANTIBACTERIAL ACTION OF SILVER NANOPARTICLES SYNTHESIZED BY LASER ABLATION IN WATER: WHAT FLUORESCENCE AND AFM DATA TELL US.....	64
V.	CONCLUSIONS.....	85
VI.	APPENDIX.....	88
	SUPPLEMENTARY MATERIAL TO CHAPTER II.....	88
	SUPPLEMENTARY MATERIAL TO CHAPTER III.....	93
	CURRICULUM VITAE.....	95
	PUBLICATION LIST.....	96

I. INTRODUCTION

1. General Concept

Silver has long been known to provide antimicrobial activity. Throughout history, it has been used as a major therapeutic agent for a variety of medical purposes, mostly empirically before the discovery that infections were caused by microbes.

The underlying interest of this thesis is antibacterial activity of silver colloids, mixtures in which microscopically dispersed insoluble or soluble silver nanoparticles (AgNPs) are suspended through another substance. Silver nanoparticles are particles of Ag with a 1 to 100 nm size range [1]. Silver colloids became the mainstay of antimicrobial treatment in the first part of the 20th century until the introduction of antibiotics in the early 1940s [2]. Silver is generally used in a silver nitrate form when requiring an antibacterial effect. However, there is a meaningful increase in the surface area available for a microbe to be exposed to when silver nanoparticles are used [3]. Therefore, the bactericidal effect of AgNPs should be attributed to them being made of silver but also their nano-nature. An overview of the antibacterial effect of nanoparticles in general is given in the third section of the Introduction.

A reasonable presumption is all research into antibacterial substances is a response to the ongoing global resistance crisis. This specific issue will be briefly addressed in the second section of the Introduction. Hence, antimicrobial resistance is an excellent motive to gaining an understanding of the modes involved in antibacterial action of compounds, particularly silver colloids.

Nowadays, thousands of commercially available silver-colloid-based products for numerous and diverse purposes are available. These products are, however, often introduced without careful characterization of the colloids and thorough biocompatibility evaluation. Each possible application requires cautious consideration of the biological activity and potential toxicity of AgNPs, as well as rigorous quality, efficacy, and safety evaluation of final AgNP-enabled materials complying with the Safe-by-Design approach [4]. Rightly so, there is justified global concern regarding the toxicity of AgNPs [5] and engineered nanomaterials [6,7].

Although silver-based products (even for human consumption) are commercially available, scientific community has still not reached uniform agreement on the mode

of antibacterial action of AgNPs. This issue, and limitations for reaching a general consensus, will be evaluated in the sixth section of the Introduction. The study of physical, chemical and bio-compatible properties of AgNPs covers numerous fields of natural sciences and research results. Searching the Web of Science database for silver nanoparticles provides a list of almost 75 000 scientific papers (this result was obtained in June 2020.). Notably, AgNPs attract attention not only because of their antibacterial activity, but also due to their optical and surface properties with potential applications in bio-imaging, drug delivery and sensing. The annual number of published studies is growing each year, and almost 9 000 papers on this topic were published in 2019. Searching the Web of Science database for silver nanoparticles and antibacterial topics yields almost 13 000 results, and is continually increasing annually with almost 2 400 papers published just in 2019. Therefore, the field of researching AgNPs is active and fruitful, even though silver-based products are widely available to the public for purchase.

The main motivation of this research is to elucidate the antibacterial mechanism of laser-synthesized silver colloids against *Escherichia coli* (*E. coli*) as a model organism. Understanding this mechanism requires thoroughly researching two initial systems: growth/inactivation of viable *E. coli* culture, and the physical and chemical properties of produced colloidal silver. The former is done via modeling bacterial growth in batch cultures and is discussed in the fifth section of the Introduction. The latter is closely related to a colloid production method and is discussed in the fourth section of the Introduction. Understanding each of these systems leads also to understanding biophysical interactions resulting from adding colloids to a bacterial cell culture. This will be done primarily by applying the principles of physical science in modelling bacterial growth and inactivation, including interpretation of experimental results. To properly position the results and conclusions in this study, current proposals on the mode of antibacterial action will be given in the fifth section of the Introduction.

In summary, the introduction addresses the motive, provides a short overview of the antibacterial activity of nanoparticles in general, characterization and production of silver colloid, modelling of bacterial growth and finally the so-far proposed antibacterial mechanisms.

Novel scientific contributions from this study will be outlined at the end of the Introduction.

2. Antimicrobial Resistance

There is a link between antibiotic consumption and bacterial resistance. This resistance is independent of any demographic variables, i.e., the consumption of antibiotics creates resistance for diverse groups of people [8]. Generally, the global bacterial resistance crisis has been attributed to the overuse and misuse of antibiotics, as well as a lack of novel drug development by the pharmaceutical industry [9]. There is a wide range of biochemical and physiological mechanisms that might be responsible for the onset of resistance [10]. The development of generations of antibiotic-resistant microbes, and their distribution in microbial populations, are the results of many years of constant selection pressure from human underuse, overuse, and misuse of antibiotics. It has been argued that this is not a natural process but has been superimposed upon nature [11]. On the other hand, the development of antibiotic resistance is viewed as a normal adaptive response and an evident manifestation of Darwin's principles of evolution [12]. Antibiotic resistance is regarded as a natural phenomenon, given that bacteria have long been evolving to resist the action of natural antibacterial products [13]. However, the occurrence of increasing antibiotic resistance over the last few decades is incomparable to what happened during the evolution of microbes over several billions of years. Contemporary selection pressure from antibiotic use and disposal is much more intense [10].

Whatever the cause of the antimicrobial resistance, a continuous supply of new classes of antibiotics, not affected by known or existing mechanisms of resistance, is essential [14]. It is vital that the search for new antimicrobial agents should not be lessened [10]. The problem posed by bacterial resistance, in terms of the synthesis of novel antibacterial agents and mode of action determination, requires the involvement of numerous scientific fields, including physics and its underlying methods.

Silver has long been used as an antimicrobial agent [2]. The scientific community has retained an interest in silver nanoparticles (AgNPs), mostly due to their outstanding antibacterial property. They have been proven to provide a synergistic effect on the antibacterial potential of antibiotics [15,16] and are increasingly used for antimicrobial coating [4]. Antimicrobial resistance, as a global health problem [17], has been and continued to be an excellent motivator in researching antimicrobial activity of silver compounds, especially silver nanoparticles [18–22]. The numerous promising results on the antibacterial effect of AgNPs, evident in literature, emphasizes the need for thorough characterization of used AgNPs and gaining an understanding of their mode of antibacterial action.

3. Antibacterial Activity of Nanoparticles

Lively interest in nanoparticles (NPs) has been led by the onset of drug-resistant bacteria and increasing rate of hospital infection outbreaks, especially due to the fact that NPs might actually prevent microbial drug resistance in certain cases. Parameters such as particle size, shape, surface area, doping modification, surface roughness, zeta potential, environmental conditions, surface curvature and the producing material, all affect the antibacterial mechanism and activities [23]. NPs have been utilized as antibacterial agents for coating implantable devices, wound dressings, bone cement and dental materials, while other applications include NP-based antibiotic delivery systems [23]. The high surface-area-to-volume ratio of nanoparticles gives them different physical and chemical characteristics in comparison to bulk material or larger particles [24]. Heavy metals, classified as metals with a density higher than 5 g/cm³, are almost exclusively used for the production of antimicrobial metallic NPs [25]. These metals tend to be transition elements, meaning that their electron configuration has the d orbital of the atom partially filled, which is important because a partially filled d orbital means that these metals are generally more redox active, facilitating NP formation [25]. The bactericidal effect of transition metal NPs is attributed to numerous properties, notably their affinity to associate with R-SH groups (thiols), but the most important is the ability to generate reactive oxygen species (ROS). Heavy metal ions, such as Ag⁺ or Hg²⁺, easily bind to SH groups which directly disrupts the functioning of specific enzymes or breaks S-S bridges necessary in maintaining the integrity of folded proteins, thus causing harmful consequences to cell metabolism [25]. The antibacterial mechanism depends on physical and chemical properties of NPs, but oxidative stress induced by ROS is one of the most prominent and important mechanisms. ROS is a generic term for molecules (such as the superoxide radical, hydroxyl radical, hydrogen peroxide and singlet oxygen) that have a strong positive redox potential. Under normal circumstances, production and clearance of ROS in bacterial cells are balanced [23]. In contrast, during excessive ROS generation, the redox balance of cells favors oxidation. This unbalanced state produces oxidative stress, which damages components in bacterial cells. Different types of NPs produce different types of ROS [23].

Gold NPs do not generate ROS. They exert antibacterial activity by changing the membrane potential and inhibiting ATP synthase, leading to a general decline in metabolism. Also, the effect is evident in the inhibition of ribosome subunits for tRNA binding, which indicates a collapse of biological processes [26]. Bimetallic AuPtNPs induce ruptures in the bacterial inner membrane and do not stimulate an increase in ROS levels [27]. On the other hand, the antibacterial mechanism of copper-bearing titanium alloys includes a disruption of respiratory chains caused by the release of Cu ions, which subsequently increases ROS levels. The released Cu ions impede the gene

replication process, while bacterial morphology changes due to membrane leakage [28]. The bacterial toxicity of graphene oxide is attributed to both membrane and oxidative stress [29].

Metal oxide nanoparticles induce diverse response in bacterial cells [30,31]. ZnONPs treatment of bacterial cells induces a higher intracellular ROS level. Moreover, the release of Zn^{2+} ions and adhesion to cell membranes causes mechanical damage to the cell wall [32]. Titanium dioxide nanoparticles induce changes in the bacterial outer membrane protein expression [30]. Evidence shows that MgO and CaO nanoparticles damage cell membranes, subsequently leading to leakage of intracellular matter and subsequent death of the bacterial cell [31]. The process involves CuO nanoparticles entering the bacterial cell and then damaging the vital bacterial enzymes [31]. Silicon nanoparticles exhibit an antibacterial property by influencing cell functioning in terms of cell differentiation, adhesion and spreading [31].

4. Production and Characterization of Silver Nanoparticles

Many metallic and metallic oxide NPs show bactericidal potential towards different bacterial strains [24], but silver nanoparticles attract the most attention partially due to the antimicrobial activity of Ag^+ ions. Silver nanoparticles have been proven to be an excellent antibacterial agent against gram-negative bacteria and a mild antibacterial agent against gram-positive bacteria, possibly due to differences in their membrane structure [20]. They are widely available for purchase or are chemically produced [33–35]. Chemical synthesis methods have been commonly applied in synthesizing metallic NPs as a colloidal dispersion in aqueous solutions or organic solvents by reducing their metal salts. AgNPs are chemically produced mainly in Brust–Schiffrin synthesis or using the Turkevich method. When synthesizing metallic NPs of a specific shape, size, and optical properties, the strength and type of reducing agents and stabilizers should be taken into consideration [36]. Most reports on the antibacterial effect of AgNPs refer to chemically synthesized colloids, but this type of production results in colloids containing unwanted chemical byproducts. Eco-friendly alternatives exist, such as biosynthesis with bacteria, fungi, or plant-related parts [22]. Green-synthesized nanoparticles exhibited a narrow size distribution, antioxidant activity and high antibacterial activity versus chemically synthesized ones which have a wider size distribution, no anti-oxidant activity and less antibacterial activity [37]. However, one of the most convenient techniques is the physical production of colloids by using laser ablation in liquids (LAL) [38], and there are significantly less reports on the bactericidal effect of nanoparticles produced by LAL [39–42]. This technique, known as a green synthesis technique [43], though other types of synthesis are also considered to be green [44], enables the production of pure colloids without

byproducts and stabilizing molecules but with unique surface properties [45,46]. This is extremely important when trying to elucidate the NP mode of antibacterial action.

4.1. LAL in liquids

The silver colloids used in this research were produced by a laser ablation process where the silver target is immersed into water [47]. The physics behind laser ablation in liquids, a synthesis method for producing AgNPs, is beyond the scope of this study, but some of the features of the production method will, nonetheless, be addressed.

In past years, LAL emerged as a reliable green alternative to traditional chemical reduction methods for obtaining noble metal nanoparticles in water or organic solvents [45]. AgNP synthesis based on pulsed laser ablation in liquid facilitates the preparation of stable silver colloids in pure solvents without the use of capping or stabilizing agents, producing AgNPs more suitable for biomedical applications than those prepared using common wet chemistry preparation techniques [42]. LAL is a physical approach to the top-down synthesis of nanomaterials, complementary to bottom-up chemical reduction methods. Also, the LAL technique provides good reproducibility while NPs are obtainable, without any ligands or stabilizers, in a variety of solvents [45]. Since any metal target can be ablated, LAL is not limited to a choice of materials.

Biomedical applications of NPs are often complicated due to possible toxicity of conventional nanomaterials, resulting from inadequate procedures for purifying nanoparticles obtained from synthetic pathways using toxic or non-biocompatible substances [43]. The microscopic, physical and chemical properties of AgNPs are closely related to experimental preparation procedures, interaction of metal ions with reducing agents, as well as adsorption of stabilizers [48]. In addition, attributes such as the size, optical properties and stability of AgNPs have been shown to be solvent-dependent [49]. Therefore, the production method as well as these physical and chemical properties of NPs are crucial for their antibacterial effect and mechanism.

LAL is used to prepare metal nanomaterials in clean, biologically friendly aqueous environment and thus resolves the additional toxicity problem [43]. This method produces stable metal colloids of extremely small size (at a scale of 1 nm) with a unique surface chemistry, and can be used for bio-imaging, cancer treatment and nanoparticle-enhanced Raman spectroscopy [43].

4.2. Characterization of AgNPs

Physical and chemical properties of AgNPs have been shown to play a significant role in the mode of antibacterial action. Therefore, thorough characterization of the LAL-synthesized AgNPs is required, leading to the introduction of commonly used

experimental techniques. These techniques provide information on nanoparticle size (distribution), concentration, stability, composition and structure.

Dynamic light scattering (DLS) and zeta potential measurements are simple, easy and reproducible tools to ascertain particle size and surface charge respectively [50]. Electrophoretic light scattering has emerged as a fast and convenient technique for obtaining the zeta potential, the potential at the slipping/shear plane of a colloidal particle [50] which is considered to be a measure of the electrokinetic charge of a particle [51]. The zeta potential of a nanoparticle is generally accepted as a measure of its stability [42] and for suspensions that are stabilized by electrostatic repulsion, the zeta potential should be at least ± 30 mV [52]. Particles in a colloid dispersion scatter incident light, and the DLS technique is used to detect the intensity of scattered light. The nanoparticles are in thermal motion within the dispersion, which causes constructive and destructive interferences, hence the intensity of scattered light changes over time [50]. The dynamics of the NPs is determined by comparing intensity values in two close moments. This technique is mostly used to determine the size distribution of NPs, confirm surface functionalization and determine long term stability in different media or pH values [53].

Transmission electron microscopy (TEM) analysis and UV-visible spectroscopy are usually exploited for obtaining information on nanoparticles synthesis results [45]. The interaction of light with the conducting electrons in a gold or silver nanostructure causes collective excitations known as surface plasmons [54]. UV-visible spectroscopy is a fast technique for characterization of nanoparticle shape and size. Generally, the presence of a sharp plasmon band close to 400 nm is proof that spherical AgNPs have been produced [45]. This cheap technique can be used to verify temporal stability of produced colloids. UV-visible spectroscopy of plasmon bands can also be used to monitor surface coverage of metallic NPs [45]. TEM modus operandi resembles that of a transmission light microscope [55]. It is a technique that exploits the interaction of accelerated electrons with the specimen and provides morphological, compositional, and crystallographic information [56]. Electron and atomic force microscopies are often used to determine the shape of AgNPs, particularly TEM which is also used to determine size (distribution), structure and shape [35,49,57,58]. In comparison, atomic force microscopy is seldom utilized, but the technique can provide shape [37,39] and size information where the former yields size distribution. NPs size distribution yielded by atomic force microscopy (AFM), is obtained by measuring the height of AgNPs (equal to the nanoparticle's diameter) since lateral dimensions are not to be taken into account due to AFM tip dilation [59]. More information on this technique will be given in the sixth section of the introduction. Finally, the possible crystalline nature and composition of nanoparticles is usually characterized using X-ray diffraction [22,39,60–63]. This characterization method is based on the X-rays diffraction by specimen periodic atomic planes and the angle or energy-resolved detection of the diffracted signal [64].

5. Modelling Untreated and Treated *E. coli* Growth and Inactivation

Bacterial growth consists of four distinct and commonly accepted phases: lag phase, exponential growth phase, stationary phase and mortality phase [65]. All stages of growth may not necessary be obtained in a growth curve, and this depends on experimental circumstances [66–68]. These stages are clearly distinguished on a growth curve which has a bacterial concentration time-dependency. A growth curve provides information on the total number of bacteria in a batch, average division time, state of bacterial metabolism and the phase at which the inoculum was taken. Different modeling strategies are used to understand the underlying mechanisms of growth, especially in interpreting data obtained under different growth conditions. The most commonly used models include the Gompertz function and its modifications [69,70], or the rate logistic (Verhulst) model [65] and its modifications [66,71]. The purely empirical Gompertz function does not provide any mechanistic insight into growth. On the other hand, the logistic model seems more intuitive given that bacterial growth is described using a differential equation. However, it only explains the exponential and stationary phase [66]. These two common models are used to fit growth curves of standard bacterial strains grown in batch culture and in food microbiology [71–73]. Buchanan et al. [74] proposed a three-phase linear model, consisting of three equations, using a physiological approach and taking into account biological variability. The downside of this model is that it describes each of the first three growth phases using a different equation. Modeling microbial growth kinetics based on a substrate concentration was first introduced by Monod [75]. He proposed that the cell division rate depends on the substrate concentration, thus forming a curve described using a Michaelis-Menten type of equation. The idea in describing the influence of resources availability and waste on the growth of a population, was also introduced by S. Sakanoue [76]. The death phase is usually given as a mirror image of growth, when depicting bacterial growth [65]. Peleg and Shetty proposed that a combination of the logistic growth and Fermi decay provide a model for the entire growth curve of certain microbes [77]. Bacterial death was also described by introducing a constant rate decay term into the model equations [78]. An overview of the models given in [79,80] includes a series of mathematical equations that model only the inactivation process in bacterial curves. Some of the proposed models include numerous parameters and give a description only for the death phase in a mathematically complex way.

The lag phase, a delay of exponential growth due to altered growth conditions, has been the center of attention in many primary growth models [81–83]. The Baranyi model [84,85] describes lag time in terms of cell adjustment to its new post-inoculum environment. Hills and Mackey [86] associated this phase with delayed biosynthesis of an essential growth factor and cell injury/resuscitation. This phase also seems to be induced when bacteria are treated using different sub minimal inhibitory

concentration (MIC) values of antibacterial substances [87–90], including silver ions and silver nanoparticles [35,91–93]. Scarce attempts have been made in modeling bacterial growth in the presence of silver nanoparticles [63,94]. The study published by Chatterjee et al. [94] introduced a modified Gompertz model for bacterial isothermal growth data obtained at various AgNPs concentrations but without any interpretation at a microscopic level.

Understanding the relevant parameters for untreated-bacteria growth is vital in understanding and explaining the effect that AgNPs treatment has on a bacterial population. If this is done by modelling, the model should be designed in a mechanistic fashion, i.e., it should not just be a mathematical description of the growth curve. Developing a model for growth and inactivation of viable *Escherichia coli* (*E. coli*) cells assists in understanding the bactericidal mechanism of laser-synthesized AgNPs.

6. Proposals Concerning the Silver Nanoparticle Mode of Antibacterial Action

The mode of antibacterial action of AgNPs has still not been resolved [95] and more research on the bioactivity and biocompatibility of AgNPs is necessary [96], but it has been stated that silver ions play a crucial role in the antibacterial activity of silver [18] given that many proposed mechanisms incorporate the release of silver ions upon dissolution of AgNPs [3,18,97–99]. Silver cations have a profound ability to interact with and bind proteins and anions in a medium [100]. The released silver ions from AgNPs interact with the thiol groups of many enzymes and causing them to inactivate. Furthermore, cells can up-take these ions possibly inhibiting several functions in cells while ROS are possibly produced due to ion inhibition of respiratory enzymes [3]. Generally, the mode of antibacterial action for AgNPs is attributed to the fact they are silver and a nanomaterial.

It has been shown that treatment using silver cations alone induces morphological changes both in gram positive and gram negative bacterial cells [101]. Morones-Ramirez et al. [102] showed that sub-lethal silver cation concentrations induce morphological changes in bacterial membranes and protein aggregation, while membrane permeability and ROS generation are triggered at inhibitory and lethal silver concentrations. It has been noted that AgNP generation of ROS is linked to the release of silver ions [38], whereas no significant difference in silver ion toxicity towards bacteria has been observed between anaerobic and aerobic conditions, which rules out oxidative stress induced by ROS as an important antibacterial mechanism for silver ions [103]. A particle-specific antibacterial potential, manifested in an increased intracellular concentration of Ag ions, has been previously reported as the main mechanism of AgNPs in combating bacteria [104]. Then again, Xiu et al. [97] reported that antimicrobial activity of AgNPs is solely due to the release of Ag ions and particle

properties that affect toxicity towards bacteria are to be interpreted as an influence on the rate, extent, location, and/or timing of Ag ion release. Interestingly, concentrations of silver ions are 10 times lower in laser-synthesized colloids than in chemically produced colloids, but these colloids reveal similar antibacterial activity [40]. This indicates that besides Ag ions, AgNPs also play an important role in the antibacterial mechanism. It has been shown that AgNPs cause more damage than do Ag ions [105]. Furthermore, it has been shown that Ag NPs toxicity towards bacteria is mediated on a large scale by dissolved Ag ions, but the way in which the particles interact with bacterial cells and some of the pathways involved in toxicity of the particles are highly dependent on nanoparticle physicochemical properties, i.e., toxicity mechanisms in *E. coli* vary for silver nanoparticles and differ from ionic silver [106]. These, sometimes opposite and contrary results, demonstrate the need for thorough characterization of the colloidal silver as an independent system and stability checks when added to the culture.

It has been reported that the mode of antibacterial action of AgNPs is size dependent: the bactericidal effect of AgNPs smaller than 10 nm is due to the nanoparticles, but the predominant mechanism of larger ones might be the release of silver ions [107]. Their bactericidal effect depends on their size [19], concentration [33], shape [18] and surface properties [106]. For coated silver nanoparticles, antimicrobial effects were found to be an interplay of the AgNPs size, solubility, and surface coating [108]. Also, AgNPs tend to attach to cell walls and subsequently penetrate them, causing permeability of cell membranes and ultimately cell death [3], with reports on the formation of pits in cell walls due to nanoparticle accumulation [46].

As suggested in a recent review paper [109], there are two main hypotheses for the AgNP mode of antibacterial action. The first hypothesis relies on the electrostatic interaction of nanoparticles with bacterium membrane and/or membrane proteins, leading to partial membrane dissolution. The second hypothesis presumes the penetration of AgNPs inside the cell/membrane and subsequent release of silver ions, followed by an increase of ROS levels and cell oxidative stress. The two scenarios are not necessarily mutually exclusive [109]. Notably, Durán et al. [107] stated that AgNPs exhibit antibacterial activity through the cell membrane disruption and DNA transformation due to ROS, but that data on the temporal resolution of ROS production or possible membrane alterations induced by the AgNPs is lacking. Taken together, it is reasonable to say that AgNP adhesion to and/or penetration inside cells and ROS generation are recognized as the most significant modes of antimicrobial action [110], whether or not they include the release of silver ions.

There are many experimental methods for probing the antimicrobial mechanism of AgNPs, and here only a few, important for this research, will be discussed.

6.1. Atomic force microscopy of AgNPs-treated cells

Microscopy techniques are rather useful as they reveal membrane alteration caused by AgNP treatment. Electron-microscopy is most often used but the technique requires complicated sample preparation and cells are not able to be inspected in the native cell environment. Published results on AgNP-treated cells imaged by electron-microscopy reveal gaps in cell membranes and the disorganization of entire cells [93], an accumulation of nanoparticles in membranes, cell penetration and the leaking of intracellular substances [33], nanoparticles have been found on cell surfaces and attached to substances released by cells [111]. In particular, TEM images of *E. coli* treated with LAL-synthesized AgNPs have revealed that nanoparticles penetrate cells membranes during which cells showed an irregular appearance [40].

On the other hand, as a valuable tool in biophysics, atomic force microscopy facilitates the study of morphology and live bacteria in different media where staining, labelling, or fixing the strain is not necessary [112]. AFM detects forces acting between the surface of the specimen and the sharp tip mounted on a cantilever. The study of nanomechanical properties is of particular use when bacterial morphology changes do not provide enough information or are at a size-scale smaller than the resolution of the microscope. Force spectroscopy, another AFM feature, is used to quantify the forces between the surface of a specimen and the sharp tip. This is done by measuring cantilever deflection as a function of probe-specimen distance when the tip is brought into proximity of the specimen and retracted from it. These measurements yield force-distance curves that provide information on the nanomechanics of cell surface [112]. These curves can be analyzed by applying theoretical indentation models to acquire quantitative information on sample elasticity, i.e., the Young modulus (YM) [113,114]. Applying the theoretical models presumes a well-established geometry of the tip and physical properties of the cantilever. Commonly used Hertzian models describe the indentation of a non-deformable indenter (tip) into an infinitely extending deformable elastic half space (the specimen's surface) [115]. However, the non-elastic response of the specimen and non-perpendicular approach of the tip to the surface may complicate analysis [116].

Topography of the specimen obtained while acquiring force-distance curves is particularly useful, meaning that morphology and nanomechanics measurements are done simultaneously. This can be achieved by utilizing the respective measurement modes [117]. Possible treatment-induced alterations can be detected by measuring the YM of a cell. Despite these described advantages, this powerful non-destructive technique is underused when it comes to studying bacteria exposed to nanomaterials. In particular, reports can be found on the AFM of dried out AgNP-treated bacterial cells. These results include loss of cellular morphology of AgNP-treated *Staphylococcus aureus* [118] and destruction of the *E. coli* cell wall accompanied by a spreading out of peptidoglycan or outer membrane fragments on the surrounding surface indicating

cell lysis [119]. However, bacteria tend to lose their morphological characteristics during the drying process, hence these results might be doubtful. A rare AFM study of hydrated AgNP-treated *E. coli* revealed alteration of ultrastructural and nanomechanical properties of the cell. Also, AgNPs induced extensive damage to the cell membrane, changing its surface roughness, rigidity and adhesion [120].

6.2. ROS detection

A widely accepted fact is that oxidative cell stress is linked to the intracellular ROS level. AgNPs and Ag ions may act as catalysts and increase ROS generation, which in turn leads to oxidative stress [46]. The fluorescence probe 2',7'-dichlorodihydrofluorescein diacetate (DCFH₂-DA), which diffuses through the cell membrane, can be used to measure bacterial ROS generation during AgNP treatment. DCFH₂-DA deacetylates to non-fluorescent, but membrane-impermeable, 2',7'-dichlorodihydrofluorescein (DCFH₂) due to intracellular esterases. Subsequently, DCFH₂ reacts with intracellular ROS to produce fluorescent 2',7'-dichlorofluorescein (DCF) which is trapped inside the cell, making it fluorescent [121]. This probe was proved to be a suitable marker for total ROS production [121] and is the most widely used fluorescent probe for detecting intracellular hydrogen peroxide [122]. The intensity of the obtained DCF signal fluorescence signal is thought to be proportional to the amount of ROS [123].

Research data obtained from previous reports are mostly raw DCF data [94,124] or are normalized the non-dyed control (background fluorescence) [125]. The data may also be given with respect to hydrogen peroxide induced DCF signal [126] or given with respect to the non-treated bacteria [127,128]. The published data suggest that: treatment with AgNPs alone did not induce significant ROS formation [126]; a significant increase in the DCF fluorescence intensity was observed for AgNP-treated bacterial cells [94]; colloidal silver significantly increased the production of ROS when compared with untreated cells [125]; ROS played a very important role in the antibacterial mechanism of AgNPs [128]. Interestingly, ROS detection data in AgNP-treated *E. coli* [127] showed that the fluorescence signal of AgNP-treated cells is lower than for non-treated cells, regarding most treatment concentrations. A ROS increase in bacterial cells, induced by biosynthesized AgNPs, was confirmed by DCFH₂ and antioxidant scavenging [129]. Treatment using the LAL-synthesized AgNPs resulted in particle-size dependent ROS generation, which was highest for particles with an average size of 19 nm [124].

Some nanoparticles reduce the obtained DCF signal. A masking effect for the DCF fluorescence signal has been reported for iron oxide nanoparticles [130] while coated AgNPs were shown to decrease ROS levels due to fluorescence quenching and adsorbing the fluorescent dye [123]. Hence, extraction of the intracellular ROS fluorescence signal from the total signal generated in the sample might not be trivial

given that AgNPs possess characteristic optical properties that must be taken into account when analyzing the DCF signal. This is due to two main reasons. First, cellular ROS must be resolved from the contribution provided by autooxidation signal of the dye. Second, light is attenuated due to absorption and/or scattering on both the nanoparticles and cells, present in the measured sample.

7. Aims and Scopes of the Study

The motive of this paper is to investigate, describe and understand the bactericidal mechanism of laser-synthesized AgNPs. Accordingly, it becomes vital to understand the underlying mechanisms of bacterial growth. This facilitates investigating the influence of AgNPs on bacterial growth, when added to the system under the same controlled conditions. The investigation relies on modelling while ensuring that the model incorporates basic interactions/processes within the system. Due to the variety and complexity of bacterial growth models found in the literature, numerous models are considered to satisfactorily fit the bacterial growth data. Since these models incorporate a large number of parameters, it seemed most convenient to construct a novel model for bacterial growth and inactivation. Furthermore, since bacterial population dynamics is a very multidisciplinary field, consideration should be given to the fact that many researchers do not have a mathematical background. Therefore, a simple method for data analysis and determining growth/death parameters should be provided.

A relatively rarely investigated antibacterial effect for LAL-synthesized silver colloid, considered to be free of chemical byproducts, has the potential to reveal its bactericidal action without irrelevant or uncontrollable parameters. Since the physicochemical properties are important for antibacterial action, the AgNPs should be characterized, and their stability and activity determined when added to the biological system. The designed model for non-treated *E. coli* cells is extended, and the bactericidal mechanism is probed using modelling of the obtained OD growth curves of *E. coli* treated with different concentrations of laser-produced AgNPs. The objective is not just to provide a mathematical description of the curves, but also, based on the modeling approach at the microscopic level, to explain bacterial growing and dying mechanisms.

In general, despite the numerous studies, conflicting reports on the mode of antibacterial action of colloidal silver still exist. This could be partially due to differences in AgNP colloid properties which depend on the synthesis method, and also due to discord in applied experimental methods and data analysis. Moreover, based on the literature, it is important to reveal whether these nanoparticles interact with and/or penetrate the membrane. Based on modeling of the growth of AgNP-treated bacteria, this study determines whether the penetration of the LAL-

synthesized AgNPs into cells is linked to the bactericidal mechanism. Furthermore, the antibacterial mode of action for AgNPs is most likely an interplay of many mechanisms. Besides membrane penetration and damage/alterations, other notable mechanisms include oxidative stress based on ROS generation. Therefore, this study is also designed to experimentally probe these two mechanisms as the mode of action of laser-synthesized AgNPs. Most of the experimental findings are obtained by studying the time development of the DCF fluorescence signal, which is proportional to the ROS level, and time-dependent YM spectroscopy of bacterial cells. Besides the proposed bactericidal mechanism of AgNPs, this study also provides a contribution based on its carefully designed experiments and data analysis approach, especially the DCF signal measurements and cellular ROS extraction.

Overall, this study aims to provide a deeper understanding of the mode of antibacterial action for laser-produced AgNPs against *E. coli* as a model organism and open a discussion on some of the findings given in the literature in relation to our results.

References

- [1] Mijndonckx K, Leys N, Mahillon J, Silver S, Van Houdt R. Antimicrobial silver: Uses, toxicity and potential for resistance. *BioMetals* 2013;26:609–21. <https://doi.org/10.1007/s10534-013-9645-z>.
- [2] Alexander JW. History of the Medical Use of Silver. *Surg Infect (Larchmt)* 2009;10:289–92. <https://doi.org/10.1089/sur.2008.9941>.
- [3] Prabhu S, Poulouse EK. Silver nanoparticles: mechanism of antimicrobial action, synthesis, medical applications, and toxicity effects. *Int Nano Lett* 2012;2:32. <https://doi.org/10.1186/2228-5326-2-32>.
- [4] Ahonen M, Kahru A, Ivask A, Kasemets K, Kõljalg S, Mantecca P, et al. Proactive Approach for Safe Use of Antimicrobial Coatings in Healthcare Settings: Opinion of the COST Action Network AMiCI. *Int J Environ Res Public Health* 2017;14:366. <https://doi.org/10.3390/ijerph14040366>.
- [5] SCCS. Scientific Committee on Consumer Safety SCCS OPINION on Colloidal Silver (nano). 2018.
- [6] Committee ES. Guidance on the risk assessment of the application of nanoscience and nanotechnologies in the food and feed chain. *EFSA J* 2011;9:2140. <https://doi.org/10.2903/j.efsa.2011.2140>.
- [7] Bondarenko O, Juganson K, Ivask A, Kasemets K, Mortimer M, Kahru A. Toxicity of Ag, CuO and ZnO nanoparticles to selected environmentally relevant test organisms and mammalian cells in vitro: A critical review. *Arch Toxicol* 2013;87:1181–200. <https://doi.org/10.1007/s00204-013-1079-4>.
- [8] Bell BG, Schellevis F, Stobberingh E, Goossens H, Pringle M. A systematic review and meta-analysis of the effects of antibiotic consumption on antibiotic resistance. *BMC Infect Dis* 2014;14:13. <https://doi.org/10.1186/1471-2334-14-13>.
- [9] Mobarki N, Almerabi B, Hattan A. Antibiotic Resistance Crisis. *Int J Med Dev Ctries* 2019;40:561–4. <https://doi.org/10.24911/IJMDC.51-1549060699>.
- [10] Davies J, Davies D. Origins and Evolution of Antibiotic Resistance. *Microbiol Mol Biol Rev* 2010;74:417–33. <https://doi.org/10.1128/MMBR.00016-10>.
- [11] Davies J, Davies D. Origins and Evolution of Antibiotic Resistance. *Microbiol Mol Biol Rev* 2010;74:417–33. <https://doi.org/10.1128/MMBR.00016-10>.
- [12] Munita JM, Arias CA. Mechanisms of Antibiotic Resistance. *Microbiol Spectr* 2016;4:464–72. <https://doi.org/10.1128/microbiolspec.VMBF-0016-2015>.
- [13] Blair JMA, Webber MA, Baylay AJ, Ogbolu DO, Piddock LJ V. Molecular mechanisms of antibiotic resistance. *Nat Rev Microbiol* 2015;13:42–51.

- <https://doi.org/10.1038/nrmicro3380>.
- [14] Bush K, Courvalin P, Dantas G, Davies J, Eisenstein B, Huovinen P, et al. Tackling antibiotic resistance. *Nat Rev Microbiol* 2011;9:894–6. <https://doi.org/10.1038/nrmicro2693>.
- [15] Panáček A, Smékalová M, Kilianová M, Pruček R, Bogdanová K, Věčřová R, et al. Strong and nonspecific synergistic antibacterial efficiency of antibiotics combined with silver nanoparticles at very low concentrations showing no cytotoxic effect. *Molecules* 2016;21:1–17. <https://doi.org/10.3390/molecules21010026>.
- [16] Masri A, Anwar A, Ahmed D, Siddiqui RB, Shah MR, Khan NA. Silver nanoparticle conjugation-enhanced antibacterial efficacy of clinically approved drugs cephadrine and vildagliptin. *Antibiotics* 2018;7:1–12. <https://doi.org/10.3390/antibiotics7040100>.
- [17] Levy SB, Marshall B. Antibacterial resistance worldwide: causes, challenges and responses. *Nat Med* 2004;10:S122–9. <https://doi.org/10.1038/nm1145>.
- [18] Rai M, Yadav A, Gade A. Silver nanoparticles as a new generation of antimicrobials. *Biotechnol Adv* 2009;27:76–83. <https://doi.org/10.1016/j.biotechadv.2008.09.002>.
- [19] Morones JR, Elechiguerra JL, Camacho A, Holt K, Kouri JB, Ramírez JT, et al. The bactericidal effect of silver nanoparticles. *Nanotechnology* 2005;16:2346–53. <https://doi.org/10.1088/0957-4484/16/10/059>.
- [20] Kim JS, Kuk E, Yu KN, Kim J-H, Park SJ, Lee HJ, et al. Antimicrobial effects of silver nanoparticles. *Nanomedicine Nanotechnology, Biol Med* 2007;3:95–101. <https://doi.org/10.1016/j.nano.2006.12.001>.
- [21] Schlemmer W, Fischer W, Zankel A, Vukušić T, Filipič G, Jurov A, et al. Green Procedure to Manufacture Nanoparticle-Decorated Paper Substrates. *Materials (Basel)* 2018;11:2412. <https://doi.org/10.3390/ma11122412>.
- [22] Siddiqi KS, Husen A, Rao RAK. A review on biosynthesis of silver nanoparticles and their biocidal properties. *J Nanobiotechnology* 2018;16. <https://doi.org/10.1186/s12951-018-0334-5>.
- [23] Wang L, Hu C, Shao L. The antimicrobial activity of nanoparticles: present situation and prospects for the future. *Int J Nanomedicine* 2017;Volume 12:1227–49. <https://doi.org/10.2147/IJN.S121956>.
- [24] Hajipour MJ, Fromm KM, Akbar Ashkarran A, Jimenez de Aberasturi D, Larramendi IR de, Rojo T, et al. Antibacterial properties of nanoparticles. *Trends Biotechnol* 2012;30:499–511. <https://doi.org/10.1016/j.tibtech.2012.06.004>.
- [25] Slavin YN, Asnis J, Häfeli UO, Bach H. Metal nanoparticles: understanding the

- mechanisms behind antibacterial activity. *J Nanobiotechnology* 2017;15:65. <https://doi.org/10.1186/s12951-017-0308-z>.
- [26] Cui Y, Zhao Y, Tian Y, Zhang W, Lü X, Jiang X. The molecular mechanism of action of bactericidal gold nanoparticles on *Escherichia coli*. *Biomaterials* 2012;33:2327–33. <https://doi.org/10.1016/j.biomaterials.2011.11.057>.
- [27] Zhao Y, Ye C, Liu W, Chen R, Jiang X. Tuning the composition of AuPt bimetallic nanoparticles for antibacterial application. *Angew Chemie - Int Ed* 2014;53:8127–31. <https://doi.org/10.1002/anie.201401035>.
- [28] Li M, Ma Z, Zhu Y, Xia H, Yao M, Chu X, et al. Toward a Molecular Understanding of the Antibacterial Mechanism of Copper-Bearing Titanium Alloys against *Staphylococcus aureus*. *Adv Healthc Mater* 2016;5:557–66. <https://doi.org/10.1002/adhm.201500712>.
- [29] Liu S, Zeng TH, Hofmann M, Burcombe E, Wei J, Jiang R, et al. Antibacterial activity of graphite, graphite oxide, graphene oxide, and reduced graphene oxide: Membrane and oxidative stress. *ACS Nano* 2011;5:6971–80. <https://doi.org/10.1021/nn202451x>.
- [30] Leung YH, Xu X, Ma APY, Liu F, Ng AMC, Shen Z, et al. Toxicity of ZnO and TiO₂ to *Escherichia coli* cells. *Sci Rep* 2016;6:1–13. <https://doi.org/10.1038/srep35243>.
- [31] Dizaj SM, Lotfipour F, Barzegar-Jalali M, Zarrintan MH, Adibkia K. Antimicrobial activity of the metals and metal oxide nanoparticles. *Mater Sci Eng C* 2014;44:278–84. <https://doi.org/10.1016/j.msec.2014.08.031>.
- [32] Sirelkhatim A, Mahmud S, Seeni A, Kaus NHM, Ann LC, Bakhori SKM, et al. Review on Zinc Oxide Nanoparticles: Antibacterial Activity and Toxicity Mechanism. *Nano-Micro Lett* 2015;7:219–42. <https://doi.org/10.1007/s40820-015-0040-x>.
- [33] Sondi I, Salopek-Sondi B. Silver nanoparticles as antimicrobial agent: a case study on *E. coli* as a model for Gram-negative bacteria. *J Colloid Interface Sci* 2004;275:177–82. <https://doi.org/10.1016/j.jcis.2004.02.012>.
- [34] Ruparelia JP, Chatterjee AK, Dutttagupta SP, Mukherji S. Strain specificity in antimicrobial activity of silver and copper nanoparticles. *Acta Biomater* 2008;4:707–16. <https://doi.org/10.1016/j.actbio.2007.11.006>.
- [35] Shrivastava S, Bera T, Roy A, Singh G, Ramachandrarao P, Dash D. Characterization of enhanced antibacterial effects of novel silver nanoparticles. *Nanotechnology* 2007;18:225103. <https://doi.org/10.1088/0957-4484/18/22/225103>.
- [36] Lee S, Jun B-H. Silver Nanoparticles: Synthesis and Application for

- Nanomedicine. *Int J Mol Sci* 2019;20:865. <https://doi.org/10.3390/ijms20040865>.
- [37] Mousavi-Khattat M, Keyhanfar M, Razmjou A. A comparative study of stability, antioxidant, DNA cleavage and antibacterial activities of green and chemically synthesized silver nanoparticles. *Artif Cells, Nanomedicine, Biotechnol* 2018;46:S1022–31. <https://doi.org/10.1080/21691401.2018.1527346>.
- [38] Slepíčka P, Kasálková NS, Siegel J, Kolská Z, Švorčík V. Methods of gold and silver nanoparticles preparation. *Materials (Basel)* 2020;13:1. <https://doi.org/10.3390/ma13010001>.
- [39] Zafar N, Shamaila S, Nazir J, Sharif R, Shahid Rafique M, Ul-Hasan J, et al. Antibacterial Action of Chemically Synthesized and Laser Generated Silver Nanoparticles against Human Pathogenic Bacteria. *J Mater Sci Technol* 2016;32:721–8. <https://doi.org/10.1016/j.jmst.2016.05.009>.
- [40] Korshed P, Li L, Liu Z, Wang T. The Molecular Mechanisms of the Antibacterial Effect of Picosecond Laser Generated Silver Nanoparticles and Their Toxicity to Human Cells. *PLoS One* 2016;11:e0160078. <https://doi.org/10.1371/journal.pone.0160078>.
- [41] Pandey JK, Swarnkar RK, Soumya KK, Dwivedi P, Singh MK, Sundaram S, et al. Silver Nanoparticles Synthesized by Pulsed Laser Ablation: as a Potent Antibacterial Agent for Human Enteropathogenic Gram-Positive and Gram-Negative Bacterial Strains. *Appl Biochem Biotechnol* 2014;174:1021–31. <https://doi.org/10.1007/s12010-014-0934-y>.
- [42] Perito B, Giorgetti E, Marsili P, Muniz-Miranda M. Antibacterial activity of silver nanoparticles obtained by pulsed laser ablation in pure water and in chloride solution. *Beilstein J Nanotechnol* 2016;7:465–73. <https://doi.org/10.3762/bjnano.7.40>.
- [43] Besner S, Kabashin A V., Winnik FM, Meunier M. Ultrafast laser based “green” synthesis of non-toxic nanoparticles in aqueous solutions. *Appl Phys A* 2008;93:955–9. <https://doi.org/10.1007/s00339-008-4773-y>.
- [44] Vamanu E, Ene M, Biță B, Ionescu C, Crăciun L, Sârbu I. In vitro human microbiota response to exposure to silver nanoparticles biosynthesized with mushroom extract. *Nutrients* 2018;10. <https://doi.org/10.3390/nu10050607>.
- [45] Amendola V, Meneghetti M. Laser ablation synthesis in solution and size manipulation of noble metal nanoparticles. *Phys Chem Chem Phys* 2009;11:3805. <https://doi.org/10.1039/b900654k>.
- [46] Lugarà P, Volpe A, Sportelli M, Ancona A, Picca R, Palazzo G, et al. The Pros and Cons of the Use of Laser Ablation Synthesis for the Production of Silver Nano-Antimicrobials. *Antibiotics* 2018;7:67. <https://doi.org/10.3390/antibiotics7030067>.

- [47] Krstulović N, Shannon S, Stefanuik R, Fanara C. Underwater-laser drilling of aluminum. *Int J Adv Manuf Technol* 2013;69:1765–73. <https://doi.org/10.1007/s00170-013-5141-4>.
- [48] Sharma VK, Yngard RA, Lin Y. Silver nanoparticles: Green synthesis and their antimicrobial activities. *Adv Colloid Interface Sci* 2009;145:83–96. <https://doi.org/10.1016/j.cis.2008.09.002>.
- [49] Tilaki RM, Irajizad A, Mahdavi SM. Stability, size and optical properties of silver nanoparticles prepared by laser ablation in different carrier media. *Appl Phys A* 2006;84:215–9. <https://doi.org/10.1007/s00339-006-3604-2>.
- [50] Bhattacharjee S. DLS and zeta potential – What they are and what they are not? *J Control Release* 2016;235:337–51. <https://doi.org/10.1016/j.jconrel.2016.06.017>.
- [51] Doane TL, Chuang C, Hill RJ, Burda C. Nanoparticle ζ -Potentials. *Acc Chem Res* 2012;45:317–26. <https://doi.org/10.1021/ar200113c>.
- [52] Müller R, Jacobs C, Kayser O. Nanosuspensions as particulate drug formulations in therapy. *Adv Drug Deliv Rev* 2001;47:3–19. [https://doi.org/10.1016/s0169-409x\(00\)00118-6](https://doi.org/10.1016/s0169-409x(00)00118-6).
- [53] Carvalho PM, Felício MR, Santos NC, Gonçalves S, Domingues MM. Application of Light Scattering Techniques to Nanoparticle Characterization and Development. *Front Chem* 2018;6:1–17. <https://doi.org/10.3389/fchem.2018.00237>.
- [54] Xia Y, Halas NJ. Shape-Controlled Synthesis and Surface Plasmonic Properties of Metallic Nanostructures. *MRS Bull* 2005;30:338–48. <https://doi.org/10.1557/mrs2005.96>.
- [55] Klein T, Buhr E, Georg Frase C. TSEM. *Adv. Imaging Electron Phys.*, vol. 171, Elsevier Inc.; 2012, p. 297–356. <https://doi.org/10.1016/B978-0-12-394297-5.00006-4>.
- [56] Sawaguchi A. *Advanced Transmission Electron Microscopy*. vol. 65. Cham: Springer International Publishing; 2015. <https://doi.org/10.1007/978-3-319-15177-9>.
- [57] Martínez-Castañón GA, Niño-Martínez N, Martínez-Gutierrez F, Martínez-Mendoza JR, Ruiz F. Synthesis and antibacterial activity of silver nanoparticles with different sizes. *J Nanoparticle Res* 2008;10:1343–8. <https://doi.org/10.1007/s11051-008-9428-6>.
- [58] Agnihotri S, Mukherji S, Mukherji S. Size-controlled silver nanoparticles synthesized over the range 5–100 nm using the same protocol and their antibacterial efficacy. *RSC Adv* 2014;4:3974–83. <https://doi.org/10.1039/C3RA44507K>.

- [59] Mecartney ML, Olson KS, Starostina N, Wong C, West PE. Tip dilation and AFM capabilities in the characterization of nanoparticles. *Jom* 2007;59:12–6. <https://doi.org/10.1007/s11837-007-0003-x>.
- [60] Mousavi SM, Hashemi SA, Ghasemi Y, Atapour A, Amani AM, Savar Dashtaki A, et al. Green synthesis of silver nanoparticles toward bio and medical applications: review study. *Artif Cells, Nanomedicine, Biotechnol* 2018;46:S855–72. <https://doi.org/10.1080/21691401.2018.1517769>.
- [61] Dasgupta N, Ranjan S, Rajendran B, Manickam V, Ramalingam C, Avadhani GS, et al. Thermal co-reduction approach to vary size of silver nanoparticle: its microbial and cellular toxicology. *Environ Sci Pollut Res* 2016;23:4149–63. <https://doi.org/10.1007/s11356-015-4570-z>.
- [62] Rolim WR, Pelegrino MT, de Araújo Lima B, Ferraz LS, Costa FN, Bernardes JS, et al. Green tea extract mediated biogenic synthesis of silver nanoparticles: Characterization, cytotoxicity evaluation and antibacterial activity. *Appl Surf Sci* 2019;463:66–74. <https://doi.org/10.1016/j.apsusc.2018.08.203>.
- [63] Haque MA, Imamura R, Brown GA, Krishnamurthi VR, Niyonshuti II, Marcelle T, et al. An experiment-based model quantifying antimicrobial activity of silver nanoparticles on *Escherichia coli*. *RSC Adv* 2017;7:56173–82. <https://doi.org/10.1039/C7RA10495B>.
- [64] Epp J. X-ray diffraction (XRD) techniques for materials characterization. *Mater. Charact. Using Nondestruct. Eval. Methods*, Elsevier; 2016, p. 81–124. <https://doi.org/10.1016/B978-0-08-100040-3.00004-3>.
- [65] Peleg M, Corradini MG. Microbial Growth Curves: What the Models Tell Us and What They Cannot. *Crit Rev Food Sci Nutr* 2011;51:917–45. <https://doi.org/10.1080/10408398.2011.570463>.
- [66] Peleg M, Corradini MG, Normand MD. The logistic (Verhulst) model for sigmoid microbial growth curves revisited. *Food Res Int* 2007;40:808–18. <https://doi.org/10.1016/j.foodres.2007.01.012>.
- [67] López S, Prieto M, Dijkstra J, Dhanoa MS, France J. Statistical evaluation of mathematical models for microbial growth. *Int J Food Microbiol* 2004;96:289–300. <https://doi.org/10.1016/j.ijfoodmicro.2004.03.026>.
- [68] Taub IA, Feeherry FE, Ross EW, Kustin K, Doona CJ. A Quasi-Chemical Kinetics Model for the Growth and Death of *Staphylococcus aureus* in Intermediate Moisture Bread. *J Food Sci* 2003;68:2530–7. <https://doi.org/10.1111/j.1365-2621.2003.tb07056.x>.
- [69] Gibson AM, Bratchell N, Roberts TA. The effect of sodium chloride and temperature on the rate and extent of growth of *Clostridium botulinum* type A in pasteurized pork slurry. *J Appl Bacteriol* 1987;62:479–90.

- <https://doi.org/10.1111/j.1365-2672.1987.tb02680.x>.
- [70] Zwietering MH, Jongenburger I, Rombouts FM, van 't Riet K. Modeling of the bacterial growth curve. *Appl Environ Microbiol* 1990;56:1875–81.
- [71] Fujikawa H, Kai A, Morozumi S. A new logistic model for *Escherichia coli* growth at constant and dynamic temperatures. *Food Microbiol* 2004;21:501–9. <https://doi.org/10.1016/j.fm.2004.01.007>.
- [72] Gibson AM, Bratchell N, Roberts TA. Predicting microbial growth: growth responses of salmonellae in a laboratory medium as affected by pH, sodium chloride and storage temperature. *Int J Food Microbiol* 1988;6:155–78. [https://doi.org/10.1016/0168-1605\(88\)90051-7](https://doi.org/10.1016/0168-1605(88)90051-7).
- [73] Koutsoumanis K. Predictive modeling of the shelf life of fish under nonisothermal conditions. *Appl Environ Microbiol* 2001;67:1821–9. <https://doi.org/10.1128/AEM.67.4.1821-1829.2001>.
- [74] Buchanan R., Whiting R., Damert W. When is simple good enough: a comparison of the Gompertz, Baranyi, and three-phase linear models for fitting bacterial growth curves. *Food Microbiol* 1997;14:313–26. <https://doi.org/10.1006/fmic.1997.0125>.
- [75] Monod J. The growth of bacterial cultures. *Annu Rev M* 1949;3:371–94.
- [76] Sakanoue S. Extended logistic model for growth of single-species populations. *Ecol Modell* 2007;205:159–68. <https://doi.org/10.1016/j.ecolmodel.2007.02.013>.
- [77] Peleg M, Shetty K. Modeling microbial populations with the original and modified versions of the continuous and discrete logistic equations. *Crit Rev Food Sci Nutr* 1997;37:471–90. <https://doi.org/10.1080/10408399709527785>.
- [78] Jones JE, Walker SJ, Sutherland JP, Peck MW, Little CL. Mathematical modelling of the growth, survival and death of *Yersinia enterocolitica*. *Int J Food Microbiol* 1994;23:433–47. [https://doi.org/10.1016/0168-1605\(94\)90168-6](https://doi.org/10.1016/0168-1605(94)90168-6).
- [79] Xiong R, Xie G, Edmondson AE, Sheard MA. A mathematical model for bacterial inactivation. *Int J Food Microbiol* 1999;46:45–55. [https://doi.org/10.1016/S0168-1605\(98\)00172-X](https://doi.org/10.1016/S0168-1605(98)00172-X).
- [80] Bevilacqua A, Speranza B, Sinigaglia M, Corbo M. A Focus on the Death Kinetics in Predictive Microbiology: Benefits and Limits of the Most Important Models and Some Tools Dealing with Their Application in Foods. *Foods* 2015;4:565–80. <https://doi.org/10.3390/foods4040565>.
- [81] Baty F, Delignette-Muller M-L. Estimating the bacterial lag time: which model, which precision? *Int J Food Microbiol* 2004;91:261–77. <https://doi.org/10.1016/j.ijfoodmicro.2003.07.002>.

- [82] Swinnen IAM, Bernaerts K, Dens EJJ, Geeraerd AH, Impe JF Van. Predictive modelling of the microbial lag phase: a review. *Int J Food Microbiol* 2004;94:137–59. <https://doi.org/10.1016/j.ijfoodmicro.2004.01.006>.
- [83] Baranyi J. Comparison of Stochastic and Deterministic Concepts of Bacterial Lag. *J Theor Biol* 1998;192:403–8. <https://doi.org/10.1006/jtbi.1998.0673>.
- [84] Baranyi J, Roberts TA, McClure P. A non-autonomous differential equation to model bacterial growth. *Food Microbiol* 1993;10:43–59. <https://doi.org/10.1006/fmic.1993.1005>.
- [85] Baranyi J, Roberts TA. A dynamic approach to predicting bacterial growth in food. *Int J Food Microbiol* 1994;23:277–94. [https://doi.org/10.1016/0168-1605\(94\)90157-0](https://doi.org/10.1016/0168-1605(94)90157-0).
- [86] Hills BP, Mackey BM. Multi-compartment kinetic models for injury, resuscitation, induced lag and growth in bacterial cell populations. *Food Microbiol* 1995;12:333–46. [https://doi.org/10.1016/S0740-0020\(95\)80114-6](https://doi.org/10.1016/S0740-0020(95)80114-6).
- [87] Drummond LJ. Effects of sub-MIC concentrations of antibiotics on growth of and toxin production by *Clostridium difficile*. *J Med Microbiol* 2003;52:1033–8. <https://doi.org/10.1099/jmm.0.05387-0>.
- [88] Cummins J, Reen FJ, Baysse C, Mooij MJ, O’Gara F. Subinhibitory concentrations of the cationic antimicrobial peptide colistin induce the pseudomonas quinolone signal in *Pseudomonas aeruginosa*. *Microbiology* 2009;155:2826–37. <https://doi.org/10.1099/mic.0.025643-0>.
- [89] Theophel K, Schacht VJ, Schlatter M, Schnell S, Stingu C-S, Schaumann R, et al. The importance of growth kinetic analysis in determining bacterial susceptibility against antibiotics and silver nanoparticles. *Front Microbiol* 2014;5:1–10. <https://doi.org/10.3389/fmicb.2014.00544>.
- [90] Gomez Escalada M, Russell AD, Maillard JY, Ochs D. Triclosan-bacteria interactions: Single or multiple target sites? *Lett Appl Microbiol* 2005;41:476–81. <https://doi.org/10.1111/j.1472-765X.2005.01790.x>.
- [91] Li W-R, Sun T-L, Zhou S-L, Ma Y-K, Shi Q-S, Xie X-B, et al. A comparative analysis of antibacterial activity, dynamics, and effects of silver ions and silver nanoparticles against four bacterial strains. *Int Biodeterior Biodegradation* 2017;123:304–10. <https://doi.org/10.1016/j.ibiod.2017.07.015>.
- [92] Ahmad T, Wani IA, Manzoor N, Ahmed J, Asiri AM. Biosynthesis, structural characterization and antimicrobial activity of gold and silver nanoparticles. *Colloids Surfaces B Biointerfaces* 2013;107:227–34. <https://doi.org/10.1016/j.colsurfb.2013.02.004>.
- [93] Li W-R, Xie X-B, Shi Q-S, Zeng H-Y, OU-Yang Y-S, Chen Y-B. Antibacterial

- activity and mechanism of silver nanoparticles on *Escherichia coli*. *Appl Microbiol Biotechnol* 2010;85:1115–22. <https://doi.org/10.1007/s00253-009-2159-5>.
- [94] Chatterjee T, Chatterjee BK, Majumdar D, Chakrabarti P. Antibacterial effect of silver nanoparticles and the modeling of bacterial growth kinetics using a modified Gompertz model. *Biochim Biophys Acta - Gen Subj* 2015;1850:299–306. <https://doi.org/10.1016/j.bbagen.2014.10.022>.
- [95] Farrokhi Z, Ayati A, Kanvisi M, Sillanpää M. Recent advance in antibacterial activity of nanoparticles contained polyurethane. *J Appl Polym Sci* 2019;136:1–13. <https://doi.org/10.1002/app.46997>.
- [96] Franci G, Falanga A, Galdiero S, Palomba L, Rai M, Morelli G, et al. Silver Nanoparticles as Potential Antibacterial Agents. *Molecules* 2015;20:8856–74. <https://doi.org/10.3390/molecules20058856>.
- [97] Xiu Z, Zhang Q, Puppala HL, Colvin VL, Alvarez PJJ. Negligible Particle-Specific Antibacterial Activity of Silver Nanoparticles. *Nano Lett* 2012;12:4271–5. <https://doi.org/10.1021/nl301934w>.
- [98] Smetana AB, Klabunde KJ, Marchin GR, Sorensen CM. Biocidal Activity of Nanocrystalline Silver Powders and Particles. *Langmuir* 2008;24:7457–64. <https://doi.org/10.1021/la800091y>.
- [99] Marambio-Jones C, Hoek EM V. A review of the antibacterial effects of silver nanomaterials and potential implications for human health and the environment. *J Nanoparticle Res* 2010;12:1531–51. <https://doi.org/10.1007/s11051-010-9900-y>.
- [100] Lansdown ABG. Silver in Health Care: Antimicrobial Effects and Safety in Use. *Biofunctional Text. Ski.*, vol. 33, Basel: KARGER; 2006, p. 17–34. <https://doi.org/10.1159/000093928>.
- [101] Feng QL, Wu J, Chen GQ, Cui FZ, Kim TN, Kim JO. A mechanistic study of the antibacterial effect of silver ions on *Escherichia coli* and *Staphylococcus aureus*. *J Biomed Mater Res* 2000;52:662–8. [https://doi.org/10.1002/1097-4636\(20001215\)52:4<662::AID-JBM10>3.0.CO;2-3](https://doi.org/10.1002/1097-4636(20001215)52:4<662::AID-JBM10>3.0.CO;2-3).
- [102] RubenMorones-Ramirez J, Winkler JA, Spina CS, Collins JJ. Silver enhances antibiotic activity against gram-negative bacteria. *Sci Transl Med* 2013;5:1–12. <https://doi.org/10.1126/scitranslmed.3006276>.
- [103] Xiu Z, Ma J, Alvarez PJJ. Differential Effect of Common Ligands and Molecular Oxygen on Antimicrobial Activity of Silver Nanoparticles versus Silver Ions. *Environ Sci Technol* 2011;45:9003–8. <https://doi.org/10.1021/es201918f>.
- [104] Bondarenko O, Ivask A, Käkinen A, Kurvet I, Kahru A. Particle-Cell Contact

- Enhances Antibacterial Activity of Silver Nanoparticles. *PLoS One* 2013;8:e64060. <https://doi.org/10.1371/journal.pone.0064060>.
- [105] Hwang ET, Lee JH, Chae YJ, Kim YS, Kim BC, Sang B-I, et al. Analysis of the Toxic Mode of Action of Silver Nanoparticles Using Stress-Specific Bioluminescent Bacteria. *Small* 2008;4:746–50. <https://doi.org/10.1002/sml.200700954>.
- [106] Ivask A, ElBadawy A, Kaweeteerawat C, Boren D, Fischer H, Ji Z, et al. Toxicity Mechanisms in *Escherichia coli* Vary for Silver Nanoparticles and Differ from Ionic Silver. *ACS Nano* 2014;8:374–86. <https://doi.org/10.1021/nn4044047>.
- [107] Durán N, Durán M, de Jesus MB, Seabra AB, Fávaro WJ, Nakazato G. Silver nanoparticles: A new view on mechanistic aspects on antimicrobial activity. *Nanomedicine Nanotechnology, Biol Med* 2016;12:789–99. <https://doi.org/10.1016/j.nano.2015.11.016>.
- [108] Kubo AL, Capjak I, Vrček IV, Bondarenko OM, Kurvet I, Vija H, et al. Antimicrobial potency of differently coated 10 and 50 nm silver nanoparticles against clinically relevant bacteria *Escherichia coli* and *Staphylococcus aureus*. *Colloids Surfaces B Biointerfaces* 2018;170:401–10. <https://doi.org/10.1016/j.colsurfb.2018.06.027>.
- [109] Zorraquín-Peña I, Cueva C, Bartolomé B, Moreno-Arribas MV. Silver Nanoparticles against Foodborne Bacteria. Effects at Intestinal Level and Health Limitations. *Microorganisms* 2020;8:132. <https://doi.org/10.3390/microorganisms8010132>.
- [110] Dakal TC, Kumar A, Majumdar RS, Yadav V. Mechanistic Basis of Antimicrobial Actions of Silver Nanoparticles. *Front Microbiol* 2016;7:1–17. <https://doi.org/10.3389/fmicb.2016.01831>.
- [111] Chwalibog A, Sawosz E, Hotowy A, Szeliga J, Mitura S, Mitura K, et al. Visualization of interaction between inorganic nanoparticles and bacteria or fungi. *Int J Nanomedicine* 2010;5:1085–94. <https://doi.org/10.2147/IJN.S13532>.
- [112] Dufrêne YF. Atomic Force Microscopy in Microbiology: New Structural and Functional Insights into the Microbial Cell Surface. *MBio* 2014;5:1–14. <https://doi.org/10.1128/mBio.01363-14>.
- [113] Radmacher M. Studying the Mechanics of Cellular Processes by Atomic Force Microscopy. *Methods Cell Biol.*, vol. 83, 2007, p. 347–72. [https://doi.org/10.1016/S0091-679X\(07\)83015-9](https://doi.org/10.1016/S0091-679X(07)83015-9).
- [114] J. Roa J, Oncins G, Diaz J, Sanz F, Segarra M. Calculation of Young's Modulus Value by Means of AFM. *Recent Pat Nanotechnol* 2011;5:27–36. <https://doi.org/10.2174/187221011794474985>.

- [115] Touhami A, Nysten B, Dufrêne YF. Nanoscale Mapping of the Elasticity of Microbial Cells by Atomic Force Microscopy. *Langmuir* 2003;19:4539–43. <https://doi.org/10.1021/la034136x>.
- [116] Eaton P, Fernandes J, Pereira E. Atomic Force Microscopy Study of the Antibacterial Effects of Chitosans on *Escherichia coli* and *Staphylococcus aureus*. *Ultramicroscopy* 2008.
- [117] Chopinet L, Formosa C, Rols MP, Duval RE, Dague E. Imaging living cells surface and quantifying its properties at high resolution using AFM in QI™ mode. *Micron* 2013;48:26–33. <https://doi.org/10.1016/j.micron.2013.02.003>.
- [118] Ali S, Perveen S, Ali M, Jiao T, Sharma AS, Hassan H, et al. Bioinspired morphology-controlled silver nanoparticles for antimicrobial application. *Mater Sci Eng C* 2020;108:110421. <https://doi.org/10.1016/j.msec.2019.110421>.
- [119] Składanowski M, Wypij M, Laskowski D, Golińska P, Dahm H, Rai M. Silver and gold nanoparticles synthesized from *Streptomyces* sp. isolated from acid forest soil with special reference to its antibacterial activity against pathogens. *J Clust Sci* 2017;28:59–79. <https://doi.org/10.1007/s10876-016-1043-6>.
- [120] Ramalingam B, Parandhaman T, Das SK. Antibacterial Effects of Biosynthesized Silver Nanoparticles on Surface Ultrastructure and Nanomechanical Properties of Gram-Negative Bacteria viz. *Escherichia coli* and *Pseudomonas aeruginosa*. *ACS Appl Mater Interfaces* 2016;8:4963–76. <https://doi.org/10.1021/acsami.6b00161>.
- [121] Chen X, Zhong Z, Xu Z, Chen L, Wang Y. 2',7'-Dichlorodihydrofluorescein as a fluorescent probe for reactive oxygen species measurement: Forty years of application and controversy. *Free Radic Res* 2010;44:587–604. <https://doi.org/10.3109/10715761003709802>.
- [122] Kalyanaraman B, Darley-USmar V, Davies KJA, Dennery PA, Forman HJ, Grisham MB, et al. Measuring reactive oxygen and nitrogen species with fluorescent probes: challenges and limitations. *Free Radic Biol Med* 2012;52:1–6. <https://doi.org/10.1016/j.freeradbiomed.2011.09.030>.
- [123] Vinković Vrček I, Pavičić I, Crnković T, Jurašin D, Babič M, Horák D, et al. Does surface coating of metallic nanoparticles modulate their interference with in vitro assays? *RSC Adv* 2015;5:70787–807. <https://doi.org/10.1039/c5ra14100a>.
- [124] Korshed P, Li L, Liu Z, Mironov A, Wang T. Size-dependent antibacterial activity for laser-generated silver nanoparticles. *J Interdiscip Nanomedicine* 2019;4:24–33. <https://doi.org/10.1002/jin2.54>.
- [125] Vila Domínguez A, Ayerbe Algaba R, Miró Canturri A, Rodríguez Villodres Á, Smani Y. Antibacterial Activity of Colloidal Silver against Gram-Negative and Gram-Positive Bacteria. *Antibiotics* 2020;9:36.

- <https://doi.org/10.3390/antibiotics9010036>.
- [126] Al-Sharqi A, Apun K, Vincent M, Kanakaraju D, Bilung LM. Enhancement of the Antibacterial Efficiency of Silver Nanoparticles against Gram-Positive and Gram-Negative Bacteria Using Blue Laser Light. *Int J Photoenergy* 2019;2019:1–12. <https://doi.org/10.1155/2019/2528490>.
- [127] Quinteros MA, Cano Aristizábal V, Dalmaso PR, Paraje MG, Páez PL. Oxidative stress generation of silver nanoparticles in three bacterial genera and its relationship with the antimicrobial activity. *Toxicol Vitro* 2016;36:216–23. <https://doi.org/10.1016/j.tiv.2016.08.007>.
- [128] Xu H, Qu F, Xu H, Lai W, Andrew Wang Y, Aguilar ZP, et al. Role of reactive oxygen species in the antibacterial mechanism of silver nanoparticles on *Escherichia coli* O157:H7. *BioMetals* 2012;25:45–53. <https://doi.org/10.1007/s10534-011-9482-x>.
- [129] Ninganagouda S, Rathod V, Singh D, Hiremath J, Singh AK, Mathew J, et al. Growth Kinetics and Mechanistic Action of Reactive Oxygen Species Released by Silver Nanoparticles from *Aspergillus niger* on *Escherichia coli*. *Biomed Res Int* 2014;2014:1–9. <https://doi.org/10.1155/2014/753419>.
- [130] Aranda A, Sequedo L, Tolosa L, Quintas G, Burello E, Castell JV, et al. Dichloro-dihydro-fluorescein diacetate (DCFH-DA) assay: A quantitative method for oxidative stress assessment of nanoparticle-treated cells. *Toxicol Vitro* 2013;27:954–63. <https://doi.org/10.1016/j.tiv.2013.01.016>.

II. A SIMPLE INTERACTION-BASED *E. COLI* GROWTH MODEL

Reproduced from:

Krce L, Šprung M, Maravić A, Aviani I. A simple interaction-based *E. coli* growth model. Phys Biol 2019;16:066005. <https://doi.org/10.1088/1478-3975/ab3d51>.

© IOP Publishing. Reproduced with permission. All rights reserved.



PAPER

A simple interaction-based *E. coli* growth modelRECEIVED
7 June 2019REVISED
19 August 2019ACCEPTED FOR PUBLICATION
21 August 2019PUBLISHED
18 September 2019Lucija Krce^{1,4}, Matilda Šprung², Ana Maravić³ and Ivica Aviani¹¹ Faculty of Science, Department of Physics, University of Split, Split, Croatia² Faculty of Science, Department of Chemistry, University of Split, Split, Croatia³ Faculty of Science, Department of Biology, University of Split, Split, Croatia⁴ Author to whom any correspondence should be addressed.E-mail: lkrc@pmfst.hr**Keywords:** bacterial growth, growth model, *E. coli*, growth rate, logistic modelSupplementary material for this article is available [online](#)**Abstract**

We present a simple growth model which was developed to explain *Escherichia coli* growth in batch culture. Optical density measurements are used to obtain *E. coli* growth curves for different inoculum sizes and nutrients concentrations. The model is described by two nonlinear mutually dependent differential equations that describe time evolution of bacteria and nutrients concentration. Introduction of the negative bacterium–bacterium interaction term is specific for the model and leads to the population decay. The proposed model describes entire experimental growth curves. The growth rate, as a function of initial nutrients concentration, follows the Monod function, whilst during the growth it decreases proportionally with the concentration of nutrients. The parameters in our equations can be related to the parameters of the logistic model. The proposed model can be applied to different *E. coli* strains and, because of the universality of the equations, might be applied to other bacterial strains.

Introduction

It is generally accepted that the bacterial growth consists of four distinct stages or phases: lag phase, exponential growth phase, stationary phase and mortality phase [1]. These stages are clearly distinguished in a growth curve which shows the change of bacterial concentration in time. The shape of a growth curve provides us with information about the state of bacterial metabolism, the phase at which the inoculum was taken, total number of bacteria in the batch, average division time, etc. Depending on the experimental circumstances, all stages of growth may not be obtained in a growth curve [2–4]. However, every growth curve should at least contain the exponential growth phase and the mortality phase if the growth is monitored for a sufficiently long time. To understand the underlying mechanisms of growth, different approaches and modeling strategies have been and are used, especially to explain the data obtained under different growth conditions. In this paper we consider growth that is described by the primary growth models which explain growth curves obtained for constant temperature, pH and water activity.

Most commonly used models include the Gompertz function and its modifications [5, 6] or are based on the rate logistic (Verhulst) model [1] and its modifications [2, 7]. The Gompertz function, being purely empirical, does not provide any mechanistic insight into the growth. On the other hand, the logistic model seems more intuitive with bacterial growth described by the differential equation. However, it can only explain the exponential and the stationary phase [2]. These two models have been used to fit the growth curves of standard bacterial strains grown in batch culture and in food microbiology [7–9].

Some, more comprehensive, proposals of bacterial growth mechanisms have been given in the last few decades. Buchanan *et al* [10] proposed a three-phase linear model consisting of three equations. The model has a physiological approach and takes into account biological variability but describing each of the first three growth phases with a different equation. When it comes to lag phase prediction and interpretation, the Baranyi model [11, 12] describes lag time in terms of cell adjustment to the new post-inoculum environment. Work done by Hills and Mackey [13] relates lag with the delayed biosynthesis of some essential growth factor and cell injury/resuscitation.

The idea of modeling microbial growth kinetics via substrate concentration was first introduced by Monod [14]. He proposed that the number of cell divisions in time depends on the substrate concentration, thus forming a curve that can be described with the equation of the Michaelis–Menten type. The idea to include influence of resources availability, e.g. nutrients, and waste, e.g. metabolites on the growth of a population, was also proposed by Sakanoue [15].

Not many models include cell inactivation. When depicting bacterial growth, the death phase is usually given as a mirror image of the growth [1]. Peleg and Shetty propose that the combination of logistic growth and Fermi decay could model the entire growth curve of some microbes [16]. They also model cell response to stress which might be indicative of the cell reaction to the presence of an antibacterial agent. The bacterial death was also described by introducing a constant rate decay term into the model equations [17]. Overviews of models given in [18, 19] offer a series of mathematical equations that model only the inactivation process. Some of the proposed models include several parameters and are mathematically complex in giving description only for the death phase.

The main motivation for this work was to investigate, describe and understand our bacterial growth system so that we could control the bacterial growth in a reproducible way. This would enable us to study the influence of an antibacterial agent when it is added to the system at the same, controlled, conditions. Having in mind the variety and complexity of the bacterial growth models found in the literature, we considered the models that would fit our data satisfactory, but with the minimum number of parameters. It was also important that the model takes into account the basic interactions/processes within the system. To satisfy these demands we have constructed a novel growth model and applied it to our experimental data. As for many other models, the bacterial growth is related to the change in nutrients (substrate) concentration and described with the two differential equations that give time evolution of the both, bacteria and nutrients concentrations. Also, a negative bacterium–bacterium interaction term is included, which brings a negative contribution to the overall growth rate. This term prevails after the nutrients have been exhausted, resulting in an appearance of the bacteria death phase. If this term is put to zero, the model is reduced to the logistic growth. To our knowledge, this approach to the description of bacterial inactivation phase has not been described in the literature so far. Furthermore, we offer a simple method for data analysis and determination of growth/death parameters that can be used by researchers without a deep mathematical background. The analysis of *Escherichia coli* DH5alpha strain growth data, obtained for Luria–Bertani growth medium, is discussed in detail. To demonstrate the applicability of the model for different strains and growth mediums, we performed the optical density (OD) measurements

for bacterial growth in Mueller Hinton broth and for *E. coli* ATCC 29213. We found that the proposed model successfully explains the obtained data as well, as presented in supporting information files (stacks.iop.org/PhysBio/16/066005/mmedia) of the paper.

Methods

In this work we have used *E. coli* DH5 α strain to study bacterial growth under the different but controlled growth conditions. Firstly, we have performed growth measurements for batches containing different dilutions of the growth medium inoculated with the same bacterial concentration. By diluting the growth medium, we have proportionally reduced the concentration of the initial nutrients. Secondly, we have performed growth measurements for different inoculum sizes whilst keeping the nutrients at the same level for all batches. Material and methods for additional measurement, made in order to further validate the model, as well as the code for solving differential equations, can be found in the supplementary information.

Optical density (OD) measurements

Different initial nutrients concentration

E. coli DH5 α strain was grown overnight at 37 °C with shaking in 50% Luria–Bertani (LB) (5.0 g l⁻¹ of tryptone, 2.5 g l⁻¹ of yeast extract and 5.0 g l⁻¹ of NaCl per 1 liter of deionized sterile water).

This growth medium will be referred as the master medium. The following day, five dilutions of the fresh master medium were made with sterile deionized water giving the master medium volume shares of 100%, 75%, 50%, 25% and 12.5%. Each dilution was inoculated with 5 · 10⁵ CFU (colony forming units) per milliliter taken from the overnight culture, and incubated for 24 h at 37 °C with shaking. Bacterial growth was monitored through OD measurements of the bacterial batch culture. The OD data at 600 nm wavelength (OD600) were monitored on a microtiter plate reader (BioTek ELx808, USA). To keep the OD signal in the microtiter plate reader linear range, 50% LB broth was used as the master medium. The experiment was performed in triplicate.

Different inoculum sizes

We have performed growth measurements for different inoculum sizes whilst keeping the nutrients at the same level for all batches. We have used the same strain, master medium, growing conditions and microtiter plate reader as described in the section above. An overnight culture was, again, diluted in fresh master broth, grown and adjusted spectrophotometrically to a density of 5 · 10⁸ CFU ml⁻¹. A 10-fold serial dilutions in fresh master medium were then prepared to a final load of 5 · 10² CFU ml⁻¹, and incubated for 24 h at 37 °C with shaking. Bacterial growth was, again, monitored through OD measurements. The experiment was performed in triplicate.

Viable cell counting

The overnight *E. coli* DH5 α culture and the next-day dilution in the master medium was prepared as for OD measurements and was left to grow in the same conditions. At different time points, serial 10-fold dilutions of the batch culture were made and aliquots of 50 μ l were plated on sterile trypticase soy agar (Biolife, Italy) plates. The plates were incubated for 24 h. By counting each colony, the total number of CFU/ml was calculated according to the formula: CFU/ml = (number of colonies \times dilution factor)/volume of the plated culture. We found that 1 absorbance unit (a.u.) corresponds to $3.64 \cdot 10^9$ CFU ml $^{-1}$. The calibration of the spectrophotometer was performed for the cells in the mid-exponential phase. The experiment was performed in triplicate.

Experimental results

Figure 1 shows growth curves of *E. coli* DH5 α obtained for different initial concentrations of nutrients N_0 and the same inoculum size $B_0 = 5 \cdot 10^5$ CFU ml $^{-1}$. Master growth medium nutrients concentration was determined to be $N_M = 2.1 \cdot 10^9$ CFU ml $^{-1}$, where equivalent CFU units are used as it will be explained later. Different initial concentrations of nutrients were produced by dilution of the master medium with sterile deionized water. The ratio $x = N_0/N_M$ which denotes the volume share of the master medium in the batch will be referred as the initial nutrients dilution factor.

The presented curves are the average of OD data obtained from three separate experiments, conducted under the same conditions. The baseline, i.e. OD of the vial and the corresponding sterile growth medium, is subtracted from the raw data so that the OD data reflect only the change in the bacteria concentration. Bacterial concentration in CFU/ml is given on the right axes. It can be noted that the maximum of bacterial OD and the exponential growth rate decreases with the reduction of the nutrients concentration. For all curves, the bacterial OD initially increases exponentially (as will be shown in the following section), exhibits the maximum for time $t \approx 500$ min and gradually decreases for larger t . It can also be seen that the maximum OD decreases with the growth medium dilution. The viable cell counting data (the large squares) show decrease of the bacterial population as well.

Figure 2 shows bacterial growth curves obtained for samples with different inoculum sizes whilst the initial nutrients concentration was kept constant at $N_0 = N_M$. The presented curves are the average of OD data obtained from three separate experiments conducted under the same conditions. Absorbance of the sterile growth medium and the vial was subtracted from the data so that OD reflects only the change in bacterial concentration. Inoculum size B_0 was changed for six orders of magnitude, from $5 \cdot 10^2$ to $5 \cdot 10^8$ CFU

ml $^{-1}$, so that the two successive concentrations differ by an order of magnitude, while all other experimental parameters were kept constant. It can be noted that the inoculum change does seem not affect the overall shape of the curve and the main effect of inoculum change is the shift of the curve along the time axis.

Introducing the model

In order to explain the experimental data, a simple theoretical model of bacterial growth was developed. The basic assumptions of the model are the following: a bacterium collects nutrients and divide, which gives a rise to the bacterial concentration $B(t)$, a number of bacteria per milliliter of the sample. At the same time, it interferes with other bacteria in a complex way. This interference could be seen through the production of metabolic waste, bacterial competition for nutrients, lack of the space etc. Such mechanisms lead to the reduction of bacterial concentration. So, the time change in the bacteria concentration is described with two terms

$$\frac{d}{dt}B(t) = \alpha \cdot N(t) \cdot B(t) - \beta \cdot B(t)^2, \quad (1)$$

where $N(t)$ is concentration of nutrients, a number of nutrient units per milliliter of the sample, and α and β are the interaction strength parameters. First term describes the increase in the bacterial concentration where we presume that bacteria collect nutrients randomly, with the probability that is proportional to the product of the bacterial $B(t)$ and nutrients $N(t)$ concentrations. This term describes the interaction between bacterial cells and nutrients. Consequently, the growth rate is proportional to the quantity of the nutrients. The second term is negative and describes mutual interaction between bacterial cells that reduces bacterial concentration. As this interaction always appears between two bacterial cells, the probability for the interaction to appear is proportional to the square of the bacterial concentration $B(t)$, regardless of the mechanism the interaction is driven by.

We also presume that the concentration of nutrients is changed only because of the bacterial consumption, so that the rate of change of the nutrients concentration is equal to the negative value of bacterial nutrients uptake:

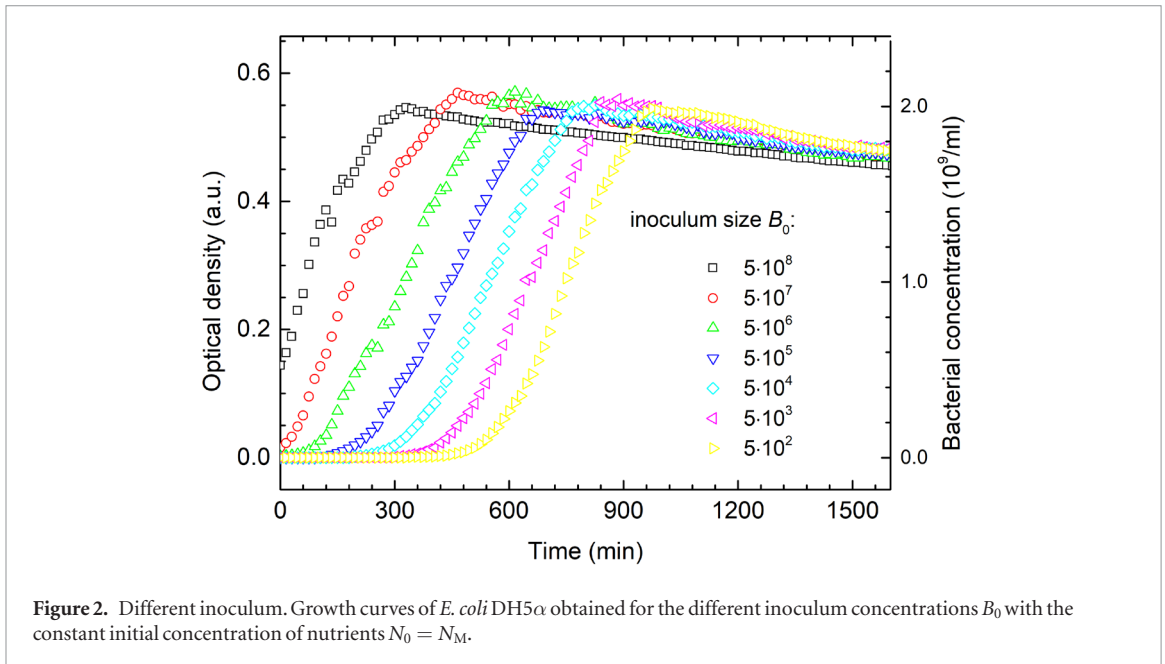
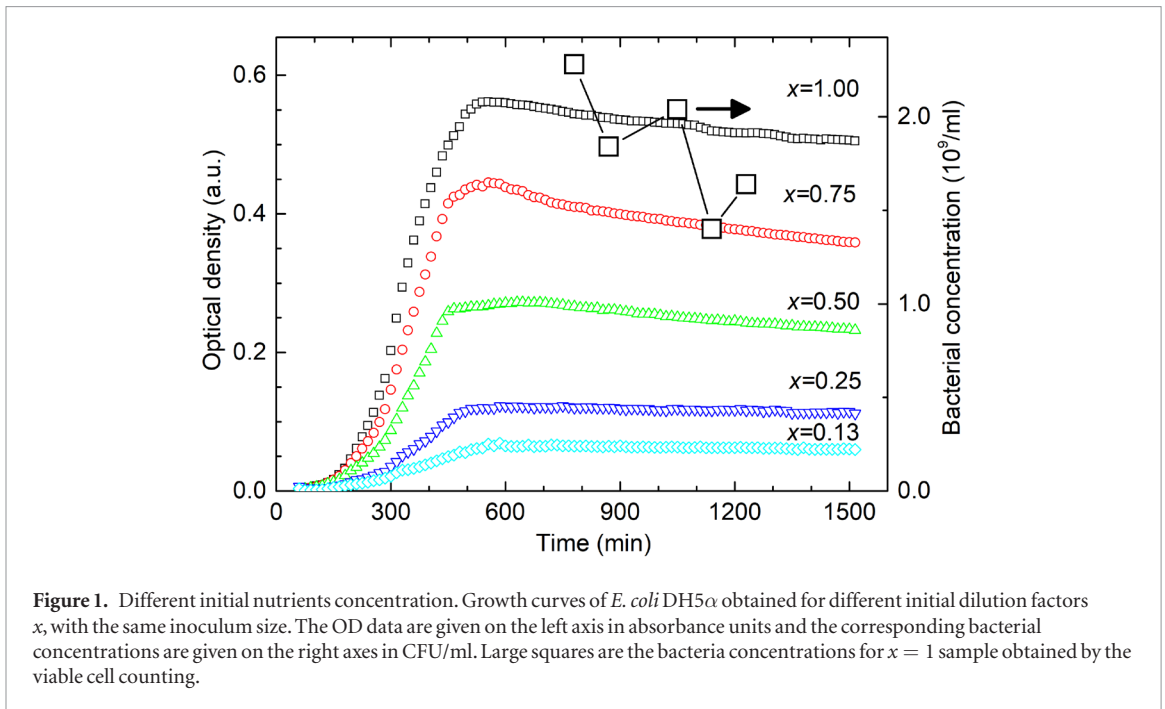
$$\frac{d}{dt}N(t) = -\alpha \cdot B(t) \cdot N(t). \quad (2)$$

Equations (1) and (2) form the system of two mutually dependent non-linear differential equations. Solution of these equations gives the time dependence of the bacterial and nutrients concentrations.

Equation (1) can be written in the form

$$\frac{d}{dt}B(t) = [\alpha \cdot N(t) - \beta \cdot B(t)] \cdot B(t), \quad (3)$$

and can be considered as the exponential growth with the decreasing growth rate, given in the brackets. The



growth rate $\alpha \cdot N(t)$ is the rate at which the bacterial concentration increases due to the uptake of the nutrients by the bacteria. The death rate $\beta \cdot B(t)$ is the rate at which the bacterial concentration decreases due to the bacterial interaction with other bacteria. It is proportional to the bacterial concentration since more bacteria produce more negative influence. If the growth conditions are met, the death rate increases due to the increase of $B(t)$. This means that the fraction of the bacteria which are not able to produce a clone increases with bacterial concentration.

We find convenient to express the concentration of nutrients $N(t)$ in bacteria—equivalent units. If m_N/V is the mass concentration of nutrients, where m_N is the mass of nutrients and V the volume of the sample, and m_{N1} is the quantity of nutrients needed for single bac-

terium growth, then $N(t) = (m_N/m_{N1})/V$ is the concentration of bacteria that could be produced with a given nutrient concentration. In this way we define a constant ‘package’ of nutrients as the quantity needed for the creation of a single bacterium and we can express the $N(t)$ in equivalent CFU/ml units.

Solutions of the system of differential equations (1) and (2), for initial concentration of bacteria $B_0 = 0.001$ a.u., $\alpha = 0.02 \text{ min}^{-1} \text{ a.u.}^{-1}$ and for different values of β are given in figure 3. The nutrients data are given in terms of equivalent concentration of bacteria.

During the process of growth, the nutrients concentration is being reduced due to bacterial consumption. Since nutrients concentration is measured in packages, needed to produce a single bacterium, it

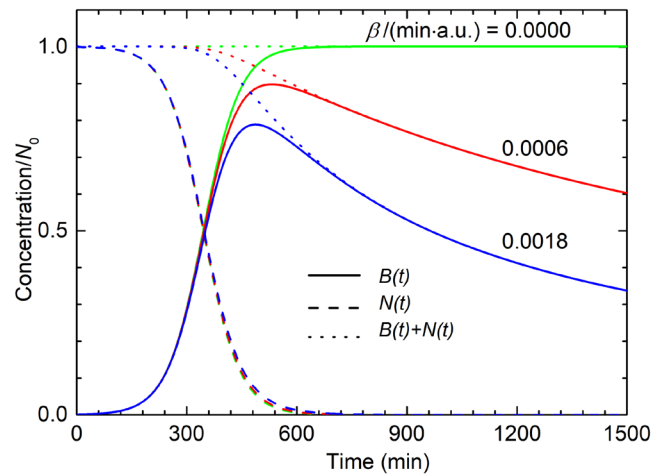


Figure 3. Solutions for different β . Solutions of the system of differential equations (1) and (2) for different values of β reveal time evolution of concentrations of bacteria $B(t)$ and nutrients $N(t)$. Each concentration is divided by the initial nutrient concentration N_0 giving the relative concentration. The data are plotted for $B_0 = 0.001$ a.u. and $\alpha = 0.02 \text{ min}^{-1}$ a.u. $^{-1}$. For $\beta = 0$ a logistic-like curve is obtained with $B(t) + N(t) = N_0 + B_0 = \text{const.}$ (dotted line) does not hold because of the bacterial inactivation.

represents the maximum possible bacterial concentration. The growth is mathematically described as a transformation of nutrients packages to bacteria so that, for $\beta = 0$, the growth capacity is conserved, $B(t) + N(t) = \text{const.}$, as shown by the dotted green line in Fig 3. We also see that for $\beta > 0$ the growth capacity $B(t) + N(t)$ is not conserved and it decreases in time due to the bacterial disintegration. For $0 < t < 240$ min the bacterial growth with the same growth rate is obtained for all cases. For $t > 500$ min the nutrient concentration decreases to zero so that for $\beta = 0$ the bacterial concentration saturates to the maximum value $N_0 + B_0$, while for $\beta > 0$ it exhibits a maximum after which it gradually decreases, similarly to the experimental results of figure 1.

Data analysis

The fitting procedure is simplified by comparing the model and the experimental data for the two limiting growth phases (the exponential and the death phase) in which certain parameters are easily obtained. This procedure also enables a better insight into the physical meaning of the obtained parameters.

Different initial nutrients concentration

At the beginning of the growth, bacterial concentration is much lower than the concentration of nutrients $B(t) \ll N(t)$ and the second term in the brackets of the equation (3) can be neglected. The concentration of nutrients does not change much with respect to the initial concentration, $N(t) \approx N_0$, so that altogether the expression in the brackets is approximately equal to αN_0 . For this case, bacterial growth is exponential with the growth rate $k = \alpha N_0$ and from equation (3) we obtain

$$\frac{d}{dt}B(t) = k \cdot B(t). \quad (4)$$

Solution of this equation

$$B(t) = B_0 \cdot e^{k \cdot t}, \quad (5)$$

depends only on two parameters: inoculum size B_0 and the growth rate k . The logarithm of bacterial concentration, as a function of time, is a straight line with the slope equal to the growth rate k and the intercept equal to the logarithm of the inoculum size B_0 :

$$\ln B(t) = k \cdot t + \ln B_0. \quad (6)$$

In this way we can obtain parameters B_0 and k from the experimental data. Figure 4 shows logarithmic values of the OD data from figure 1 at the beginning of the growth. The symbols are the experimental data for different initial concentrations of nutrients and the solid lines are the theoretical fits, which will be discussed later. We see that at the beginning of the growth the logarithm of bacterial population exhibits a linear time dependence, characteristic for the exponential phase, showing the absence of the lag phase. A change in the growth rate for the curves with the different initial nutrients concentration is clearly seen. To analyze the exponential phase data, we first made the two-parameter linear fits for $t < 240$ min data, in accordance with equation (6), and obtained parameters B_0 and k for each sample. For $x = 0.13$ sample, the deviated points at the beginning of the growth were not included in the fitting procedure because, they significantly differ from the overall trend. We presume that this is probably due to the experimental error. As all the samples have the same inoculum size, we find reasonable to repeat the same fitting procedure, with parameter B_0 fixed. The dotted lines are the one-parameter linear fits of the exponential phase data with fixed $B_0 = 10^{-3}$ a.u. which is the average value obtained from the data of two-parameter fits. The adjusted R^2 values of all linear fits obtained in this manner was above 0.99. The

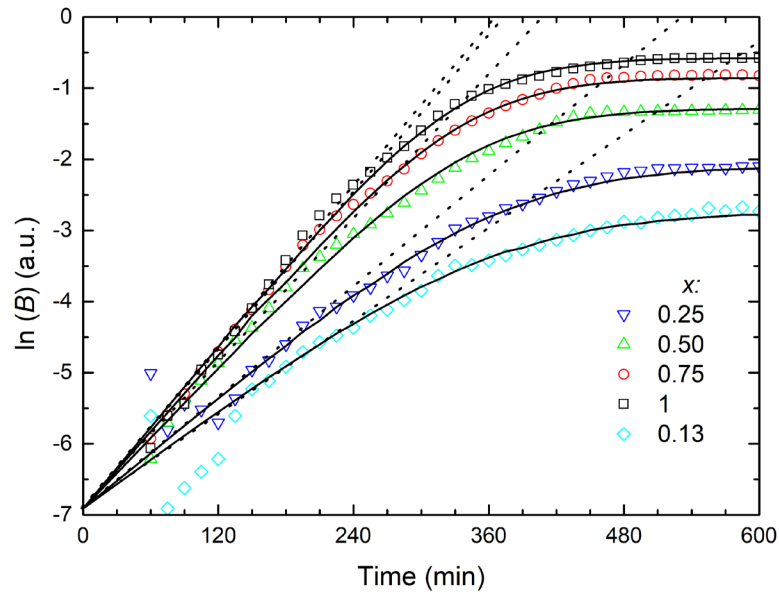


Figure 4. Different initial nutrients concentration: initial exponential growth. Plot of logarithmic values of *E. coli* growth curves from figure 1 for different initial concentration of nutrients where the symbols are experimental data and solid lines the theoretical fits. The dots are the linear fits of the exponential phase data, for $t < 240$ min.

described procedure gave values for k that deviated not more than 10%, with respect to the values obtained if both k and B_0 are varied.

After the growth curve reaches its maximum, which occurs after bacteria have consumed almost all nutrients, $N(t) \approx 0$, the death phase appears in which a gradual decrease of bacterial concentration is observed. It can be seen in Fig 3 that for $t > 600$ min nutrients concentration falls to zero. We can neglect the first term in the brackets of the equation (3), so that the equation reduces to

$$\frac{d}{dt}B(t) = -\beta \cdot B(t)^2. \quad (7)$$

Solution of this equation is

$$B(t) = \frac{1}{\beta \cdot t + C} \quad (8)$$

where C is the integration constant. Reciprocal value of the bacterial concentration

$$\frac{1}{B(t)} = \beta \cdot t + C. \quad (9)$$

is linear in time with the slope that is equal to the parameter β and intercept C . To compare the value of the intercept C with the theory we assume that the position t_M of the maximum of the growth curve corresponds to the maximum of bacterial concentration $B(t_M)$. The maximum value is approximately equal to N_0 , because at the maximum all nutrient packages should be ‘transformed’ to bacteria. Strictly speaking, it is a little bit less than N_0 due to a small population decay before t_M caused by bacterium–bacterium interaction. Time t_M was determined from the data sheet, simply by reading the time for which OD assumes maximum value, with the

error of about 15 min, which is the sampling rate of the instrument. By introducing $B(t_M) = N_0$ in (9) we find that $C = 1/N_0 - \beta \cdot t_M$, and equation (9) becomes

$$\frac{1}{B(t)} = \beta \cdot (t - t_M) + \frac{1}{N_0}. \quad (10)$$

Comparing equations (9) and (10) we conclude that, from the intercept and the slope of the $1/B(t)$ plot, the initial concentration of nutrients can be obtained as

$$N_0 = (C + \beta \cdot t_M)^{-1}. \quad (11)$$

Figure 5 shows the reciprocal growth curves for different initial nutrients dilution factors x and the corresponding linear fits obtained in the death phase, for $t > 600$ min. From the slopes and intercepts of the obtained lines, β and N_0 are determined for each initial nutrients dilution factor x . From equation (11) we find initial nutrients concentrations N_0 to be: N_M , $0.78N_M$, $0.50N_M$, $0.22N_M$ and $0.12N_M$, where $N_M = 2.1 \cdot 10^9$ CFU ml⁻¹ is the nutrients concentration of the master growth medium. This is in excellent accordance with the nominal values given in the Experimental results section: N_M , $0.75N_M$, $0.50N_M$, $0.25N_M$ and $0.13N_M$, respectively. By obtaining the experimental initial nutrients concentration, one obtains the experimental initial dilution factor x . The described procedure can be used for accurate determination of the initial nutrients concentration in the diluted samples. For further discussion and calculations, we use the initial dilution factors obtained from the fits in figure 5, not the nominal ones.

Interaction strength parameters α and β for different initial nutrients dilution factor x are plotted in figure 6. Parameter $\alpha(x) = k(x)/N_0 = k(x)/(N_M \cdot x)$ ($N_M = 0.58$ a.u.) is calculated from the coefficients of growth $k(x)$ obtained from the slopes of linear

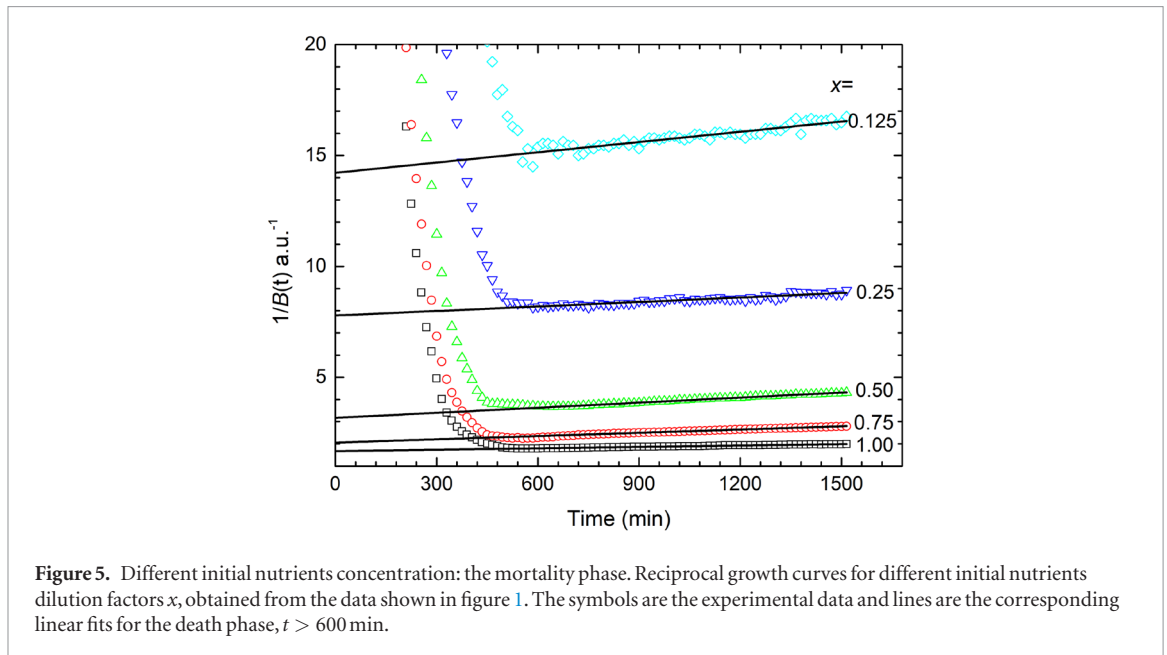


Figure 5. Different initial nutrients concentration: the mortality phase. Reciprocal growth curves for different initial nutrients dilution factors x , obtained from the data shown in figure 1. The symbols are the experimental data and lines are the corresponding linear fits for the death phase, $t > 600$ min.

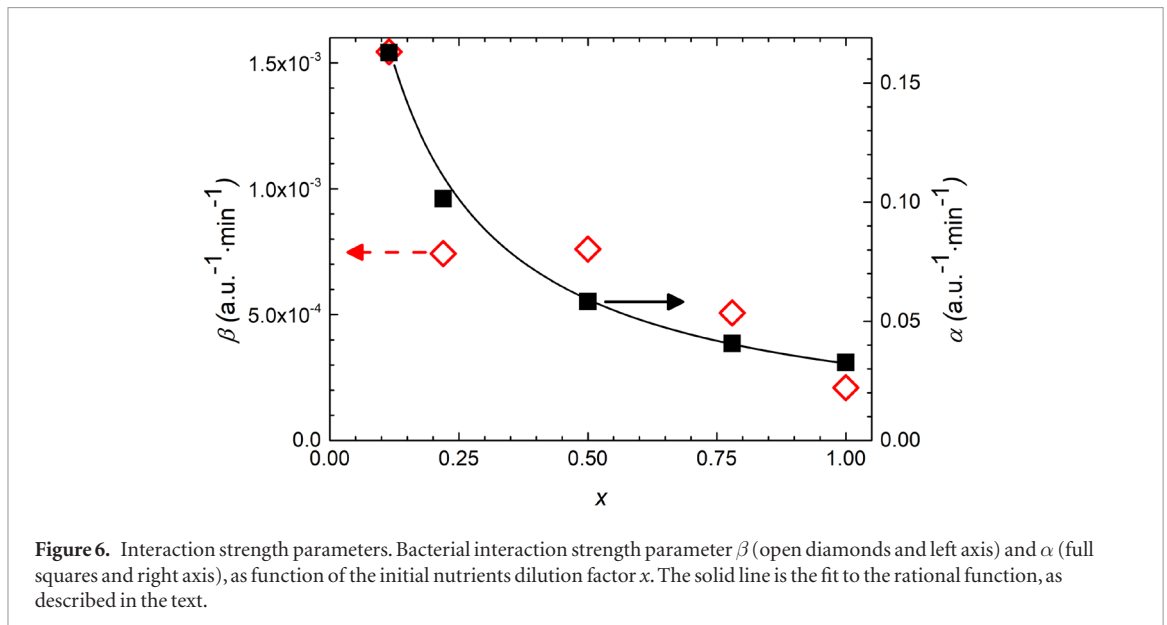


Figure 6. Interaction strength parameters. Bacterial interaction strength parameter β (open diamonds and left axis) and α (full squares and right axis), as function of the initial nutrients dilution factor x . The solid line is the fit to the rational function, as described in the text.

fits in figure 4. The $\beta(x)$ data are obtained from the slopes of the linear fits in figure 5 in accordance with the equation (9). Interaction strength $\beta(x)$ strongly decreases with x , with the dependence very similar to the concentration dependence of parameter $\alpha(x)$ as shown in figure 6 in the appropriate scale. Therefore, we presume that both parameters are described with the function $f(x) = a/(x_{1/2} + x)$ which differs only in parameter a . The solid line in figure 6 is the least-square fit of parameter $\alpha(x)$ (with $R^2 = 0.99$) to the function $f(x)$, with $a = 3.34 \cdot 10^{-2} \text{ min}^{-1} \text{ a.u.}^{-1}$ and $x_{1/2} = 0.093$. The same line is the fit to the same function for parameter $\beta(x)$ (with $R^2 = 0.89$). For parameter $x_{1/2}$ fixed to the value 0.093, this fit gives $a' = 3.37 \cdot 10^{-4} \text{ min}^{-1} \text{ a.u.}^{-1}$.

The same functional dependence of α and β is also found for *E. coli* ATCC 29213, but with different parameters $a = 5.51 \cdot 10^{-2} \text{ min}^{-1} \text{ a.u.}^{-1}$, $a' = 7.45 \cdot$

$10^{-4} \text{ min}^{-1} \text{ a.u.}^{-1}$ and $x_{1/2} = 0.163$, as described in detail in the supplementary file and shown in figure S3.

Comparison between the experimental and the model data for the growth curves in the whole range are given in figure 7. The lines are the best fits obtained from the solutions of model equations (1) and (2).

To resume, note that the fitting procedure requires variation of the four parameters: B_0 , N_0 , α and β , but parameters space is limited since the initial and the final part of the growth curve are well defined with only two of the parameters. To obtain the best fits, we first fitted the data of the exponential phase, from $t = 0$ to 240 min, in accordance to the equation (6). From the least square linear fit for the logarithm of bacterial concentration as a function of time parameters B_0 and $\alpha = k/N_0$ are obtained. We found parameter B_0 to be approximately constant for all the samples with the average value $B_0 = 1.0 \cdot 10^{-3} \text{ a.u.}$. Least square

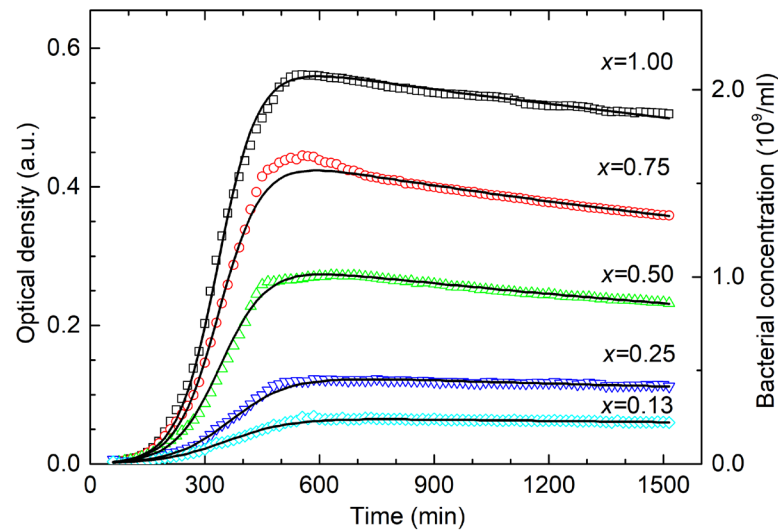


Figure 7. Model application: different initial nutrients concentration. Growth curves given in figure 1 with the corresponding theoretical curves. Symbols are the experimental data and solid lines are the theoretical fits. The OD in absorbance units is given on the left axis and the corresponding bacterial concentrations in CFU/ml are given on the right axes.

linear fits were also performed for the reciprocal bacterial concentration as a function of time according to equation (9) to obtain the slope β and the intercept C . The values for the initial nutrients concentration N_0 were obtained from equation (11). The nutrients concentration of the master growth medium N_M is found from the growth curve fit of the $x = 1$ sample and with the assumption that in the process of growth all the nutrients were consumed, i.e. all the nutrients were converted to bacteria. For the sample with maximal OD, we obtain $N_0 = N_M = 0.58$ a.u., or $N_M = 2.1 \cdot 10^9$ CFU ml $^{-1}$. After inserting the obtained four parameters in the system of differential equations (1) and (2) the solution is found numerically. The solution gives a good description of the entire growth curve for all initial nutrients concentrations, as can be seen in figure 7.

Different inoculum sizes

The model is also used to explain the growth curves obtained for different inoculum sizes whilst the initial nutrients concentration is kept constant. Figure 2 shows that there is an approximately constant time shift between two adjacent concentrations, which means that the reduction of inoculum results in a delay of bacterial growth. The question is: Does the exponential growth starts from the beginning or there is a lag phase? To answer the question, we plotted the first 800 min of the experimental data from figure 2 in 8 in logarithmic OD scale. Note that for samples with $B_0 \leq 5 \cdot 10^5$ CFU ml $^{-1}$ the data at the beginning of the growth are not presented. Those data are below the resolution limit of the instrument, which is about 10^6 CFU ml $^{-1}$ and cannot be resolved from the noise. For all the samples a linear increase at the beginning of the growth is found, in accordance with equation (6). To obtain the intercepts, the missing data are extrapolated by solid lines. According to equation (6) the interceptions of these lines with the

ordinate are the inoculum sizes, and the slopes are the growth rates. From figure 8, we see that for all the samples the intercepts follow the nominal inoculum sizes B_0 and that the growth rate is approximately the same. This brings us to the conclusion that the cells grow exponentially from the very beginning.

To explain the shift along the time axis from figure 2, we consider the exponential bacterial growth (equation (5)) for two samples that differ only in the inoculum sizes which we denote by B_0 and B'_0 . It is easily seen that the growth of the second sample $B'(t)$ can be expressed by the same exponential function $B(t)$ as for the first sample, but with the time shift t' :

$$B'(t) = B_0 \cdot e^{k \cdot (t-t')} = B(t-t'), \quad (12)$$

where

$$t' = \frac{1}{k} \cdot \ln \frac{B_0}{B'_0}. \quad (13)$$

To obtain the shifts along the time axes a linear regression for $B(t)$ is made between 0.1 and 0.4 a.u., for each curve in figure 2. Time shifts are determined from the intercepts of the obtained lines with the time axis.

The inset of figure 9. shows the time shifts t' , measured with respect to the $B_0 = 5 \cdot 10^5$ CFU ml $^{-1}$ growth curve, plotted against the logarithm of the inoculum sizes ratio B_0/B'_0 . The solid line is the linear fit to the data. As can be seen from figure, the time shift is proportional to the logarithm of inoculum size as predicted by equation (13).

According to equation (12), all the curves obtained for different inoculum sizes, when properly shifted, must fall on the same curve. To check this hypothesis, the data from Fig 2, obtained for the different inoculum sizes, were shifted on the time axes for 0, ± 110 , ± 220 and ± 330 min in order to match the curve with $B_0 = 5 \cdot 10^5$ and plotted in figure 9. We see that all data collapsed to a single curve. We conclude that,

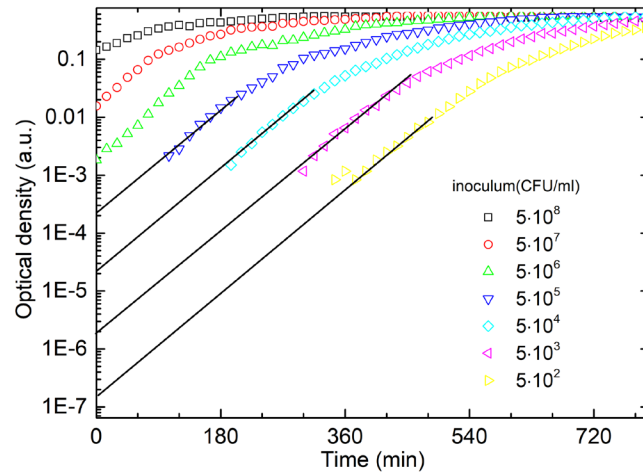


Figure 8. Different inoculum: initial exponential growth. The bacterial growth data from figure 2, obtained for the different inoculum sizes, presented in logarithmic OD plot, exhibit an exponential growth from $t = 0$, with no observable lag. The missing data are extrapolated by the solid lines of equal slope.

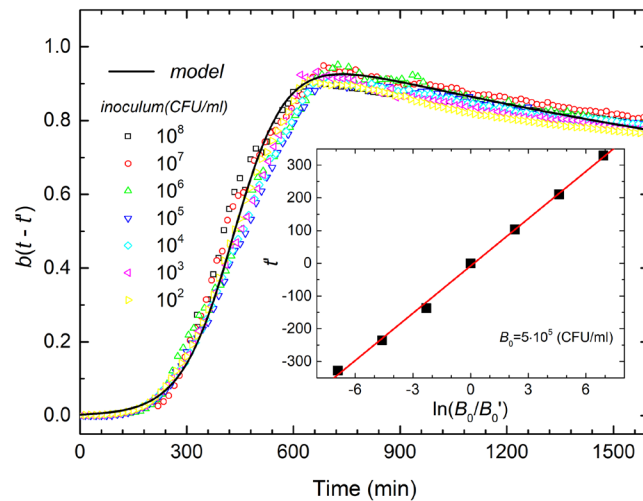


Figure 9. Different inoculum: time shift. Reduced (divided by N_0) growth curves from figure 2 for different inoculum sizes shifted on the time axes to match the $B_0 = 5 \cdot 10^5$ curve. We see that all the data collapse to the single curve. The solid line is the theoretical model curve. The inset shows the time shifts t' plotted against the logarithm of the inoculum sizes B_0^* . The solid line is a linear fit to that data.

in accordance with the model, the change in the inoculum size provides only a shift of the whole curve at the time scale, but keeps the overall shape of the curve unchanged. In the exponential phase, bacterial growth obtained for the initial bacterial concentration B_0 , is equivalent to bacterial growth with ten times lower initial concentration $B_0/10$, obtained with the 110 minutes delay.

From the slope of the linear fit and equation (13), we obtain the growth rate $k(x=1) = k_m \cdot q(x=1) = 0.0208 \pm 0.004 \text{ min}^{-1}$, with the error of only 2%, which is much more accurate than k obtained from the exponential fit of the single curve. These considerations show that exponential bacterial growth phase is present in all samples from the very beginning of the experiment, i.e. from $t=0$. Smaller inoculum size results in larger time shift, because bacteria take longer period of time to reach the maximum population. We

can conclude that the lag phase is not present in our measurements at all. Since all curves are explained with the same growth rate $k(x)$ we also find that the change in inoculum size does not induce the change of the growth rate.

Model formulation and comparison with other models

From the data analysis we obtained the functional dependence of strength parameters $\alpha(x)$ and $\beta(x)$ on nutrient dilution factor x , which enables us to discuss the bacterial growth more comprehensively. If we introduce the reduced bacterial concentration $b(t) = B(t)/N_0$ and reduced nutrients concentration $n(t) = N(t)/N_0$, and take into account functional dependences of $\alpha(x)$ and $\beta(x)$, equations (1) and (2) take on a more general form

Table 1. List of the model variables and parameters.

Symbol	Physical quantity
$B(t)$	Bacterial concentration
B_0	Inoculum size
$N(t)$	Nutrients concentration
N_0	Initial nutrients concentration
N_M	Master growth medium nutrients concentration
x	Initial nutrients dilution factor
$\alpha(x)$	Bacteria–nutrients interaction strength parameter
$\beta(x)$	Bacteria–bacteria interaction strength parameter
k	Exponential growth rate
t_M	Maximum OD time
$b(t)$	Reduced bacterial concentration (per N_0)
$n(t)$	Reduced nutrients concentration (per N_0)
k_m	Bacteria–nutrients interaction strength constant
k_{bb}	Bacteria–bacteria interaction strength constant
$q(x)$	Initial nutrients response function

$$\frac{d}{dt}b(t) = q(x) [k_m b(t) \cdot n(t) - k_{bb} b(t)^2] \quad (14)$$

$$\frac{d}{dt}n(t) = -q(x)k_m b(t) \cdot n(t) \quad (15)$$

$$q(x) = \frac{x}{(x_{1/2} + x)}, \quad (16)$$

with the all the relevant physical quantities of the model given in table 1. In this notation the concentrations $n(t)$ and $b(t)$ are dimensionless quantities that are measured relative to the initial nutrients concentration N_0 and can assume values from 0 to 1, as shown in figure 3. The constants $k_m = a \cdot N_M = 1.94 \cdot 10^{-2} \text{ min}^{-1}$ and $k_{bb} = a' \cdot N_M = 1.96 \cdot 10^{-4} \text{ min}^{-1}$ are a measure of bacteria–nutrient and bacteria–bacteria interaction strength, respectively. They do not depend on N_0 and have dimension of inverse time.

To compare our model with the logistic model, the bacterium–bacterium interaction strength is set to zero. For $k_{bb} = 0$ differential equations (14) and (15) reduce to:

$$\frac{d}{dt}b(t) = k_m \cdot q(x) \cdot n(t) \cdot b(t) \quad (17)$$

$$\frac{d}{dt}n(t) = -\frac{d}{dt}b(t). \quad (18)$$

Time dependence of bacterial and nutrients concentrations for this case is given in figure 3. Equation (18) can be written in a form

$$\frac{d}{dt}(n(t) + b(t)) = 0, \quad (19)$$

which gives the solution

$$n(t) + b(t) = 1 + b_0. \quad (20)$$

Inserting (20) into (17) we obtain the differential equation for bacterial concentration

$$\frac{d}{dt}b(t) = k_m \cdot q(x) \cdot b(t) \cdot [1 + b_0 - b(t)]. \quad (21)$$

After separation of variables, equation (21) is solved by integration, which brings the solution

$$b(t) = \frac{1 + b_0}{1 + \frac{1}{b_0} \cdot e^{-k_m \cdot q(x) \cdot (1+b_0) \cdot t}}. \quad (22)$$

The solution (22) can be recognized as a logistic (Verhulst) model [1, 2, 7, 15] for bacterial growth:

$$b(t) = \frac{b_a}{1 + \left(\frac{b_a}{b_0} - 1\right) \cdot e^{-k_v \cdot t}}, \quad (23)$$

where k_v is the logistic growth rate constant and b_a is the maximum population, i.e. the number of bacteria a habitat can support. Comparing expressions (22) and (23), we find the following relationships between the parameters:

$$b_a = 1 + b_0 \quad (24)$$

$$k_v = k_m \cdot q(x) \cdot (1 + b_0). \quad (25)$$

In most experiments inoculum size b_0 is much less than initial nutrient size ($b_0 \ll 1$) so that equation (22) becomes equivalent to the logistic equation (23) with the maximum population equal to the concentration of nutrients, $b_a = 1$. However, unlike equation (23), for larger inoculum sizes our result reveals the fact that the maximum capacity of the habitat should be given by the sum of initial nutrients and bacterial concentrations. This could be important for large b_0 , e.g. if additional nutrients are added to the exhausted culture batch during the stationary or the death phase as in [20]. There is also a difference in the growth rate. The logistic growth rate (25) depends on the initial nutrients dilution factor x and on the inoculum size b_0 . However, this dependence is significant only if the inoculum size b_0 is of the same order of magnitude as the maximal population b_a .

Initial growth rate (for $t = 0$) for the logistic model can be found from (23) as ratio of the derivative of bacterial concentration $b(t)$ at the beginning of the growth and the inoculum size b_0

$$\frac{1}{b_0} \frac{d}{dt}b(0) = k_v \cdot \left(1 - \frac{b_0}{b_a}\right). \quad (23a)$$

We see that, for the logistic model, the growth rate decreases with the inoculum size, i.e. with the ratio b_0/b_a . On the other hand, for our model, after inserting (24) and (25) in (23a) we find

$$\frac{1}{b_0} \frac{d}{dt}b(0) = k_m \cdot q(x), \quad (23b)$$

that the initial growth rate does not depend on the inoculum size.

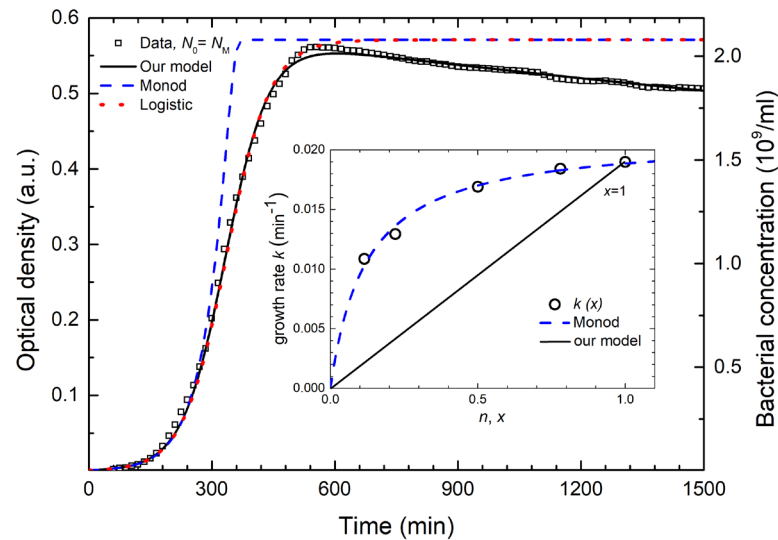


Figure 10. Comparison to other models. Growth curve for the $N_0 = N_M$ sample (squares) is compared with the theoretical fits obtained for our model (solid line), logistic model (dotted line), and Monod model (dashed line). Initial growth rates (circles), obtained from the slopes of the linear fits for each initial nutrients dilution factor x are given in the inset. The inset also shows dependence of growth rate on the nutrients concentration for our model (solid line) and for Monod model (dashed line).

From the proportionality between initial nutrients concentration and maximum OD (see figure 1), we conclude that the growth stops due to the lack of nutrients. Therefore, we found useful to discuss our data in terms of the Monod model which is related to nutrients (substrate) limited growth. For that purpose, we plot the experimental growth data for $x = 1$ sample and theoretical growth curves for related models in figure 10. The circles in the inset are the initial growth rates $k(x)$ obtained from the fitting procedure for different initial nutrients dilution factor x , as described in figure 4.

When discussing the growth rate, it should be noted that it could have different meanings in the literature. For the exponential growth given by equation (4), it is a constant. It is also related to the maximum microbial population, since larger growth rate yields a larger maximum microbial population, as can be observed from figure 1 in Lopez *et al* [3]. More generally, it is assumed that the growth rate is a function of the nutrient concentration $k = k(n)$, and that it declines during the growth, which is mostly related to the decay in nutrients concentration [14, 21–23]. The Monod growth rate function $k(n)$ is given by:

$$k(n) = k_m \frac{n}{n_{1/2} + n}, \quad (26)$$

where k_m is the maximum growth rate and $n_{1/2}$ the nutrients concentration for which the growth rate is half of the maximal, $k(n_{1/2}) = k_m/2$ [14, 21–23]. As seen in the inset of the figure 10, the initial growth rates obtained from different growth curves from figure 4 follow this dependence. Best fit of our data to the Monod function is obtained for $k_m = 0.021 \text{ min}^{-1}$ and $n_{1/2} = 0.121$. These values are close to the values obtained for k_m and $x_{1/2}$, obtained from the parameter $\alpha(x)$ fit. Obviously, there is an excellent agreement

between our data and the Monod fit, as shown in the inset.

The dependence of growth rate on the nutrients concentration given in equation (26) can be compared with the growth rate function for our model for $k_{bb} = 0$. From equation (17) it follows:

$$k(n) = k_m \cdot q(x) \cdot n. \quad (27)$$

We see that the growth rate function is linear, which is typical for the logistic model, with the slope that depends on the initial nutrients dilution factor x . Growth rate function $k(n)$, for $x = 1$ is drawn with the solid line in the inset of the figure 10. If the initial growth rate dependence on the initial nutrients concentration x , obtained from different growth curves (dashed line in the inset), is interpreted as a growth rate dependence on nutrients concentration n during the growth, $k(n) = k(x)$, the growth curve should follow the Monod model, which is not the case for our data.

Discussion

The growth curve for $N_0 = N_M$ sample is compared with the different theoretical models in figure 10. We see that all models well describe the data at the beginning of the growth. The Monod model (dashed line) does not describe the transition to the stationary phase as the data show much slower transition. The slowed-down transition to the stationary phase can be for bacteria growing in colonies, as found by Shao *et al* [24], and described by the modified Monod model. However, our growth curves are obtained for batch culture. Also, according to the literature, this bacterial strain and growth method cannot result in the formation of aggregates [25, 26]. The logistic model (dotted line) overshoots the maximum bacterial

concentration and does not describe the death phase. On the other hand, our model (presented with the solid line) describes all phases of growth. This analysis shows that the Monod model explains the initial growth rate dependence on the initial dilution factor but does not describe the experimental growth curve. Figures 7 and 10 show that our model describes entire growth curves for different dilution factors x but cannot consistently explain the initial growth rates $k(x) = \alpha(x)N_0$ which are not proportional to x . This issue obviously requires further investigation and interpretation.

It should be noted that, due to the experiment design, there is a possibility that the change in the growth rate does not come only from the change of the nutrients concentration. By diluting the medium other constituents are also changed, which can result in additional variables, and influence the growth. However, our data gave proportionality of the maximal population with the initial nutrients concentration which shows that the limited nutrient is the dominant variable in the experiment.

We further elaborate the meaning of the interaction strength parameter $\alpha(x)$ and discuss its dependence on the initial nutrients dilution factor x given in figure 6. This dependence shows that the probability of nutrients uptake (when bacteria encounters nutrients) decreases with the initial dilution factor x . The explanation can be the following. If there is an abundance of nutrients (large x), bacteria will not uptake it at each encounter so that $\alpha(x)$ will be small. On the other hand, for small x , there is a lack of nutrients. So, a bacterium consumes nutrients every time it encounters it, resulting with a large $\alpha(x)$. As our growth curves are described with the $\alpha(t) = \text{const.}$, we conclude that bacteria nutrients uptake does not change significantly during the growth. It seems that bacteria somehow adapt their nutrient uptake frequency in respect to the initial growing conditions which leads to the different maximal populations. The possibility to adapt might be attributed to, e.g., quorum sensing [27] since bacteria use it to determine the population density to anticipate carrying capacity to avoid population collapse [28]. However, *E. coli* DH5 α does not seem to be able to produce signal activity [29].

In our experiments we used LB broth, for which it has been demonstrated that bacterial growth stops due to consumption of all utilizable carbon sources, because after adding glucose, the growth continues [20]. This also indicates that other nutrients in the batch were not exhausted and that the metabolite waste level was not as toxic to induce growth stop.

According to our model, bacterial inactivation is caused by the interaction amongst bacteria which is described by the second term of equation (1). As the nutrients resources are being spent and the exponential growth phase comes to its end, this interaction becomes more noticeable since it increases with the square of bacterial concentration. In other words, the mortality occurs prior to the onset of the visible inactivation phase.

The idea to introduce a negative quadratic term of bacterial concentration to describe bacterial inactivation is different from the ideas found in literature, as e.g. introduction of the waste products variable [15], or negative term proportional to the bacterial concentration [24]. We also found that these models are not convenient for the description of our data. The model presented in [15] includes the waste products as a variable, which we are not able to control/measure, and the model given in [24] is related to the bacterial growth in colonies which are not observed in our samples.

The bacterium–bacterium interaction might comprise different contributions. The positive contribution, probably mediated by the metabolic byproducts, gives rise to β . The negative contribution might arise from bacterial death, since dying bacteria might be a source of nutrients for the rest of the population [30]. The later would result in the reduction of the β . We found that that the higher maximal bacterial concentration leads to the lower bacterial interaction parameter $\beta(x)$, which could be described by the same functional dependence on the initial dilution factor x as parameter $\alpha(x)$. However, a relatively large scattering of $\beta(x)$ data gives $R^2 = 0.89$ for the corresponding fit so that the proposed functional dependence for $\beta(x)$ should be considered with caution. In any case, if the $\beta(x)$ data are expressed by a two-parameter function, it is reasonable to presume that this function has the same rational form as $\alpha(x)$ for which a theoretical explanation can be found.

The dependence of parameter $\alpha(x)$ is equivalent to the Monod dependence of the growth rate $k(x)$ on nutrients concentration. An attempt to explain Monod dependence is given in [23] where a delay for biomass production is taken into account. According to that paper, growth rate is not proportional to the instant bacterial concentration, but to the bacterial concentration some time ago, and that is because the substrate-to-biomass conversion is not instantaneous. Similar consideration can be applied to the negative bacterium–bacterium interaction which could result in the same functional dependence of $\beta(x)$.

The death phase OD data should be discussed with care since OD method cannot distinguish between viable and unviable cells. The OD is expected to decrease only if bacteria disintegrate, which appears sometime after their inactivation. So, we found necessary to do viable cell counting measurements for the death phase. Comparison of the viable plate counting and the OD data for the initial nutrients dilution factor $x = 1$ is given in figure 1. It is noticeable that the decline of bacterial concentration in the mortality phase obtained by viable cell counting is steeper than the one obtained by OD measurements. This could be because the non-viable cells contribute to the OD signal until they completely decompose. Similar observations were made when modeling growth curves obtained for different strain or different growing medium. Details can be found in the supplementary file accompanied by figures S1 and S2.

Our experiments, which included variation of inoculum and initial nutrient concentration, did not induce a lag phase. Modeling of growth curves obtained for different inoculum sizes showed that smaller inoculum sizes result in larger time shifts, because bacteria take longer period of time to reach the same population. Bacterial growth is not seen at the beginning of measurements not because of the lag of the growth, but because of very low cell concentration that cannot be observed by the instrument. We relate the absence of a lag phase with the sample preparation protocol in which the initial growing conditions did not change. The overnight batch culture was transferred to the same fresh medium so that the cells did not need time to metabolically adapt. Note that the lag phase, in which bacteria adapts to the new environment after inoculation, is included in many models of growth [31]. Also, we have shown that the inoculum size variation only induces the time shift of the curve. This is due to the fact that the growth rate $k(x)$ is the same for each growth curve. This observation is in line with the properties of our model that the initial growth rate does not depend on the inoculum size (see equation (23b)).

Conclusion

In this work we study *E. coli* growth by measuring the time change of the sample OD, for different initial nutrients concentrations and different inoculum sizes. For all curves, obtained from the different initial nutrients concentration experiment, the bacterial OD initially increases exponentially, exhibits the maximum for time $t \approx 500$ min and gradually decreases for larger t . The maximum OD decreases proportionally with the initial nutrients dilution factor, suggesting that the growth stop is caused by the lack of the nutrient. The main effect of the inoculum change is a shift of the curve along the time axis without affecting the overall shape of the curve. This shift should not be attributed to the lag phase, which is not observed in our data. The variation of inoculum and initial nutrient concentration did not induce a lag phase. Absence of the lag phase is a very convenient starting point for studying the influence of a bactericide which can induce it.

To analyze the observed data, we introduce a simple growth model which describes the entire growth curve. The bacterial population is described by the two mutually dependent first-order nonlinear differential equations. These equations give the time change of bacteria and the nutrients concentration. Specific for our model, in addition to the usual positive bacteria–nutrients interaction term, which gives the exponential rise and saturation of the bacterial population, is the introduction of the negative bacterium–bacterium interaction term which leads to the population decay. This is a novel mathematical approach for description

of bacterial inactivation and onset of the death phase which can be explained on a microscopic basis. The model can be easily extended to include additional interactions.

If the bacterium–bacterium interaction is neglected, the model reduces to the logistic one with the initial growth rate independent on the inoculum size.

We found that the initial bacteria–nutrients interaction, and related initial growth rate depend on the initial nutrients concentration. This dependence is described with the Monod function. However, it is not equivalent to the growth rate dependence on nutrients concentration during the growth, since the growth curves cannot be described with the Monod model. The growth data are described if the initial bacteria–nutrients interaction strength is kept constant during the growth, which is a characteristic of the logistic model.

We describe a simple method for data analysis and determination of models parameters. The initial growth rates and inoculum sizes are obtained from linear fits of the logarithmic plots of the OD data. The initial nutrients concentration and the bacterium–bacterium interaction strength is found from the linear fits of the inverse data plots. Once the parameters are obtained the entire growth curve is described. This procedure can be used by a researcher with a minimum of mathematical background. The method for accurate determination of the growth rate from the time shifts of growth curves with different inoculum sizes is also presented.

The generality of the model should be tested by applying it to different microbial strains. Also, despite simplicity and interaction-based interpretability of the model, the biochemical interpretation of the parameters is missing and should to be considered. We plan to keep on investigating in this line.

Acknowledgments

The authors would like to thank V Zlatić for helpful discussions. This work was supported by the Ministry of Science and Education of the Republic of Croatia, under the bilateral Croatia-USA agreement on the scientific and technological cooperation, Project No. 1/2014.

ORCID iDs

Lucija Krce  <https://orcid.org/0000-0002-8387-1412>

Matilda Šprung  <https://orcid.org/0000-0001-5008-2700>

Ana Maravić  <https://orcid.org/0000-0001-5235-6656>

Ivica Aviani  <https://orcid.org/0000-0002-5002-388X>

References

- [1] Peleg M and Corradini M G 2011 Microbial growth curves: what the models tell us and what they cannot *Crit. Rev. Food Sci. Nutrition* **51** 917–45
- [2] Peleg M, Corradini M G and Normand M D 2007 The logistic (Verhulst) model for sigmoid microbial growth curves revisited *Food Res. Int.* **40** 808–18
- [3] López S, Prieto M, Dijkstra J, Dhanoa M S and France J 2004 Statistical evaluation of mathematical models for microbial growth *Int. J. Food Microbiol.* **96** 289–300
- [4] Taub I A, Feeherry F E, Ross E W, Kustin K and Doona C J 2003 A quasi-chemical kinetics model for the growth and death of *Staphylococcus aureus* in intermediate moisture bread *J. Food Sci.* **68** 2530–7
- [5] Gibson A M, Bratchell N and Roberts T A 1987 The effect of sodium chloride and temperature on the rate and extent of growth of *Clostridium botulinum* type A in pasteurized pork slurry *J. Appl. Bacteriol.* **62** 479–90
- [6] Zwietering M H, Jongenburger I, Rombouts F M and van 't Riet K 1990 Modeling of the bacterial growth curve *Appl. Environ. Microbiol.* **56** 1875–81
- [7] Fujikawa H, Kai A and Morozumi S 2004 A new logistic model for *Escherichia coli* growth at constant and dynamic temperatures *Food Microbiol.* **21** 501–9
- [8] Gibson A M, Bratchell N and Roberts T A 1988 Predicting microbial growth: growth responses of salmonellae in a laboratory medium as affected by pH, sodium chloride and storage temperature *Int. J. Food Microbiol.* **6** 155–78
- [9] Koutsoumanis K 2001 Predictive modeling of the shelf life of fish under nonisothermal conditions *Appl. Environ. Microbiol.* **67** 1821–9
- [10] Buchanan R, Whiting R and Damert W 1997 When is simple good enough: a comparison of the Gompertz, Baranyi, and three-phase linear models for fitting bacterial growth curves *Food Microbiol.* **14** 313–26
- [11] Baranyi J, Roberts T A and McClure P 1993 A non-autonomous differential equation to model bacterial growth *Food Microbiol.* **10** 43–59
- [12] Baranyi J and Roberts T A 1994 A dynamic approach to predicting bacterial growth in food *Int. J. Food Microbiol.* **23** 277–94
- [13] Hills B P and Mackey B M 1995 Multi-compartment kinetic models for injury, resuscitation, induced lag and growth in bacterial cell populations *Food Microbiol.* **12** 333–46
- [14] Monod J 1949 The growth of bacterial cultures *Annu. Rev. Mater.* **3** 371–94
- [15] Sakanoue S 2007 Extended logistic model for growth of single-species populations *Ecol. Modell.* **205** 159–68
- [16] Peleg M and Shetty K 1997 Modeling microbial populations with the original and modified versions of the continuous and discrete logistic equations *Crit. Rev. Food Sci. Nutrition* **37** 471–90
- [17] Jones J E, Walker S J, Sutherland J P, Peck M W and Little C L 1994 Mathematical modelling of the growth, survival and death of *Yersinia enterocolitica* *Int. J. Food Microbiol.* **23** 433–47
- [18] Xiong R, Xie G, Edmondson A E and Sheard M A 1999 A mathematical model for bacterial inactivation *Int. J. Food Microbiol.* **46** 45–55
- [19] Bevilacqua A, Speranza B, Sinigaglia M and Corbo M 2015 A focus on the death kinetics in predictive microbiology: benefits and limits of the most important models and some tools dealing with their application in foods *Foods* **4** 565–80
- [20] Sezonov G, Joseleau-Petit D and D'Ari R 2007 *Escherichia coli* physiology in luria-bertani broth *J. Bacteriol.* **189** 8746–9
- [21] Kovárová-Kovar K and Egli T 1998 Growth kinetics of suspended microbial cells: from single-substrate-controlled growth to mixed-substrate kinetics *Microbiol. Mol. Biol. Rev.* **62** 646–66
- [22] Bren A, Hart Y, Dekel E, Koster D and Alon U 2013 The last generation of bacterial growth in limiting nutrient *BMC Syst. Biol.* **7** 27
- [23] Lobry J, Flandrois J, Carret G and Pave A 1992 Monod's bacterial growth model revisited *Bull. Math. Biol.* **54** 117–22
- [24] Shao X, Mugler A, Kim J, Jeong H J, Levin B R and Nemenman I 2017 Growth of bacteria in 3-d colonies *PLoS Comput. Biol.* **13** e1005679
- [25] Kragh K N et al 2017 The inoculation method could impact the outcome of microbiological experiments *Appl. Environ. Microbiol.* **84** 1–14
- [26] Chart H, Smith H R, La Ragione R M and Woodward M J 2000 An investigation into the pathogenic properties of *Escherichia coli* strains BLR, BL21, DH5alpha and EQ1 *J. Appl. Microbiol.* **89** 1048–58
- [27] Waters C M and Bassler B L 2005 Quorum sensing: cell-to-cell communication in bacteria *Annu. Rev. Cell. Dev. Biol.* **21** 319–46
- [28] An J H, Goo E, Kim H, Seo Y-S and Hwang I 2014 Bacterial quorum sensing and metabolic slowing in a cooperative population *Proc. Natl Acad. Sci.* **111** 14912–7
- [29] Surette M G 1998 Quorum sensing in *Escherichia coli* and *Salmonella typhimurium* *Proc. Natl Acad. Sci.* **95** 7046–50
- [30] Schink S J, Biselli E, Ammar C and Gerland U 2018 Maintenance cost and biomass recycling determine fitness of *E. Coli* during starvation *SSRN Electron. J.* submitted (<https://doi.org/10.2139/ssrn.3255561>)
- [31] Swinnen I A M, Bernaerts K, Dens E J J, Geeraerd A H and Van Impe J F 2009 Predictive modelling of the microbial lag phase: a review *Int. J. Food Microbiol.* **94** 137–59






III. BACTERIA EXPOSED TO SILVER NANOPARTICLES SYNTHESIZED BY LASER ABLATION IN WATER: MODELLING *E. COLI* GROWTH AND INACTIVATION

Reproduced from:

Krce L, Šprung M, Maravić A, Umek P, Salamon K, Krstulović N, Aviani I. Bacteria Exposed to Silver Nanoparticles Synthesized by Laser Ablation in Water: Modelling *E. coli* Growth and Inactivation. *Materials* (Basel) 2020;13:653. <https://doi.org/10.3390/ma13030653>.

Article

Bacteria Exposed to Silver Nanoparticles Synthesized by Laser Ablation in Water: Modelling *E. coli* Growth and Inactivation

Lucija Krce ^{1,*}, Matilda Šprung ², Ana Maravić ³, Polona Umek ⁴, Krešimir Salamon ⁵,
Nikša Krstulović ⁶ and Ivica Aviani ¹

¹ Faculty of Science, Department of Physics, University of Split, Ruđera Boškovića 33, 21000 Split, Croatia; iaviani@pmfst.hr

² Faculty of Science, Department of Chemistry, University of Split, Ruđera Boškovića 33, 21000 Split, Croatia; msprung@pmfst.hr

³ Faculty of Science, Department of Biology, University of Split, Ruđera Boškovića 33, 21000 Split, Croatia; amaravic@pmfst.hr

⁴ Jožef Stefan Institute, Jamova cesta 39, 1000 Ljubljana, Slovenia; polona.umek@ijs.si

⁵ Ruđer Bošković Institute, Bijenička cesta 54, 10 000 Zagreb, Croatia; Kresimir.Salamon@irb.hr

⁶ Institute of Physics, Bijenička cesta 46, 10000 Zagreb, Croatia; niksak@ifs.hr

* Correspondence: lkrce@pmfst.hr

Received: 8 January 2020; Accepted: 30 January 2020; Published: 1 February 2020



Abstract: This study is aimed to better understand the bactericidal mode of action of silver nanoparticles. Here we present the production and characterization of laser-synthesized silver nanoparticles along with growth curves of bacteria treated at sub-minimal and minimal inhibitory concentrations, obtained by optical density measurements. The main effect of the treatment is the increase of the bacterial apparent lag time, which is very well described by the novel growth model as well as the entire growth curves for different concentrations. The main assumption of the model is that the treated bacteria uptake the nanoparticles and inactivate, which results in the decrease of both the nanoparticles and the bacteria concentrations. The lag assumes infinitive value for the minimal inhibitory concentration treatment. This apparent lag phase is not postponed bacterial growth. It is a dynamic state in which the bacterial growth and death rates are close in value. Our results strongly suggest that the predominant mode of antibacterial action of silver nanoparticles is the penetration inside the membrane.

Keywords: laser synthesis of nanoparticles; silver nanoparticles; antibacterial activity; modeling bacterial growth

1. Introduction

Antimicrobial resistance, being a global health problem [1], has been and currently is, an excellent motivator in the research of the antimicrobial activity of silver compounds, especially silver nanoparticles (AgNPs) [2–6]. The high surface-area-to-volume ratio of nanoparticles (NPs) provides different physical and chemical characteristics of NPs in comparison to bulk material or larger particles [7]. Many metallic and metallic oxide NPs show bactericidal potential towards different bacterial strains [7], but silver nanoparticles attract the most attention partially due to the antimicrobial activity of Ag⁺ ions [8]. Silver nanoparticles have been proven to be an excellent antibacterial agent against Gram-negative bacteria and a mild antibacterial agent against Gram-positive bacteria, possibly due to differences in their membrane structure [4]. They are widely available for purchase or are chemically produced [9–11]. Their bactericidal effect depends on their size [3], concentration [9],

shape [2] and surface properties [8]. It has also been shown that AgNPs enhance the antibacterial potential of antibiotics compared to the drugs alone [12,13]. Reports of the impact of AgNPs on human health are still not numerous and are inconclusive as stated in the review paper [14]. It has been shown that toxicity also depends on the physicochemical properties of nanoparticles [15] so it might be difficult to compare between toxicity research of AgNPs with different shapes and sizes at different concentrations.

However, significantly fewer reports on the bactericidal effect of nanoparticles produced by laser ablation in liquid (LAL) exist [16–19]. This technique, known as a ‘green synthesis’ technique [20], although other types of synthesis are considered to be green [21], enables nanoparticle production without chemical byproducts and stabilizing molecules [22].

The mode of antibacterial action of AgNPs is still not resolved [23] though many mechanisms incorporate the release of silver ions while some report formation of pits in the cell wall due to the nanoparticles accumulation [24]. It was reported that the mode of action is size-dependent: the bactericidal effect of AgNPs smaller than 10 nm is due to the nanoparticles, but the predominant mechanism of the larger ones might be the release of silver ions [25].

A bacterial cell concentration, as a function of time, obtained in a closed habitat, yields a growth curve generally consisting of four distinctive phases: lag phase, exponential phase, stationary phase and mortality phase as depicted in [26]. The lag phase, the delay of the exponential growth arising due to the changed growth conditions, has been a center of attention of many primary growth models [27–29]. This phase also seems to be induced when bacteria are treated at different sub-minimal inhibitory concentration (MIC) values of antibacterial substances [30–33], including silver ions and silver nanoparticles [11,34–36]. Commonly used approaches for bacterial growth modeling are the empirical Gompertz [37] and the rate logistic (Verhulst) models [26]. Scarce attempts have been made in modeling the bacterial growth in the presence of silver nanoparticles [38,39]. Recently published work [38] introduced a modified Gompertz model for bacterial isothermal growth data obtained at various AgNPs concentrations but without any interpretation at the microscopic level.

A relatively rarely investigated antibacterial mode of action of LAL-synthesized silver colloid, which is considered to be free of chemical byproducts, has a potential to reveal its bactericidal action without irrelevant or uncontrollable parameters. This has been our main motivation for this research.

We have synthesized silver nanoparticles by laser ablation, treated *E. coli* (*Escherichia coli*) and subsequently tracked the bacterial cell number in time through the optical density (OD) of the batch culture. We have aimed to explain the obtained OD growth curves of *E. coli* treated with different concentrations of laser produced AgNPs through modeling. Our objective was not just to give a mathematical description of the curves, but also, according to the modeling approach at a microscopic level, to explain the bacterial growing and dying mechanisms. We extended our model for non-treated *E. coli* cells [40], and described the bacterial growth through the system of three differential equations. These equations give the time change of bacterial, nutrients and nanoparticles concentrations. The model enabled us to understand the obtained growth phases, particularly the apparent lag phase and to propose the mode of antibacterial action of LAL-synthesized AgNPs which is one of the main prerequisites for efficient clinical trials and drug development. According to our knowledge, this approach has not been exploited.

2. Materials and Methods

2.1. Silver Colloid Production

Colloidal AgNPs were synthesized by laser ablation of silver target (purity >99.99%, GoodFellow, Huntingdon, UK) immersed in deionized water. The experimental setup is shown schematically in [41]. The silver target was immersed in a 30 mL beaker containing 25 mL of deionized water, while the water thickness above the target surface was 2 cm. The thickness of the water layer was kept constant during the laser ablation in order to keep the laser ablation efficiency constant [42]. The target was

irradiated by a Nd:YAG laser using fundamental wavelength of 1064 nm and the laser pulse energy delivered to the target was 100 mJ giving fluence of 10 J/cm². The number of delivered pulses was 5000 with the repetition rate of 5 Hz. The laser pulse was focused on the target surface using a 10 cm lens. The focal plane position was corrected after each 1000 pulses as the index of refraction of the produced colloid changed with the time of processing. This procedure was repeated four times in order to obtain 100 mL of colloid.

2.2. Silver Colloid Characterization

To determine the nanoparticle size, concentration, stability, composition and structure, the following measurements were performed.

The total volume of all AgNPs in the colloid was obtained from the volume of the craters that were created on the target surface during the laser ablation process. In order to determine the crater's volume, the craters were studied with an optical microscope (Leitz Aristomet, Leica, Wetzlar, Germany) in a reflective illumination mode.

The ultraviolet-visible (UV-VIS) spectrum of synthesized Ag colloidal solutions was recorded in the wavelength range from 190–1100 nm using a UV-VIS spectrophotometer (Lambda 25, Perkin Elmer, Waltham, Massachusetts, USA).

Particles' sizes and zeta potentials were determined by dynamic (DLS) and electrophoretic light scattering, respectively, using a Zetasizer Ultra (Malvern Panalytical, Malvern, UK). To avoid overestimation arising from the scattering of larger particles, the average particle size was obtained as the value at peak maximum of the number size distribution. The reported results are average of 10 measurements. The zeta potential result is reported as an average value of three measurements. The data processing was done by a ZS Xplorer 1.20 (Malvern Panalytical, Malvern, UK).

In order to perform structural characterization, the produced colloid was applied to a silicon substrate and left to air dry. This procedure was repeated several times resulting in an Ag film. The crystalline structure of the Ag films was investigated using a D5000 diffractometer (Siemens, Munich, Germany) in parallel beam geometry with Cu K α radiation, a point detector and a collimator in front of the detector. Grazing incidence X-ray diffraction (GIXRD) scans were acquired with the constant incidence angle α_i of 1°, guaranteeing that the information contained in the collected signal covers the entire film thickness.

The morphology of the sample was investigated with a transmission electron microscope (TEM) (Jeol 2100, 200 kV, Jeol, Tokyo, Japan). For TEM analyses, a specimen was prepared by adding 0.5 mL of the colloid to 0.5 mL of methanol and ultra-sonicated for a few minutes. Then one drop of the obtained dispersion was deposited on a lacey carbon film supported by a copper grid and dried in air. TEM nanoparticle size distribution was obtained by measuring the diameter of over 850 nanoparticles.

The specimen preparation for the atomic force microscopy (AFM) (Multimode 3, Digital Instruments/Bruker, Billerica, Massachusetts, USA) started by applying 5 μ L of the colloid on a freshly cleaved mica sheet. The specimen was then left to air dry for 30 min. Imaging was done in contact mode at ambient conditions with probes having nominal spring constants of 0.12 N/m and 0.06 N/m (DNPS-10, Bruker, Billerica, Massachusetts, USA). AFM height images were analyzed using Gwyddion, an open source software for AFM data analysis. Height of each nanoparticle was taken as its diameter. Height measurements of over 170 nanoparticles yielded the particles size distribution.

Zeta potential, DLS and UV-VIS spectrum measurements were done immediately after the LAL synthesis, while the GIXRD measurements and microscopy studies were performed a few days later.

2.3. Minimal Inhibitory and Bactericidal Concentrations

To determine the minimal inhibitory concentration and the minimal bactericidal concentration the following experimental method and materials were used. The in vitro antibacterial activity of the synthesized Ag colloid was tested against the Gram-negative *E. coli* DH5 α (kindly provided by Janoš Terzić Lab, School of Medicine, University of Split, Croatia).

DH5 α is commonly used laboratory *E. coli* strain to maintain and amplify small plasmid DNA [43]. More importantly, it is often used in fundamental research of a wide range of new potential antibacterials [44–47] and even for the production of silver nanoparticles upon transformation [48]. Additionally, it seemed reasonable to model growth curves of this strain since we have thoroughly investigated its growth parameters [40].

Antibacterial activity was evaluated using the microdilution method according to the Clinical and Laboratory Standards Institute guidelines [49] and performed in 96-well microtiter plates. Nutritionally impoverished Luria-Bertani (LB) broth (5.0 g of tryptone, 2.5 g of yeast extract, and 5.0 g of NaCl per 1 L of deionized sterile water) was used in all experiments. This medium will be further referred as the master medium. An overnight culture of *E. coli* DH5 α was diluted in the fresh master medium and grown for 60 min. Aliquots of bacterial suspension (50 μ L) corresponding to 10^6 colony forming units per milliliter (CFU/mL) were added to 50 μ L of serial dilutions of the synthesized Ag colloid to a final load of 5×10^5 CFU/mL per well. The silver colloid was briefly ultra-sonicated before adding it to the bacterial culture. Plates were incubated at 37 °C for 18 h before visual inspection. The MIC was read as the lowest concentration of the substance, showing no turbidity in the wells. For the minimal bactericidal concentration (MBC) determination, aliquots were taken from the wells corresponding to MIC and $2 \times$ MIC and then plated on Mueller-Hinton agar (Biolife, Monza, Italy). After the incubation for 18 h at 37 °C, the MBC value was recorded as the concentration which caused ~99.9% of mortality in the starting inoculum.

2.4. Optical Density Measurements

The microdilution method showed that the MIC value corresponded to the AgNPs concentration obtained at the 50% colloid volume share of the plate well. The bacteria were subsequently treated with different AgNPs concentrations (colloid volume shares) that were close to the MIC value. Growth curves of the treated bacteria were obtained by OD595 (optical density at 595 nm) measurements in a microtiter plate reader (BioTek ELx808 and BioTek Synergy HTX, BioTek Instruments, Winooski, Vermont, USA). Bacterial culture was prepared for the treatment as was for the MIC experiments. The colloid was added to each plate well so that it constituted 3% to 63% of the sample volume, while the rest of the volume consisted of bacterial suspension in the master medium. Before adding it to the bacterial suspension, the colloid was briefly ultrasonically agitated. The inoculum was kept at 5×10^5 CFU/mL for all wells. The plate was shaken constantly at 37 °C. The OD was measured every 15 min for 24 h. All OD measurements were performed in triplicates. In order to obtain the bacterial concentration, the OD data were calibrated by viable cell counting. We found that 1 absorbance unit (a.u.) corresponds to 3.64×10^9 CFU/mL.

2.5. Statistical Analysis

All experimental OD data were obtained in triplicate, and the results were expressed as the mean values and the maximal relative standard deviation was obtained for all growth curves. To compare the experimental data with the theoretical model, we have calculated the theoretical OD values for each experimental OD time point. The linear correlation between the corresponding experimental and theoretical data was quantified by Pearson correlation coefficient which was calculated for each couple of curves. The statistical analysis was performed using Microsoft Excel (Microsoft Office 2016, Microsoft Corporation, Redmond, Washington, DC, USA).

3. Experimental Results

3.1. Colloid Characterization

The volume of a crater created during ablation was determined from a crater's semi-profile as described in detail in [50]. Using this procedure, an average crater's volume was determined since the colloidal suspension was made by four ablation procedures. The calculated average volume was

$5.2 \pm 0.8 \times 10^6 \mu\text{m}^3$ giving the total ablated volume in 4 craters $V_{\text{tot}} = 2.1 \pm 0.3 \times 10^7 \mu\text{m}^3$, which corresponded to the total volume of synthesized AgNPs. The ablated mass was dispersed in 100 mL of deionized water giving the mass concentration of $220 \pm 32 \mu\text{g/mL}$.

Figure 1a shows an average UV–VIS spectrum for the four samples of silver colloids. The spectrum exhibits a sharp absorption peak in the visible range due to nanoparticle's surface plasmon band [51]. The obtained maximum at 404 nm is typical for silver spherical stable colloidal nanoparticles in the diameter range of about 10 nm [52]. The zeta potential of nanoparticles is, as generally accepted, a measure of its stability [19], and for suspensions that are stabilized by electrostatic repulsion is required to be ± 30 mV at least [53]. Zeta potential of the produced silver colloidal solution was $-(53.1 \pm 1.1)$ mV.

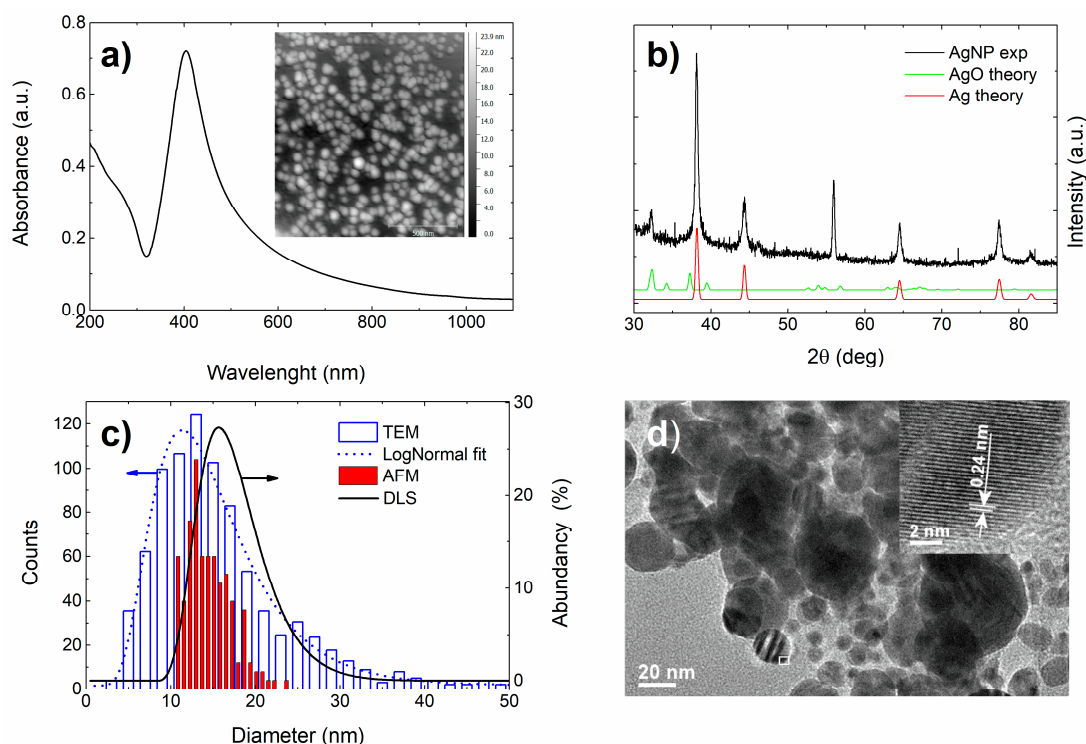


Figure 1. (a) UV–VIS photoabsorption spectrum of AgNPs exhibits a prominent characteristic peak at about 400 nm. The inset shows an AFM height image of a dried-out colloid sample revealing spherical shape of AgNPs, (b) GIXRD pattern obtained from AgNPs. Simulated patterns for the fcc-Ag and AgO phases are shown at the bottom. The peak at $2\theta = 56^\circ$ originates from the monocrystalline silicon substrate, (c) Size-distribution of AgNPs obtained from AFM images (red full column bar) with counts multiplied by a factor of 4 for better visibility and from TEM images (blue column bar) with the corresponding log-normal fit (blue dotted curve). The black full curve represents the size distribution obtained from the DLS measurements, (d) TEM image of AgNPs. The high-resolution TEM inset indicates the crystalline nature of AgNPs. The inset was taken in the area marked by a white frame.

Figure 1b shows the GIXRD pattern for the Ag film together with the simulations for the fcc-Ag and the silver-oxide phases. The measured pattern matches with the fcc-Ag phase (ICDD card no. 00-004-0783). The appearance of all major Bragg peaks of Ag phase evidences randomly-oriented Ag crystallites. A relatively weak Bragg peak at $2\theta = 32.18^\circ$ proves that only a very small fraction of AgNP was oxidized.

The results of TEM analysis, presented in Figure 1d, support AFM (inset in Figure 1a) findings showing that the AgNPs are spherical-like. As seen in Figure 1c, their diameters were found mostly in the range from 3 nm to 40 nm (very rarely nanoparticles of up to 250 nm can be found). Nanoparticles are crystalline (inset to Figure 1), measured d-spacing of 0.24 nm corresponds to the (111) planes of Ag (ICDD card no. 00-004-0783) what is in the line with GIXRD findings. The AFM size distribution

(Figure 1c) is obtained by measuring the height of the AgNPs (equal to the nanoparticle's diameter, z-axis) since the lateral dimensions are not to be taken into account due to the AFM tip dilation [54]. An average AgNP diameter obtained from the AFM images is 13.1 nm, while the TEM images revealed the diameter to be 11.3 nm (the discrepancy is possibly due to better resolution of the TEM microscope).

DLS measurements reveal that the dynamic AgNP diameter is 15.6 nm (black line given in Figure 1c). However, all size distributions are relatively broad ranging from about 3 nm to 50 nm with the maximum at around 10–15 nm. The TEM size-distribution follows a log-normal (LogN) distribution fit represented by the blue dotted line. LogN fit is often used to describe the size-distribution of NPs synthesized from gaseous phase, which is the case in NP synthesis by LAL. It is applied whenever particle growth depends on the diffusion and drift of atoms to a growth zone of the nanoparticles [55], while the final distribution is determined with the available growth time of the nanoparticles [56]. The average volume of a single nanoparticle can be determined from the average diameter of the NPs. Dividing the ablated volume of silver, dispersed in 100 mL of water, by the average nanoparticle volume, one obtains the concentration of AgNPs to be $1.2 \pm 0.2 \times 10^{11} \text{ mL}^{-1}$ as obtained from the TEM diameter. The procedure of how to determine the nanoparticle concentration is described in detail in [57].

3.2. Bacteria Treatment Results

The MIC and MBC values obtained by the microdilution assay for the produced Ag colloid against *E. coli* DH5 α were resolved to be $(110 \pm 16) \mu\text{g/mL}$. To study how a near-MIC treatment influences bacterial growth, the OD growth experiments were made. The raw OD bacterial growth data at 595 nm for the eight sub-MIC and MIC treatments are given in Figure 2a, where the OD signal is proportional to the concentration of bacteria. The maximal relative standard deviation for the three replicates was 4.5% of the OD signal for all growth curves. The numbers given in the legend are the volume shares v of the colloid in the batch culture, and are proportional to the concentration of the NPs. The concentration of the NPs for each treatment is obtained by multiplying the concentration of NPs in the produced colloid by v . As seen in Figure 2a, the main effects of increasing the AgNPs concentration are: increase of the baseline, increase of the bacterial lag time and the reduction of the maximal OD.

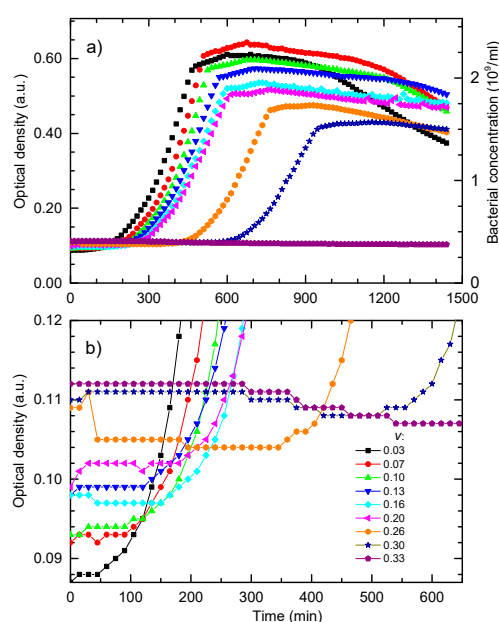


Figure 2. (a) Growth data of *E. coli* treated with different concentrations of silver nanoparticles, i.e., different colloid volume shares v . The OD in absorbance units is given on the left axis and the corresponding bacterial concentrations in CFU/mL are given on the right axes. (b) The first 650 min of the experimental OD data given in Figure 2a.

The growth curve for $v = 0.30$ exhibits the lowest maximal OD and the largest lag time. For $v \geq 0.33$ bacterial growth is completely suppressed, that is when the NPs concentration in the batch exceeds the value of $73 \pm 11 \mu\text{g/mL}$. This value is close to the MIC/MBC obtained by microdilution. Note that, for the microdilution assay, a serial dilution of the produced colloid was made, thus reducing the AgNPs concentration in the successive wells by the factor of 2. In comparison, the OD data gave finer and more accurate results.

The details of the first 650 min of growth are shown in Figure 2b. They reveal the bacterial population dynamics during the lag phase. Growth curves obtained for bacteria treated with higher concentrations of NPs show an increase of the initial optical density and appearance of the minimum in the OD before the growth of bacteria prevails. The bacterial inactivation curve obtained for $v = 0.33$ exhibits a constant decrease in the OD.

The OD data given in Figure 2a,b have motivated us to develop a model of bacterial growth in the presence of the antimicrobial agent.

4. Model Evolution

The model we apply here is an extension of the interaction-based model that successfully describes growth and inactivation of untreated *E. coli* cells [40]. The sketch of the model's mechanism, i.e., included interactions within the system when bacteria are treated with the AgNPs, is given in Figure 3. Bacteria consume nutrients and divide which leads to the increase of the bacterial concentration $B(t)$ and the decrease of the nutrients concentration $N(t)$. Bacteria also interact with the nanoparticles which leads to the decrease of the AgNPs concentration $P(t)$ and the bacterial concentration $B(t)$. We find convenient to express both $N(t)$ and $P(t)$ in bacteria-equivalent units, that is in "packages" per bacterium as described below.

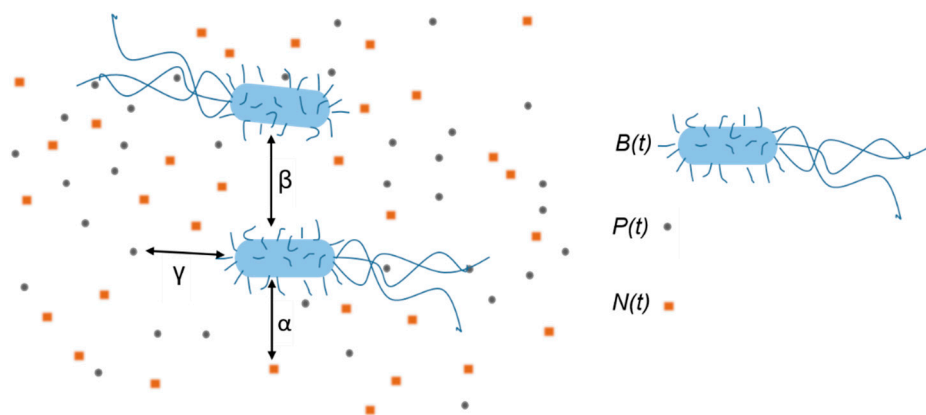


Figure 3. The schematic representation of the batch system as described by our model. The squares and circles represent the nutrients and nanoparticles “packages” that correspond to a single bacterium creation or inactivation, respectively. Interactions are represented by double-head arrows and marked by their interaction strengths α , β , and γ . They describe the following occurrences: Bacteria (i) consume the nutrients, (ii) interact with other bacteria, and (iii) they uptake nanoparticles.

If m_N/V is the mass concentration of nutrients, where m_N is the mass of nutrients and V the volume of the sample, and m_{N1} is the quantity of nutrients needed for a single bacterium growth, then $N(t) = (m_N/m_{N1})/V$ is concentration of the bacteria that could be produced with the given nutrients concentration. Similarly, if N_p/V is the concentration of AgNPs, where N_p is the number of the AgNPs in the sample and N_{p1} is their number needed for a single bacterium inactivation, then $P(t) = (N_p/N_{p1})/V$ is the concentration of the bacteria that could be inactivated with the given concentration of AgNPs.

The bacterium-nutrient interaction strength α and bacterium-nanoparticle interaction strength γ describe the positive influence of the nutrients and the negative influence of the AgNPs on the bacterial population, respectively. The bacterium-bacterium interaction strength β describes the

negative bacterial influence on the bacterial growth such as: the presence of metabolite waste, bacterial competition for nutrients, and possibly lack of space. The model is mathematically expressed by the system of three mutually dependent non-linear differential equations:

$$\frac{d}{dt}B(t) = \alpha \cdot B(t) \cdot N(t) - \beta \cdot B(t)^2 - \gamma \cdot B(t) \cdot P(t) \quad (1)$$

$$\frac{d}{dt}N(t) = -\alpha \cdot B(t) \cdot N(t) \quad (2)$$

$$\frac{d}{dt}P(t) = -\gamma \cdot B(t) \cdot P(t). \quad (3)$$

The first equation describes the time change of the bacterial concentration. The bacterial concentration increases due to the presence of nutrients, and decreases due to the presence of other bacteria and AgNPs. The second and third equations describe the decrease of nutrients and AgNPs concentrations in time, respectively, with the presumption that their concentration is changed only because of the bacterial consumption. If the concentration of nutrients is changed only because of the bacterial consumption, then the number of bacteria produced in unit of time should reduce the number of the nutrients packages for the same amount. This assumption is taken into account by putting the same coefficient α in Equations (1) and (2). The corresponding rates of change are equal in size but opposite in sign. Similarly, if the colloid is stable, the concentration of AgNPs is changed only because of bacterial uptake. The list of the parameters included in the model is as follows:

t —time

$B(t)$ —bacterial concentration

B_0 —inoculum size

$N(t)$ —nutrients concentration

N_M —master growth medium nutrients concentration

$P(t)$ —AgNPs concentration

P_M —produced colloid AgNPs concentration

x —initial nutrients dilution factor

v —initial volume shares of the colloid

$\alpha(x)$ —bacterium–nutrients interaction strength parameter

$\beta(x)$ —bacterium–bacterium interaction strength parameter

γ —bacterium–nanoparticle interaction strength

The number of bacteria inactivated in a unit of time, due to the AgNPs, should reduce the number of the AgNPs packages for the same amount, which is taken into account by putting the same coefficient γ in Equations (1) and (3). The bacterial growth is determined by the initial bacterial concentration (inoculum) $B(0)$, initial concentration of nutrients “packages” $N(0)$ and initial nanoparticles “packages” concentration $P(0)$. In our experiments, the inoculum was kept constant, while the AgNPs concentration was changed by mixing the appropriate volume V_P of the colloid, that has the AgNPs concentration P_M , with the volume of the appropriately inoculated master growth medium V_N , that has nutrients concentration N_M , so that the total volume of the batch culture $V = V_N + V_P$ is kept constant. In this way, the initial volume shares of the colloid $v = V_P/V = P(0)/P_M$ and of the growth medium $x = V_N/V = N(0)/N_M$ are varied so that the condition:

$$x + v = 1 \quad (4)$$

is fulfilled. Therefore, the initial conditions are defined by Equations (5)–(7):

$$B(0) \equiv B_0 \quad (5)$$

$$P(0) = P_M \cdot v \quad (6)$$

$$N(0) = N_M \cdot x = N_M \cdot (1 - v). \quad (7)$$

In our previous work [40], we found that the interaction strengths α and β depend on the initial nutrients concentration with the dependence in the form of a rational function $const./(0.093 + x)$. For our system, the best fits are obtained for $\alpha = \alpha(x) = (0.0295 \text{ min}^{-1} \cdot \text{a.u.})/(0.093 + x)$ and $\beta = \beta(x) = (0.00045 \text{ min}^{-1} \cdot \text{a.u.})/(0.093 + x)$. According to Equation (4), α and β can also be expressed in terms of the initial colloid volume share v giving $\alpha(v) = (0.0295 \text{ min}^{-1} \cdot \text{a.u.})/(0.093 + 1 - v)$ and $\beta(v) = (0.00045 \text{ min}^{-1} \cdot \text{a.u.})/(0.093 + 1 - v)$.

Solutions of Equations (1)–(3), for $B_0 = 0.0025 \text{ a.u.}$, $N_M = 0.57 \text{ a.u.}$, $P_M = 0.05 \text{ a.u.}$, $v = 0.33$, $\gamma = 1.65$ and $\beta = 0$ are plotted in Figure 4. As will be shown latter, these values correspond to the experimentally observed OD data obtained for the MIC treated culture. Note that all concentrations are expressed in terms of a.u., so that calculated values can be compared to the experimental data. In order to make the NPs' concentration change visibly on the given scale, the $P(t)$ data were multiplied by a factor of 10. Additionally, to emphasize the main results of the model, parameter β , which is responsible for the population decay in the death phase, is set to zero. At the beginning, the bacterial concentration slightly decreases, then acquires a broad minimum and then slowly increases, so that the bacterial population remains below the inoculum size up to 1000 min approximately. In that period, both the nutrients and the NPs' concentrations decrease, exhibiting similar functional dependence. Obviously, a dynamic equilibrium exists in which approximately an equal number of bacteria divide, because of the nutrients consumption, and die due to the uptake of the nanoparticles. The exponential bacterial growth appears only if the concentration of nanoparticles falls below some critical value. As a result of that process, the exponential growth phase is significantly postponed. For $t > 1000 \text{ min}$, the onset of that process, the exponential growth phase is seen and the stationary phase is reached for $t > 2000 \text{ min}$.

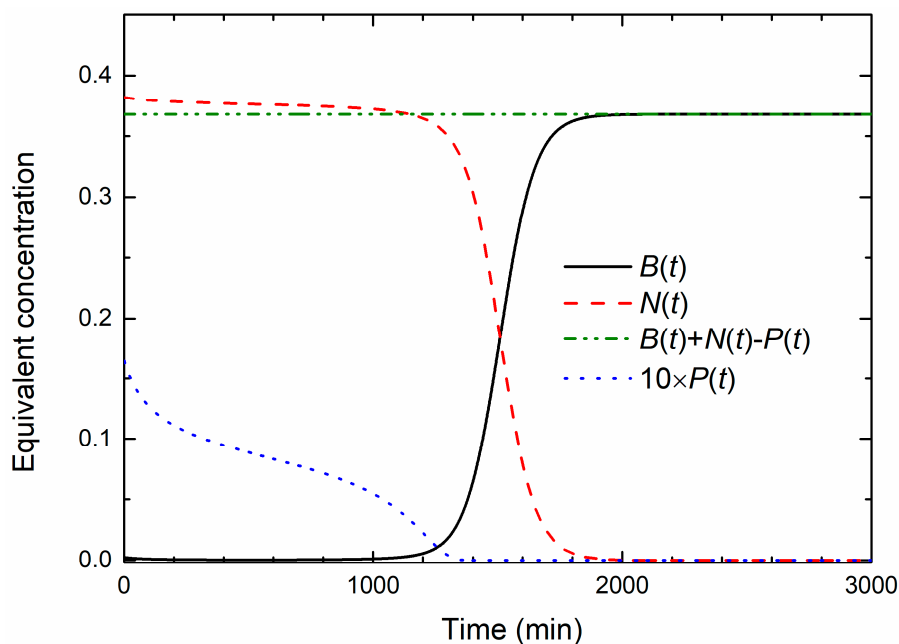


Figure 4. Time change of bacterial concentration $B(t)$ and the equivalent concentrations of nutrients $N(t)$ and nanoparticles $P(t)$ as obtained from the solution of Equations (1)–(3). Note the conservation of the total growth capacity $B(t) + N(t) - P(t) = const.$

As seen from Figure 4, the sum $B(t) + N(t) - P(t) = const.$ holds at all times during the growth. This sum is also the final concentration of the bacterial population; thus it represents the total capacity of the system.

To further elucidate the proposed model, it is useful to inspect the bacterial growth behavior upon treatment with different initial NPs concentrations. Figure 5a shows bacterial growth curves calculated

for different NPs concentrations while all other parameters were the same as for the data given in Figure 4. Bacterial growth for non-treated cells is represented by the full curve. The growth curves for several sub-MIC concentrations show that the main effect of the NPs concentration increase is the delay of the exponential growth phase. For volume share $v = 0.345$ given in dotted curve, bacteria do not go into the exponential phase. This behavior is in accordance with the experimental data given in Figure 2.

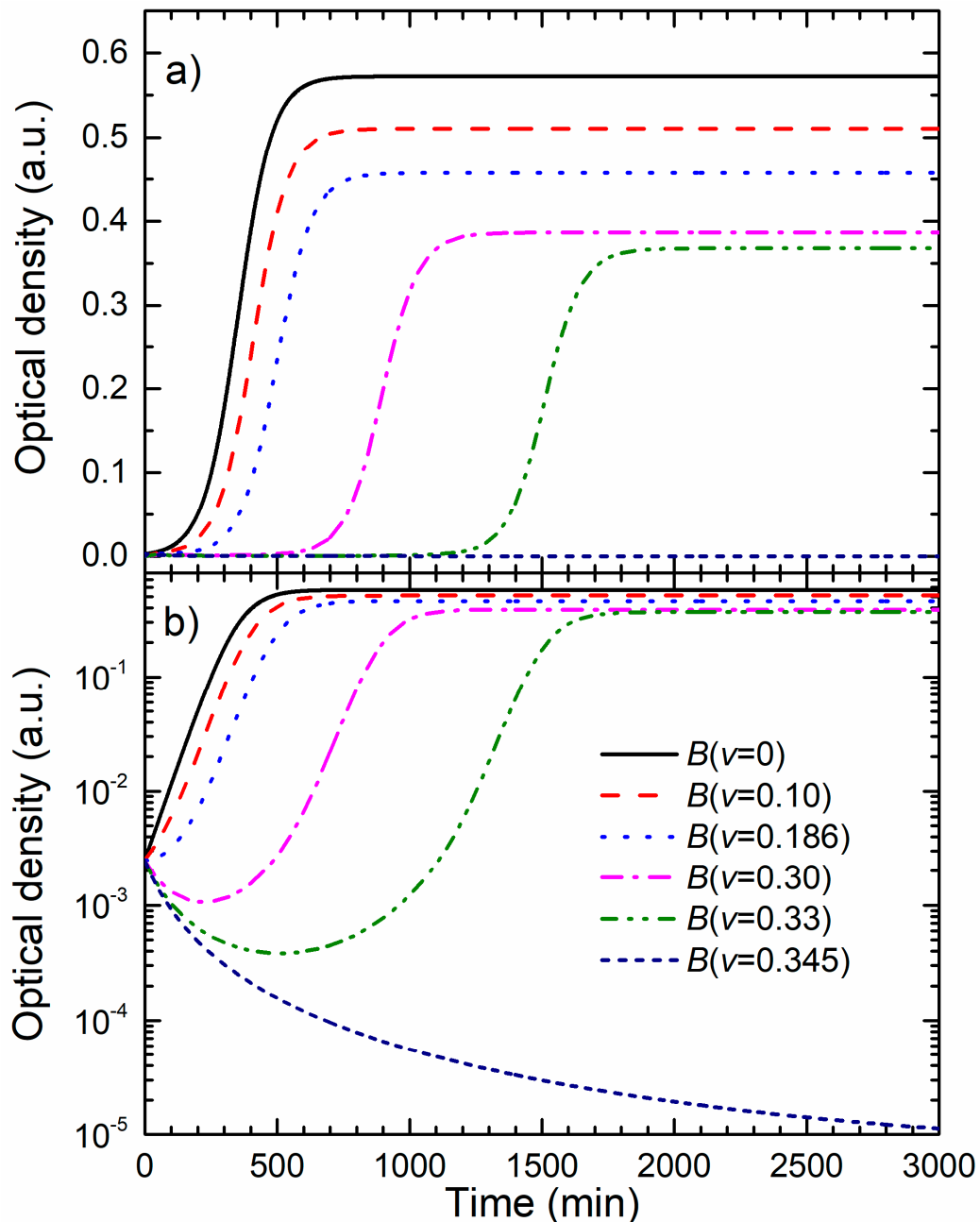


Figure 5. (a) Bacterial population obtained from solutions of Equations (1)–(3) for $\beta = 0$ for different colloid volume shares v . The increase of the colloid volume share reduces the maximal bacterial concentration and postpones the exponential bacterial growth. (b) The same data given in logarithmic scale, exhibiting the population dynamic of the lag phase.

The decrease of the maximal population size with the increase of the colloid volume share is mostly related to the dilution of the master growth medium and the decrease of the initial nutrients concentration, i.e., the total growth capacity.

Figure 5b shows the growth data from Figure 5a presented in the logarithmic OD scale. In this representation, it can be found that the postponed exponential bacterial growth is not a classic lag in which bacteria do not divide. This state can be characterized as a dynamic lag phase that is close to the steady state because the bacterial growth rate is close to the bacterial death rate. As expected, cells in the non-treated sample grow exponentially from the beginning, and the exponential growth of the cells treated with the colloid volume shares of 0.10 and 0.186 is postponed.

For higher nanoparticle concentrations, $v = 0.30$ and $v = 0.33$, the bacterial population firstly decreases, and develops a broad minimum, before the exponential growth prevails. The minimum is related to the prevailed onset of the exponential growth. To determine the lethal nanoparticle dosage, the concentration range in which a minimum of $B(t)$ develops and disappears should be found analytically. We found that the minimum disappears for $v \geq 0.345$ treatments for which the bacterial population decreases continually. This value is in excellent agreement with the experimentally-obtained MBC concentration.

According to the model, the decrease of bacterial concentration is due to the uptake of the AgNPs, which causes bacterial death. In this process, the nanoparticles are removed from the habitat. This is in line with the study done by Sondi and Salopek Sondi [8] where TEM analysis clearly showed that the nanoparticles were accumulated in the membrane, while some of them successfully penetrated into the cells. When the concentration of the NPs falls below a certain level, the rest of the viable bacteria start to divide.

5. Data Analysis and Discussion

There is a wide range of reported MICs of silver nanoparticles, typically between 1 and 100 $\mu\text{g}/\text{mL}$ [3,9,39,58,59]. Since the bactericidal effect depends on nanoparticles' physical and chemical properties, the bacterial strain and growth conditions, it is reasonable to conclude that the obtained MIC value of $73 \pm 11 \mu\text{g}/\text{mL}$ falls within the reported range.

To compare the model with the experimental data from Figure 2a,b, the contributions of nutrients, nanoparticles, and cells to the measured OD data should be taken into account. We neglect the contribution of nutrients in accord to our previous findings [40], where the change in nutrients concentration did not provide observable change in the initial OD signal for the nutrients concentrations described here. The total OD signal can then be written as the sum of the constant contribution of the well plate and the medium c_m and the time and volume-share dependent contributions of bacterial $c_b B(t, v)$ and nanoparticles $c_p P(t, v)$ concentrations:

$$OD(t, v) = c_m + c_b \cdot B(t, v) + c_p \cdot P(t, v) \quad (8)$$

The contribution of AgNPs is in accordance with Figure 1a that shows absorbance of the silver nanoparticles at 595 nm, the wavelength used in our OD experiments.

The constants c_b and c_p reflect the light scattering/absorbance intensity for the bacteria and for the nanoparticles, respectively. To compare the experimental and theoretical growth curves, these constants are determined. The constants are obtained from the two limiting cases: the beginning of the growth, where $B(0, v) \approx 0$, and from the maximum of the population, where $P(t, v) \approx 0$.

The contribution of the NPs to the total OD signal is observed at the beginning of the growth, while the bacterial concentration is very low and not visible in the OD signal, so the condition $B(0, v) = 0$ in Equation (8) is fulfilled and we assume that the whole change in the OD signal is due to the change of the NPs concentration. The contribution of the AgNPs to the OD signal is obtained from the

concentration dependence of the initial OD($0, v$) obtained for different growth curves. These data are shown in Figure 6. The line is the linear fit to the data given by the expression:

$$OD(0, v) = (0.086 + 0.074 \cdot v) \text{ a.u.} \quad (9)$$

where the intercept $c_m = 0.086$ a.u. is the absorbance of the well plate and the medium. The coefficient $c_p = 0.074$ a.u. is obtained from the slope of the linear fit. We see that maximal overall contribution of AgNPs to the total OD is of the order of 0.02 a.u. and is much less than the maximum bacteria OD, which is around 0.5 a.u.

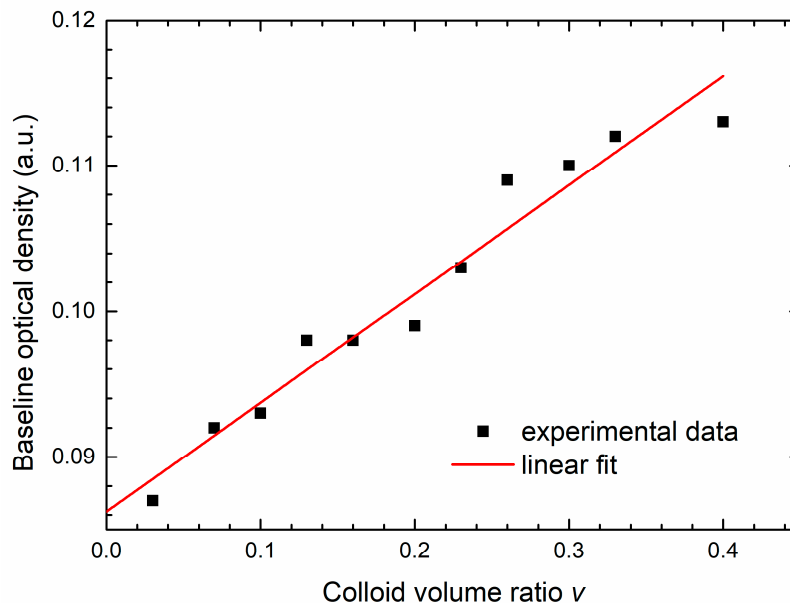


Figure 6. Initial OD (baseline) of the experimental growth curves given in Figure 2a, as a function of the colloid volume share v , is given by squares. Linear fit obtained for these data, given by the straight line, is the contribution of the silver nanoparticles to the total OD.

Since NPs are taken up by the bacterial cells, the concentration of the nanoparticles decreases so from the exponential phase and onwards it becomes negligible, in comparison to the bacterial concentration, so we can put $P(t, v) = 0$. Equation (8) becomes:

$$OD(t, v) = c_m + c_b \cdot B(t, v) \quad (10)$$

and we can compare the OD data with the calculated bacterial concentration.

Equation (10) shows that if we subtract c_m from the experimental $OD(t, v)$ data and set c_b to 1, there is one-to-one correspondence between the theoretical calculations and experimental data. In other words, the calculated, theoretical data, are expressed in a.u. Note that the theoretical concentrations of nutrients and nanoparticles are calculated in terms of bacterial equivalents, as explained before, and are also given in a.u.

When modelling the experimental curves in Figure 7a, we found that the best fits are obtained for the initial nanoparticles concentration $P(0, v) = 0.05 \times v$ a.u.. Substituting this expression for v in Equation (9) gives:

$$OD_{th}(0, v) = 0.086 \text{ a.u.} + 1.5 \cdot P(0, v). \quad (11)$$

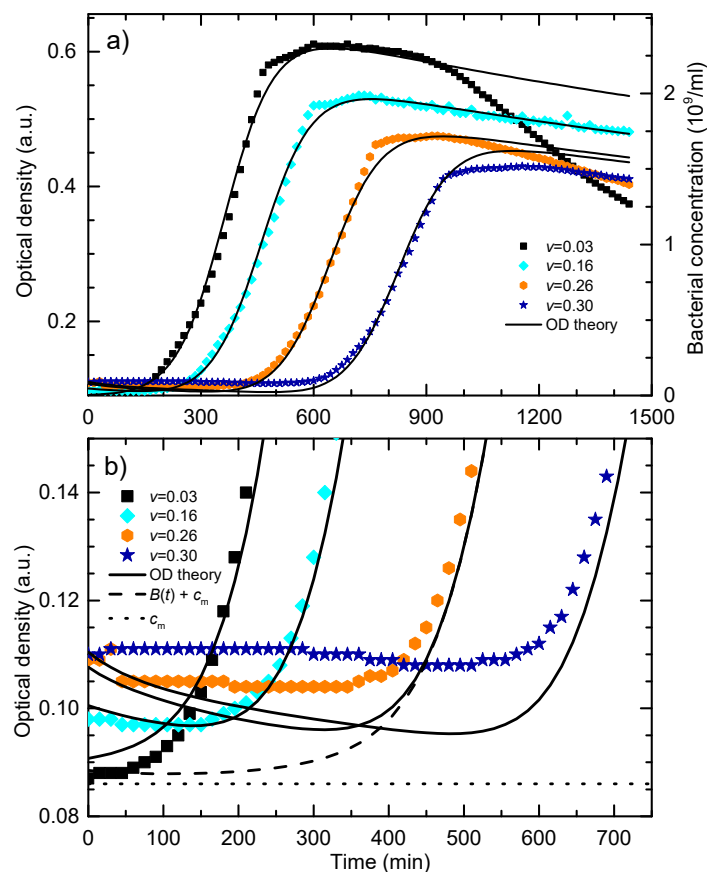


Figure 7. (a) Comparison of the experimental curves (symbols) with theoretical fits for different v values (lines). (b) the first 700 min of the OD signal from Figure 7a. The symbols are the raw experimental data for the different colloid volume shares and the full lines are the theoretical fits as given by Equations (1)–(3) and Equation (12). The dashed line is the theoretical bacterial concentration $B(t)$ for $v = 0.26$ summed with the constant $c_m = 0.086$. The dotted line is $c_m = 0.086$ a.u., i.e., the optical density of the well plate and the master medium.

Equation (11) gives calculated initial OD for different growth curves as a function of the initial colloid volume share v , i.e., concentration of nanoparticles. It reveals that one “package” of the AgNPs needed to annihilate a single bacterium contributes 1.5 times more to the total OD when compared to the OD contribution of a single bacterium. This dependence is used to describe time evolution of the OD for a growth curve for which the nanoparticles concentration is time-dependent.

As a result, Equation (8) assumes the form:

$$OD_{th}(t) = 0.086 \text{ a.u.} + B(t) + 1.5 \cdot P(t). \quad (12)$$

This allows us to model the obtained experimental OD data with more accuracy. To compare the experimental and theoretical data, the parameters were adjusted and the solutions of Equations (1)–(3) were calculated in bacteria-concentration equivalent absorbance units. In accordance with the Equation (12) the calculated nanoparticles concentration is multiplied by the factor of 1.5. The comparison of the experimental and theoretical OD response of bacteria and nanoparticles for the four representative experimental growth curves from Figure 2a is given in Figure 7a. The symbols are the experimental data while the lines are the theoretical fits according to the solutions of the Equations (1)–(3) and OD contributions given by Equation (12).

The fitting procedure was the following. Firstly, the growth curve for the colloid volume share $v = 0.16$ was fitted in a way that only parameter $v = 0.16$ was fixed and all other parameters in the system of Equations (1)–(3) were varied. This curve was chosen merely because it is in the middle of

the treatment range. Initially, to obtain P_M , the contribution of nanoparticles in the OD signal was neglected, but for further iterations Equation (12) was used to compare the fit with the experimental data. The least-square fit was obtained for the following parameters set: $B_0 = 0.0025$, $P_M = 0.05$, $N_M = 0.57$, $\gamma = 1.65$. When fitting the other curves, only the parameter v was changed while all other model parameters were kept at the same values as for the $v = 0.16$ sample.

It can be seen that the theoretical curves fit the experimental data for the lag and the exponential phase very well, i.e., the model completely describes the nanoparticles concentration-dependent postponed bacterial growth. The obtained correlation coefficients for the corresponding sets of data are: 0.96 for $v = 0.03$ curves, 0.99 for $v = 0.16$ curves, 0.99 for $v = 0.26$ curves, and 0.99 for $v = 0.30$ curves.

The postponed bacterial growth for cultures treated with AgNPs is found in many published data [9,10,38,39,60]. Our model, however, less successfully describes the reduction of the maximal OD for higher nanoparticles concentration, as well as the time-dependent decrease of the bacterial population in the death phase. Lowering of the maximal OD is reported in many studies [9–11,38] while some report relatively unaffected max OD value for treatments with spherical silver nanoparticles [39,61]. In our case, the decrease of the maximal OD is mostly related to the experimental design. Notably, the maximal bacterial population depends on the initial concentration of nutrients [40]. In the experiment, the NPs concentration is changed by replacing the growth medium with the produced colloid. Consequently, the samples with the higher AgNPs concentration had lower initial concentration of nutrients and thus developed lower maximal number of bacterial cells.

It is also noticeable that for higher AgNP concentrations, the experimental maximal OD is systematically lower than the calculated value. The drop down of the maximal OD could be due to the return of AgNPs back to the habitat, caused by the decomposition of the dead cells. In other words, it is reasonable to presume that a dead bacterium decomposes and releases the nanoparticles back into the batch so that some nanoparticles might be used more than once. However, these considerations demand further investigation and modeling of the system.

The data also show that the AgNPs treatment does not change the bacterial growth rate. A weak growth rate reduction can be attributed to the change in nutrients concentration as we found for untreated cells [40]. Published data show a discrepancy regarding this issue: some report relatively unaffected growth rates [39,60] while others report growth rate reductions [11,38]. To resume, we found that the change in the observed maximum OD and the growth rate is due to the change in the initial nutrients concentration and not due to the influence of the AgNPs.

Figure 7b presents details of the data from Figure 7a at the beginning of the growth. The symbols are the raw experimental data and the full lines are the theoretical fits for the different colloid volume shares, as given by Equations (1)–(3) and Equation (12). At this scale, all the contributions to the optical density signal can be resolved. This is demonstrated for the sample with the colloid volume share $v = 0.26$. The dotted line is the constant $c_m = 0.086$ a.u., i.e., the OD of the well plate and the master medium. The difference between the dashed and dotted line is the theoretical bacterial contribution $B(t)$ and the difference between the dashed and the full line is the theoretical contribution of the nanoparticles $P(t)$. As can be seen in the figure, for $t > 500$ min this difference is practically zero because $P(t)$ falls to zero. When $B(t)$ and $P(t)$ curves are compared, it is noticeable that the prominent decrease in the OD value, before the bacterial concentration OD signal prevails, can only be attributed to the reduction of the nanoparticle concentration in the habitat due to the bacterial uptake. From Figure 7b, we also see to what extent the theoretical model can describe the experimental data. Generally, it can be noted that the agreement with the experiment is better for lower nanoparticles concentrations, $v = 0.03$ and $v = 0.16$, then for the higher ones. For higher nanoparticle concentrations, theoretical curves exhibit a more pronounced minimum in the OD when compared to the experiment. This could be because the nanoparticles that were adhered to the bacterial surface still absorb some of the light and thus still contribute to the measured OD signal. However, the theoretical curves follow the trend of the OD decrease before bacterial growth prevails which is observed in the experimental data.

The theoretical calculations show that, at the beginning of the growth, the nanoparticles contribution to the OD dominates over the bacterial and that the decrease of the total OD, as seen in Figures 7b and 8, comes from the decrease of the nanoparticles concentration in the batch. It is reasonable to presume that this decrease is due to the uptake of the nanoparticles by the bacteria because the nanoparticles that enter the bacteria are no longer visible to the spectrophotometer. Our results are supported by the TEM data which clearly showed that the AgNPs have penetrated the membrane/cell [9].

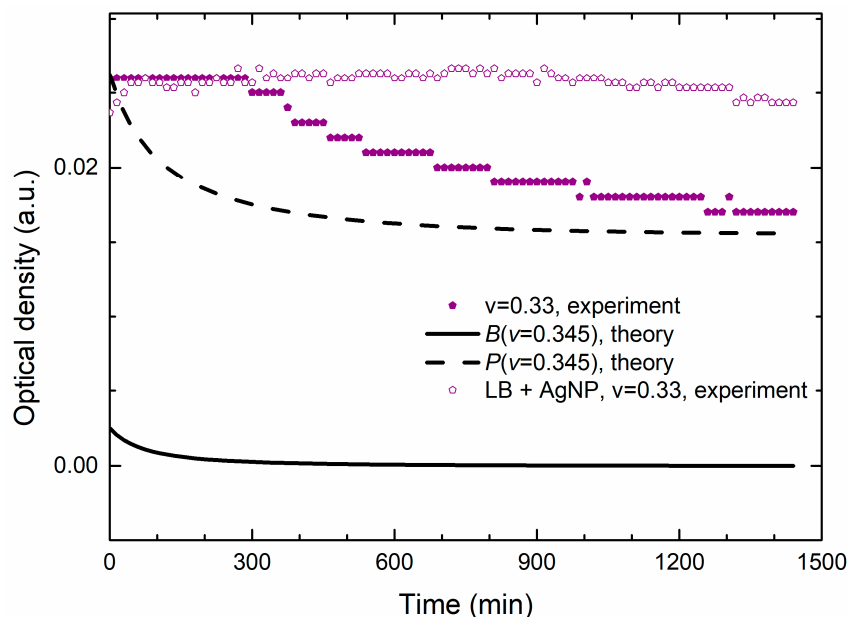


Figure 8. Growth curves of bacteria treated with the MBC concentration. The full symbols are the experimental OD data for bacterial $v = 0.33$ treatment (c_m value was subtracted), i.e., the AgNPs' OD signal. The full and the dashed lines are the theoretical data for bacterial and for nanoparticle concentrations, respectively, for $v = 0.345$. All the curves exhibit a continuous drop of OD for the given time frame. The open symbols are the experimental data obtained for $v = 0.33$ mixture of LB growth medium and AgNPs.

When modeling non-treated curves, we have shown [40] that the bacterial OD could not be observed at the initial time by the utilized spectrophotometer for the inoculum size used in these experiments. This indicates that the initial decrease of OD given in Figure 7b, cannot be attributed to the inactivation of the bacterial cells. When it comes to the MIC/MBC value, there is a small discrepancy between the experimental and theoretical data. From the experiment we found that the MIC/MBC value is at $v = 0.33$ and the theoretical model gives $v = 0.345$.

Figure 8 shows the experimental and theoretical growth data for the MIC/MBC concentration. We see that the theoretical OD data are lower than the measured OD, but they describe well the time dependence of the measured OD. Additionally, Figure 8 reveals that the nanoparticles contribution to the OD signal is approximately an order of magnitude greater than the contribution of bacteria. The bacterial concentration also exhibits a decrease but on the scale that is comparable with the sensitivity of the spectrophotometer (about 0.001 a.u.).

It is generally accepted that the silver ions (Ag^+) are, to some extent, released by AgNPs and there are opinions that these Ag^+ ions are mostly responsible for the antibacterial effect. According to the literature [62], silver ions are likely to interact with chloride ions (Cl^-) present in the bacterial growth medium and can cause precipitation of silver ions as $\text{AgCl}(s)$. Therefore, there is a possibility that the decrease in the OD signal found at the lethal concentration of AgNPs appears due to the AgNPs dissolution in the growth medium.

However, our experimental data obtained for the same non-inoculated sample, given by open symbols in Figure 8, exhibits almost constant OD which does not support the Ag^+ release mechanism as the main cause of the obtained decrease of the OD, which is expected to appear even without the cells. Since the OD decrease does not appear if there are no bacteria in the batch, we conclude that these data support the hypothesis of our model, according to which the OD decreases because of the bacterial uptake of the nanoparticles.

This supports our statement that, for the lethal treatment, the OD signal measures mostly the change in the concentration of the nanoparticles due to the bacterial uptake.

It should be emphasized that the lag phase was not observed in our experiments with the non-treated bacteria, which were prepared according to the same protocol [40] so the “traditional” lag is not included in the model. Figure 7b clearly shows that the postponed exponential growth is not due to the classical lag, i.e., the absence of the bacterial division, and should be considered as a dynamic lag phase. According to the model, Figure 4 shows that the nutrients consumption continues even when the bacterial concentration is being reduced. Thus, during this dynamic lag phase, bacteria are dividing and being inactivated by the AgNPs at the same time. The duration of the dynamic lag phase depends on the nanoparticles concentration. We find that the time interval measured from the beginning of the growth to the inflection point (the point at which the growth is maximal) is the most reliable measure for comparing the experimental and theoretical data. This time is easily determined from the maximum of the time derivative of the growth curve. We propose that this time should be called the dynamic lag time. The dynamic lag phase includes the bacterial division and inactivation.

The symbols in Figure 9 are the dynamic lag times obtained from the maximum of the derivative of the experimental OD curves from Figure 2a for different colloid volume shares v . The full line, obtained from the derivative of the theoretical curves, follows the experimental data very well. We see that the dynamical lag time increases with the nanoparticles concentration and diverges (becomes infinite) at the lethal colloid volume share $v = 0.345$. The limit between bacterial life and death conditions (lethal treatment) is denoted by the vertical line. In fact, Figure 9 represents a transition between life and death conditions, transforming the bacterial habitat from the one that enables bacterial growth to a habitat in which the bacteria growth is suppressed.

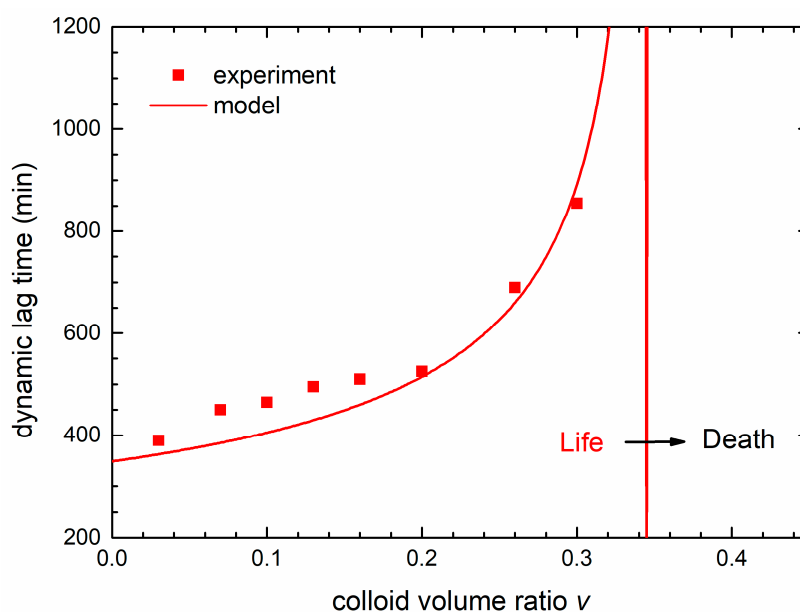


Figure 9. The dependence of the dynamic lag time on the colloid volume share v . The squares are the data obtained from the experimental growth curves and the solid line are the calculated data obtained from the theoretical model. The limit between bacterial life and death conditions (lethal treatment) is denoted by the vertical dashed line.

Since there are rare attempts on modeling the bacterial growth in the presence of nanomaterial in general, we find this model a good start for future developments. It is important to note that further validation of this model should be conducted for different bacterial strains growing under different conditions. The model might also be applicable if other antibacterial agents are utilized as long as they are detectable via spectrophotometer.

6. Conclusions

The main goal of this study is better understanding of bactericidal mode of action of silver nanoparticles. The silver nanoparticle colloid was synthesized by laser ablation in deionized water. To determine the NPs stability, composition, structure, size and concentration, UV-VIS, zeta potential, GIXRD, DLS, AFM, and TEM measurements were performed. The concentration of the AgNPs in the colloid was estimated from the volume of the ejected material. The colloid proved to be stable having spherical NPs with the average diameter of ~11.3 nm and the log-normal size distribution. The GIXRD results revealed the fcc-Ag crystallites and very weak presence of the silver oxide phase.

The colloid was tested against *E. coli* DH5 α cells which showed sensitivity towards the produced colloid. The AgNPs MIC/MBC values were 73 ± 11 $\mu\text{g/mL}$. Growth curves of bacteria treated with sub-MIC and MIC AgNP concentrations were obtained via the OD measurements.

The main effects of the treatment are the increase of the baseline of the growth curve, increase of the apparent lag time, and reduction of the maximal OD, without significant change of the growth rate. Growth curves of bacteria treated with higher sub-MIC concentrations exhibit a minimum, before the exponential growth prevails. For concentrations higher than the MIC, the growth is suppressed and the OD constantly decreases.

In order to analyze the data, we designed a novel growth model as an extension of the interaction-based model for the non-treated cells [40]. The main assumption of the model is that treated bacteria uptake the nanoparticles, which results in the decrease of the both the nanoparticles and the bacteria concentrations. The time change of the bacterial, nutrients, and nanoparticles concentrations depends on the strengths of the bacteria–nutrients, bacteria–bacteria, and bacteria–nanoparticles interactions.

We have shown that the experimental growth data reflect the concentration of both bacterial cells and nanoparticles. The contribution of the nanoparticles was clearly observed at the beginning of the growth, when the nanoparticles OD signal dominates the bacterial one. The signal was found to be constant for the non-inoculated sample and it decreased for the lethal bacterial treatment because AgNPs enter the bacteria. This also brings us to the conclusion that, for the lethal treatment, the decrease in OD mostly reflects the change in the nanoparticles concentration.

The model completely describes concentration-dependent postponed growth, with very good fits for the apparent lag and the exponential phase. It also describes the reduction of the maximal population with the colloid volume share increase and the decrease of the bacterial population in the death phase. According to the model, the postponed exponential growth is not due to a classic lag in which bacteria do not divide. This state can be characterized as a dynamic lag phase, or a near steady state for which the bacterial growth rate is close to the bacterial death rate. In the lag phase bacteria are dividing due to nutrients consumption, and being inactivated due to the uptake of the silver nanoparticles, at the same time. The duration of the dynamic lag time increases with the nanoparticles concentration and becomes infinite at the lethal concentration, representing a transition between bacterial life and death conditions.

To conclude, the main contributions of this research may be emphasized as follows. The observed lag phase induced by AgNPs is not postponed bacterial growth and the predominant mode of antibacterial action of AgNPs is their penetration inside the cell.

Author Contributions: L.K.: conceptualization, methodology, formal analysis, AFM, and bacterial growth/treatment investigation, writing—original draft, writing—review and editing, visualization. M.Š.: bacterial growth/treatment investigation. A.M.: bacterial growth/treatment investigation. P.U.: TEM investigation,

visualization. K.S.: GIXRD investigation, visualization. N.K.: investigation: nanoparticle production and organization of nanoparticle characterization, visualization. I.A.: conceptualization, methodology, formal analysis, writing—review and editing, writing—original draft, visualization, supervision. All authors have read and agreed to the published version of the manuscript.

Funding: L.K. and I.A. were partially supported by the Ministry of Science and Education of the Republic of Croatia, bilateral Croatia-USA agreement on the scientific and technological cooperation, Project No. 1/2014. N. K. was supported by project IP-11-2013-2753 funded by the Croatian Science Foundation.

Acknowledgments: The authors would like to thank V.Zlatić for helpful discussions.

Conflicts of Interest: The authors declare no conflict of interest.

References

1. Levy, S.B.; Marshall, B. Antibacterial resistance worldwide: Causes, challenges and responses. *Nat. Med.* **2004**, *10*, S122–S129. [[CrossRef](#)] [[PubMed](#)]
2. Rai, M.; Yadav, A.; Gade, A. Silver nanoparticles as a new generation of antimicrobials. *Biotechnol. Adv.* **2009**, *27*, 76–83. [[CrossRef](#)] [[PubMed](#)]
3. Morones, J.R.; Elechiguerra, J.L.; Camacho, A.; Holt, K.; Kouri, J.B.; Ramírez, J.T.; Yacaman, M.J. The bactericidal effect of silver nanoparticles. *Nanotechnology* **2005**, *16*, 2346–2353. [[CrossRef](#)] [[PubMed](#)]
4. Kim, J.S.; Kuk, E.; Yu, K.N.; Kim, J.-H.; Park, S.J.; Lee, H.J.; Kim, S.H.; Park, Y.K.; Park, Y.H.; Hwang, C.-Y.; et al. Antimicrobial effects of silver nanoparticles. *Nanomed. Nanotechnol. Biol. Med.* **2007**, *3*, 95–101. [[CrossRef](#)] [[PubMed](#)]
5. Schlemmer, W.; Fischer, W.; Zankel, A.; Vukušić, T.; Filipič, G.; Jurov, A.; Blažeka, D.; Goessler, W.; Bauer, W.; Spirk, S.; et al. Green Procedure to Manufacture Nanoparticle-Decorated Paper Substrates. *Materials* **2018**, *11*, 2412. [[CrossRef](#)] [[PubMed](#)]
6. Siddiqi, K.S.; Husen, A.; Rao, R.A.K. A review on biosynthesis of silver nanoparticles and their biocidal properties. *J. Nanobiotechnol.* **2018**, *16*, 14. [[CrossRef](#)]
7. Hajipour, M.J.; Fromm, K.M.; Akbar Ashkarran, A.; Jimenez de Aberasturi, D.; de Larramendi, I.R.; Rojo, T.; Serpooshan, V.; Parak, W.J.; Mahmoudi, M. Antibacterial properties of nanoparticles. *Trends Biotechnol.* **2012**, *30*, 499–511. [[CrossRef](#)]
8. Ivask, A.; ElBadawy, A.; Kaweeterawat, C.; Boren, D.; Fischer, H.; Ji, Z.; Chang, C.H.; Liu, R.; Tolaymat, T.; Telesca, D.; et al. Toxicity Mechanisms in Escherichia coli Vary for Silver Nanoparticles and Differ from Ionic Silver. *ACS Nano* **2014**, *8*, 374–386. [[CrossRef](#)]
9. Sondi, I.; Salopek-Sondi, B. Silver nanoparticles as antimicrobial agent: A case study on E. coli as a model for Gram-negative bacteria. *J. Colloid Interface Sci.* **2004**, *275*, 177–182. [[CrossRef](#)]
10. Ruparella, J.P.; Chatterjee, A.K.; Duttagupta, S.P.; Mukherji, S. Strain specificity in antimicrobial activity of silver and copper nanoparticles. *Acta Biomater.* **2008**, *4*, 707–716. [[CrossRef](#)]
11. Shrivastava, S.; Bera, T.; Roy, A.; Singh, G.; Ramachandrarao, P.; Dash, D. Characterization of enhanced antibacterial effects of novel silver nanoparticles. *Nanotechnology* **2007**, *18*, 225103. [[CrossRef](#)]
12. Masri, A.; Anwar, A.; Ahmed, D.; Siddiqui, R.B.; Shah, M.R.; Khan, N.A. Silver nanoparticle conjugation-enhanced antibacterial efficacy of clinically approved drugs cephadrine and vildagliptin. *Antibiotics* **2018**, *7*, 100. [[CrossRef](#)] [[PubMed](#)]
13. Panáček, A.; Smékalová, M.; Kilianová, M.; Pucek, R.; Bogdanová, K.; Věčřová, R.; Kolár, M.; Havrdová, M.; Płaza, G.A.; Chojniak, J.; et al. Strong and nonspecific synergistic antibacterial efficiency of antibiotics combined with silver nanoparticles at very low concentrations showing no cytotoxic effect. *Molecules* **2016**, *21*, 26. [[CrossRef](#)] [[PubMed](#)]
14. Zorraqu, I.; Cueva, C.; Bartolom, B.; Moreno-arribas, M.V. Silver Nanoparticles against Foodborne Bacteria. Effects at Intestinal Level and Health Limitations. *Microorganisms* **2020**, *8*, 132. [[CrossRef](#)] [[PubMed](#)]
15. Nedyalkova, M.; Dimitrov, D.; Donkova, B.; Simeonov, V. Chemometric Evaluation of the Link between Acute Toxicity, Health Issues and Physicochemical Properties of Silver Nanoparticles. *Symmetry* **2019**, *11*, 1159. [[CrossRef](#)]
16. Zafar, N.; Shamaila, S.; Nazir, J.; Sharif, R.; Shahid Rafique, M.; Ul-Hasan, J.; Ammara, S.; Khalid, H. Antibacterial Action of Chemically Synthesized and Laser Generated Silver Nanoparticles against Human Pathogenic Bacteria. *J. Mater. Sci. Technol.* **2016**, *32*, 721–728. [[CrossRef](#)]

17. Korshed, P.; Li, L.; Liu, Z.; Wang, T. The Molecular Mechanisms of the Antibacterial Effect of Picosecond Laser Generated Silver Nanoparticles and Their Toxicity to Human Cells. *PLoS ONE* **2016**, *11*, e0160078. [[CrossRef](#)]
18. Pandey, J.K.; Swarnkar, R.K.; Soumya, K.K.; Dwivedi, P.; Singh, M.K.; Sundaram, S.; Gopal, R. Silver Nanoparticles Synthesized by Pulsed Laser Ablation: As a Potent Antibacterial Agent for Human Enteropathogenic Gram-Positive and Gram-Negative Bacterial Strains. *Appl. Biochem. Biotechnol.* **2014**, *174*, 1021–1031. [[CrossRef](#)]
19. Perito, B.; Giorgetti, E.; Marsili, P.; Muniz-Miranda, M. Antibacterial activity of silver nanoparticles obtained by pulsed laser ablation in pure water and in chloride solution. *Beilstein J. Nanotechnol.* **2016**, *7*, 465–473. [[CrossRef](#)]
20. Besner, S.; Kabashin, A.V.; Winnik, F.M.; Meunier, M. Ultrafast laser based “green” synthesis of non-toxic nanoparticles in aqueous solutions. *Appl. Phys. A* **2008**, *93*, 955–959. [[CrossRef](#)]
21. Vamanu, E.; Ene, M.; Biță, B.; Ionescu, C.; Crăciun, L.; Sârbu, I. In vitro human microbiota response to exposure to silver nanoparticles biosynthesized with mushroom extract. *Nutrients* **2018**, *10*, 607. [[CrossRef](#)] [[PubMed](#)]
22. Amendola, V.; Meneghetti, M. Laser ablation synthesis in solution and size manipulation of noble metal nanoparticles. *Phys. Chem. Chem. Phys.* **2009**, *11*, 3805. [[CrossRef](#)] [[PubMed](#)]
23. Farrokhi, Z.; Ayati, A.; Kanvisi, M.; Sillanpää, M. Recent advance in antibacterial activity of nanoparticles contained polyurethane. *J. Appl. Polym. Sci.* **2019**, *136*, 1–13. [[CrossRef](#)]
24. Lugarà, P.; Volpe, A.; Sportelli, M.; Ancona, A.; Picca, R.; Palazzo, G.; Clemente, M.; Cioffi, N.; Izzi, M. The Pros and Cons of the Use of Laser Ablation Synthesis for the Production of Silver Nano-Antimicrobials. *Antibiotics* **2018**, *7*, 67.
25. Durán, N.; Durán, M.; de Jesus, M.B.; Seabra, A.B.; Fávaro, W.J.; Nakazato, G. Silver nanoparticles: A new view on mechanistic aspects on antimicrobial activity. *Nanomed. Nanotechnol. Biol. Med.* **2016**, *12*, 789–799. [[CrossRef](#)]
26. Peleg, M.; Corradini, M.G. Microbial Growth Curves: What the Models Tell Us and What They Cannot. *Crit. Rev. Food Sci. Nutr.* **2011**, *51*, 917–945. [[CrossRef](#)]
27. Baty, F.; Delignette-Muller, M.-L. Estimating the bacterial lag time: Which model, which precision? *Int. J. Food Microbiol.* **2004**, *91*, 261–277. [[CrossRef](#)]
28. Swinnen, I.A.M.; Bernaerts, K.; Dens, E.J.J.; Geeraerd, A.H.; Van Impe, J.F. Predictive modelling of the microbial lag phase: A review. *Int. J. Food Microbiol.* **2004**, *94*, 137–159. [[CrossRef](#)]
29. Baranyi, J. Comparison of Stochastic and Deterministic Concepts of Bacterial Lag. *J. Theor. Biol.* **1998**, *192*, 403–408. [[CrossRef](#)]
30. Drummond, L.J. Effects of sub-MIC concentrations of antibiotics on growth of and toxin production by *Clostridium difficile*. *J. Med. Microbiol.* **2003**, *52*, 1033–1038. [[CrossRef](#)]
31. Cummins, J.; Reen, F.J.; Baysse, C.; Mooij, M.J.; O’Gara, F. Subinhibitory concentrations of the cationic antimicrobial peptide colistin induce the pseudomonas quinolone signal in *Pseudomonas aeruginosa*. *Microbiology* **2009**, *155*, 2826–2837. [[CrossRef](#)]
32. Theophel, K.; Schacht, V.J.; Schlüter, M.; Schnell, S.; Stingu, C.S.; Schaumann, R.; Bunge, M. The importance of growth kinetic analysis in determining bacterial susceptibility against antibiotics and silver nanoparticles. *Front. Microbiol.* **2014**, *5*, 1–10. [[CrossRef](#)] [[PubMed](#)]
33. Gomez Escalada, M.; Russell, A.D.; Maillard, J.Y.; Ochs, D. Triclosan-bacteria interactions: Single or multiple target sites? *Letts. Appl. Microbiol.* **2005**, *41*, 476–481. [[CrossRef](#)]
34. Li, W.-R.; Sun, T.-L.; Zhou, S.-L.; Ma, Y.-K.; Shi, Q.-S.; Xie, X.-B.; Huang, X.-M. A comparative analysis of antibacterial activity, dynamics, and effects of silver ions and silver nanoparticles against four bacterial strains. *Int. Biodeterior. Biodegrad.* **2017**, *123*, 304–310. [[CrossRef](#)]
35. Ahmad, T.; Wani, I.A.; Manzoor, N.; Ahmed, J.; Asiri, A.M. Biosynthesis, structural characterization and antimicrobial activity of gold and silver nanoparticles. *Colloids Surfaces B Biointerfaces* **2013**, *107*, 227–234. [[CrossRef](#)] [[PubMed](#)]
36. Li, W.-R.; Xie, X.-B.; Shi, Q.-S.; Zeng, H.-Y.; OU-Yang, Y.-S.; Chen, Y.-B. Antibacterial activity and mechanism of silver nanoparticles on *Escherichia coli*. *Appl. Microbiol. Biotechnol.* **2010**, *85*, 1115–1122. [[CrossRef](#)] [[PubMed](#)]

37. Zwietering, M.H.; Jongenburger, I.; Rombouts, F.M.; Van, T.R.K.; Van't Riet, K. Modeling of the bacterial growth curve. *Appl. Environ. Microbiol.* **1990**, *56*, 1875–1881. [[CrossRef](#)]
38. Chatterjee, T.; Chatterjee, B.K.; Majumdar, D.; Chakrabarti, P. Antibacterial effect of silver nanoparticles and the modeling of bacterial growth kinetics using a modified Gompertz model. *Biochim. Biophys. Acta Gen. Subj.* **2015**, *1850*, 299–306. [[CrossRef](#)]
39. Haque, M.A.; Imamura, R.; Brown, G.A.; Krishnamurthi, V.R.; Niyonshuti, I.I.; Marcelle, T.; Mathurin, L.E.; Chen, J.; Wang, Y. An experiment-based model quantifying antimicrobial activity of silver nanoparticles on *Escherichia coli*. *RSC Adv.* **2017**, *7*, 56173–56182. [[CrossRef](#)]
40. Krce, L.; Šprung, M.; Maravić, A.; Aviani, I. A simple interaction-based *E. coli* growth model. *Phys. Biol.* **2019**, *16*, 066005. [[CrossRef](#)]
41. Krstulović, N.; Umek, P.; Salamon, K.; Capan, I. Synthesis of Al-doped ZnO nanoparticles by laser ablation of ZnO:Al₂O₃ target in water. *Mater. Res. Express* **2017**, *4*. [[CrossRef](#)]
42. Krstulović, N.; Shannon, S.; Stefanuik, R.; Fanara, C. Underwater-laser drilling of aluminum. *Int. J. Adv. Manuf. Technol.* **2013**, *69*, 1765–1773. [[CrossRef](#)]
43. Kostylev, M.; Otwell, A.E.; Richardson, R.E.; Suzuki, Y. Cloning should be simple: *Escherichia coli* DH5 α -mediated assembly of multiple DNA fragments with short end homologies. *PLoS ONE* **2015**, *10*, 1–15. [[CrossRef](#)] [[PubMed](#)]
44. Olmos, D.; Pontes-Quero, G.M.; Corral, A.; González-Gaitano, G.; González-Benito, J. Preparation and characterization of antimicrobial films based on LDPE/Ag nanoparticles with potential uses in food and health industries. *Nanomaterials* **2018**, *8*, 60. [[CrossRef](#)]
45. Segura González, E.A.; Olmos, D.; Lorente, M.Á.; Vélaz, I.; González-Benito, J. Preparation and characterization of polymer composite materials based on PLA/TiO₂ for antibacterial packaging. *Polymers* **2018**, *10*, 1365. [[CrossRef](#)]
46. Zammit, I.; Vaiano, V.; Ribeiro, A.R.; Silva, A.M.T.; Manaia, C.M.; Rizzo, L. Immobilised cerium-doped zinc oxide as a photocatalyst for the degradation of antibiotics and the inactivation of antibiotic-resistant bacteria. *Catalysts* **2019**, *9*, 222. [[CrossRef](#)]
47. Krüger, M.; Richter, P.; Strauch, S.M.; Nasir, A.; Burkovski, A.; Antunes, C.A.; Meißgeier, T.; Schlücker, E.; Schwab, S.; Lebert, M. What an *Escherichia coli* mutant can teach us about the antibacterial effect of chlorophyllin. *Microorganisms* **2019**, *7*, 59. [[CrossRef](#)]
48. Yuan, Q.; Bomma, M.; Xiao, Z. Enhanced Silver Nanoparticle Synthesis by *Escherichia Coli* Transformed with *Candida Albicans* Metallothionein Gene. *Materials* **2019**, *12*, 4180. [[CrossRef](#)]
49. CLSI. *Performance Standards for Antimicrobial Susceptibility Testing*, 26th ed.; CLSI Supplement M100S; Clinical Laboratory Standards Institute: Wayne, PA, USA, 2016.
50. Krstulović, N.; Milošević, S. Drilling enhancement by nanosecond–nanosecond collinear dual-pulse laser ablation of titanium in vacuum. *Appl. Surf. Sci.* **2010**, *256*, 4142–4148. [[CrossRef](#)]
51. Xia, Y.; Halas, N.J. Shape-Controlled Synthesis and Surface Plasmonic Properties of Metallic Nanostructures. *MRS Bull.* **2005**, *30*, 338–348. [[CrossRef](#)]
52. Agnihotri, S.; Mukherji, S.; Mukherji, S. Size-controlled silver nanoparticles synthesized over the range 5–100 nm using the same protocol and their antibacterial efficacy. *RSC Adv.* **2014**, *4*, 3974–3983. [[CrossRef](#)]
53. Müller, R.; Jacobs, C.; Kayser, O. Nanosuspensions as particulate drug formulations in therapy. *Adv. Drug Deliv. Rev.* **2001**, *47*, 3–19.
54. McCartney, M.L.; Olson, K.S.; Starostina, N.; Wong, C.; West, P.E. Tip dilation and AFM capabilities in the characterization of nanoparticles. *JOM* **2007**, *59*, 12–16.
55. Kiss, L.; Söderlund, J.; Niklasson, G.A.; Granqvist, C.G. New approach to the origin of lognormal size distributions of nanoparticles. *Nanotechnology* **1999**, *25*, 25–28. [[CrossRef](#)]
56. Söderlund, J.; Kiss, L.B.; Niklasson, G.A.; Granqvist, C.G. Lognormal Size Distributions in Particle Growth Processes without Coagulation. *Phys. Rev. Lett.* **1998**, *80*, 2386–2388. [[CrossRef](#)]
57. Krstulović, N.; Salamon, K.; Budimlija, O.; Kovač, J.; Dasović, J.; Umek, P.; Capan, I. Parameters optimization for synthesis of Al-doped ZnO nanoparticles by laser ablation in water. *Appl. Surf. Sci.* **2018**, *440*, 916–925. [[CrossRef](#)]
58. Martínez-Castañón, G.A.; Niño-Martínez, N.; Martínez-Gutierrez, F.; Martínez-Mendoza, J.R.; Ruiz, F. Synthesis and antibacterial activity of silver nanoparticles with different sizes. *J. Nanoparticle Res.* **2008**, *10*, 1343–1348. [[CrossRef](#)]

59. Dasgupta, N.; Ranjan, S.; Rajendran, B.; Manickam, V.; Ramalingam, C.; Avadhani, G.S.; Kumar, A. Thermal co-reduction approach to vary size of silver nanoparticle: Its microbial and cellular toxicology. *Environ. Sci. Pollut. Res.* **2016**, *23*, 4149–4163. [[CrossRef](#)]
60. Irwin, P.; Martin, J.; Nguyen, L.; He, Y.; Gehring, A.; Chen, C. Antimicrobial activity of spherical silver nanoparticles prepared using a biocompatible macromolecular capping agent: Evidence for induction of a greatly prolonged bacterial lag phase. *J. Nanobiotechnol.* **2010**, *8*, 34. [[CrossRef](#)]
61. Pal, S.; Tak, Y.K.; Song, J.M. Does the antibacterial activity of silver nanoparticles depend on the shape of the nanoparticle? A study of the gram-negative bacterium *Escherichia coli*. *J. Biol. Chem.* **2015**, *290*, 1712–1720. [[CrossRef](#)]
62. Franci, G.; Falanga, A.; Galdiero, S.; Palomba, L.; Rai, M.; Morelli, G.; Galdiero, M. Silver nanoparticles as potential antibacterial agents. *Molecules* **2015**, *20*, 8856–8874. [[CrossRef](#)] [[PubMed](#)]



© 2020 by the authors. Licensee MDPI, Basel, Switzerland. This article is an open access article distributed under the terms and conditions of the Creative Commons Attribution (CC BY) license (<http://creativecommons.org/licenses/by/4.0/>).

IV. PROBING THE MODE OF ANTIBACTERIAL ACTION OF SILVER NANOPARTICLES SYNTHESIZED BY LASER ABLATION IN WATER: WHAT FLUORESCENCE AND AFM DATA TELL US

Reproduced from:

Krce L, Šprung M, Rončević T, Maravić A, Čikeš Čulić V, Blažeka D, Krstulović N, Aviani I. Probing the Mode of Antibacterial Action of Silver Nanoparticles Synthesized by Laser Ablation in Water: What Fluorescence and AFM Data Tell Us. *Nanomaterials* 2020;10:1040. <https://doi.org/10.3390/nano10061040>.



Article

Probing the Mode of Antibacterial Action of Silver Nanoparticles Synthesized by Laser Ablation in Water: What Fluorescence and AFM Data Tell Us

Lucija Krce ^{1,*} , Matilda Šprung ² , Tomislav Rončević ³ , Ana Maravić ³ ,
Vedrana Čikeš Čulić ⁴ , Damjan Blažeka ⁵, Nikša Krstulović ⁵ and Ivica Aviani ¹

¹ Department of Physics, Faculty of Science, University of Split, Ruđera Boškovića 33, 21000 Split, Croatia; iaviani@pmfst.hr

² Department of Chemistry, Faculty of Science, University of Split, Ruđera Boškovića 33, 21000 Split, Croatia; msprung@pmfst.hr

³ Department of Biology, Faculty of Science, University of Split, Ruđera Boškovića 33, 21000 Split, Croatia; troncevic@pmfst.hr (T.R.); amaravic@pmfst.hr (A.M.)

⁴ Department of Medical Chemistry and Biochemistry, School of Medicine, University of Split, Šoltanska ulica 2, 21000 Split, Croatia; vedrana.cikes.culic@mefst.hr

⁵ Institute of Physics, Bijenička cesta 46, 10000 Zagreb, Croatia; dblazeka@ifs.hr (D.B.); niksak@ifs.hr (N.K.)

* Correspondence: lkrce@pmfst.hr

Received: 30 April 2020; Accepted: 27 May 2020; Published: 29 May 2020



Abstract: We aim to elucidate the mode of antibacterial action of the laser-synthesized silver colloid against *Escherichia coli*. Membrane integrity was studied by flow cytometry, while the strain viability of the treated culture was determined by plating. The spectrofluorometry was used to obtain the time development of the reactive oxygen species (ROS) inside the nanoparticle-treated bacterial cells. An integrated atomic force and bright-field/fluorescence microscopy system enabled the study of the cell morphology, Young modulus, viability, and integrity before and during the treatment. Upon lethal treatment, not all bacterial cells were shown to be permeabilized and have mostly kept their morphology with an indication of cell lysis. Young modulus of untreated cells was shown to be distinctly bimodal, with randomly distributed softer parts, while treated cells exhibited exponential softening of the stiffer parts in time. Silver nanoparticles and bacteria have shown a masking effect on the raw fluorescence signal through absorbance and scattering. The contribution of cellular ROS in the total fluorescence signal was resolved and it was proven that the ROS level inside the lethally treated cells is not significant. It was found that the laser-synthesized silver nanoparticles mode of antibacterial action includes reduction of the cell's Young modulus in time and subsequently the cell leakage.

Keywords: laser-synthesized nanoparticles; silver nanoparticles; mode of antibacterial action; nano-bio interactions; reactive oxygen species; atomic force microscopy; Young modulus

1. Introduction

Silver nanoparticles (AgNPs) have retained the interest of the scientific community, mostly due to their outstanding antibacterial property. They have been proven to have a synergistic effect on the antibacterial potential of antibiotics [1,2] and are increasingly being used for antimicrobial coating [3]. These promising results emphasize the need for thorough characterization of the used AgNPs and understanding of their antibacterial mode of action.

As suggested in the recent review paper [4], there are two main hypotheses for their antibacterial mode of action. The first hypothesis relies on the nanoparticle's electrostatic interaction with the

bacterium membrane and/or with membrane proteins which leads to membrane's partial dissolution. The second hypothesis presumes penetration of the AgNPs inside the cell/membrane and subsequent release of silver ions, followed by the increase of the reactive oxygen species (ROS) and cell oxidative stress. The two scenarios do not need to be mutually exclusive [4]. Ivask et al. [5] emphasize the role of the dissolved silver ions in the toxicity mechanism, and also the importance of AgNPs' physicochemical surface properties which govern the interaction with the bacterial cells. For coated silver nanoparticles, antimicrobial effects were found to be the interplay of nanoparticle (NP) size, solubility, and surface coating [6]. The activity of transition metals, such as silver, should also be considered to be the possible reason for potent antibacterial activity. Transition metals have an affinity to associate with R-SH groups, which can disrupt the function of specific enzymes or disrupt S-S bridges necessary to maintain the integrity of folded proteins, causing detrimental effects to the metabolism and the physiology of the cell [7]. Particle-specific antibacterial potential, which is manifested through increased intracellular concentration of Ag ions, has been previously reported as the AgNPs' main mechanism to battle bacteria [8]. Xiu et al. [9] report that the antimicrobial activity of AgNPs is solely due to the release of Ag ions. Notably, Durán et al. [10] state that the AgNPs exhibit their antibacterial activity through the cell's membrane disruption and DNA transformation via ROS but that there is a lack of data regarding the temporal resolution of the ROS production or possible membrane alterations induced by the AgNPs. Taken together, it is reasonable to say that the AgNPs adhesion to and/or penetration inside the cells, ROS generation and modulation of microbial signal transduction pathways are recognized as the most notable modes of antimicrobial action [11].

In comparison, AuNPs [12] and AuPtNPs [13] do not induce the generation of ROS. On the other hand, the antibacterial mechanism of copper-bearing titanium alloys includes an increased amount of ROS, among other cells' alterations [14]. The toxicity of graphene oxide towards bacteria may be attributed to both membrane and oxidative stress [15], while ZnO NPs induce ROS production and TiO₂ NPs promote changes in the outer membrane proteins [16].

Most of the reports concerning the antibacterial effect of the AgNPs refer to colloids produced by the reduction of metal salts with a chemical agent which results in colloids containing unwanted chemical byproducts. There are eco-friendly alternatives such as biosynthesis with bacteria, fungi, or plant-related parts [17]. However, one of the most convenient techniques is the physical production of colloids by using laser ablation in liquids (LAL) [18]. This method enables the production of pure colloids without byproducts and with unique surface properties [19] which is extremely important when one is trying to elucidate their mode of antibacterial action.

Microscopy techniques are rather useful since they can reveal membrane alteration caused by the AgNPs treatment. Previously, electron-microscopy data have revealed gaps in the cells' membrane and disorganization of entire cells [20], nanoparticles accumulated in the membrane, penetration into the cells and leaking of intracellular substances [21], nanoparticles found on cells' surface and attached to the substance released by the cells [22]. Transmission electron-microscopy images of *Escherichia coli* (*E. coli*) treated with LAL-produced AgNPs revealed that the nanoparticles have penetrated the cells' membranes and entered the cells while the cells had irregular appearance [23]. However, this technique does not enable the inspection of cells in their native environment.

Atomic force microscopy (AFM), enables the study of morphology and nanomechanical properties of live bacteria in different media. The loss of cellular morphology of AgNP-treated *Staphylococcus aureus* [24] and alterations in the bacterial cell surface [25] is reported for AFM performed on dried out bacterial cells. A rare report on AFM performed on hydrated AgNP-treated *E. coli* cells reveals membrane rupture, cell stiffness reduction, and appearance of cellular debris around the cells [26]. Although being a very convenient technique, AFM is still under-used in the study of AgNP-treated bacteria and according to our knowledge, there is no time-resolved analysis of Young modulus (YM) of the AgNP-treated bacterial cells.

AgNPs and Ag ions might act as catalysts and increase the generation of ROS which can lead to oxidative stress [19]. ROS detection is mostly performed using the 2',7'-dichlorodihydrofluorescein

(DCFH₂) which oxidizes inside the cells to yield the highly fluorescent 2',7'-dichlorofluorescein (DCF) [27]. The intensity of the fluorescence signal is proportional to the amount of ROS [28]. The research data obtained from previous reports suggest that: treatment with AgNPs alone did not induce significant ROS formation [29]; a significant increase in the DCF fluorescence intensity was observed for AgNP-treated bacterial cells [30]; colloidal silver significantly increased the production of ROS when compared with untreated cells [31]; ROS played a very important role in the antibacterial mechanism of AgNPs [32]. Interestingly, ROS detection data in AgNP-treated *E. coli* [33] showed that the fluorescence signal of AgNP-treated cells is lower than for the non-treated cells, for most treatment concentrations. ROS increase in bacterial cells, induced by biosynthesized AgNPs, was confirmed by DCFH₂ and antioxidant scavenging [34]. Treatment with the LAL-produced AgNPs resulted in the particle-size dependent ROS generation, highest for particles with an average size of 19 nm [35]. It is also worth noting that no significant difference in silver ion toxicity towards bacteria has been observed between anaerobic and aerobic conditions, which rules out oxidative stress by ROS as an important antibacterial mechanism for silver ions [36].

The AgNPs have been used in industry for food packaging, medical device coating, and environmental sensing [37]. LAL-synthesized AgNPs have already been used to fabricate AgNP-impregnated paper fines sheets with antimicrobial activity [38]. This type of AgNPs might also be used as drug carriers by applying different functionalization strategies [39]. Another application might include AgNP-impregnated polymeric nanofibers [40] for wound healing or the incorporation of AgNPs into a device for delivering bioactive agents, such as protein scaffolds [41]. These possible applications require careful consideration of AgNPs' biological activity and potential toxicity as well as careful quality, efficacy, and safety evaluation of final AgNP-enabled materials complying with the Safe-by-Design approach [3]. It must be noted that there is a justified global concern regarding the toxicity of AgNPs [42] and engineered nanomaterial in general [43,44].

Altogether, despite the numerous studies, there are still contrary reports on the mode of antibacterial action of colloidal silver. This could be partially related to the difference in the AgNPs colloid properties which depend on the synthesis method. Recently, based on modeling of the growth of AgNP-treated bacteria, we have shown that the antibacterial action of LAL-synthesized AgNPs is closely related to their penetration into the cell [45] which should be supported by other complementary experimental methods found in the literature. All the above encouraged us to extend our research of bactericidal effects induced by LAL-synthesized AgNPs, produced in our lab.

Most of our findings are done by studying the time development of the DCF fluorescence signal, which is proportional to the ROS level, and time-dependent YM spectroscopy of bacterial cells. This paper is aimed to contribute to the understanding of the mode of antibacterial action of AgNPs against *E. coli* as a model organism and to discuss some of the findings given in the literature in the context of our results.

2. Materials and Methods

The laser synthesis of AgNPs in water and thorough characterization of the produced colloid is described in [45]. The nanoparticles were determined to be spherical-like with the mean diameter of 13.1 nm (obtained from the transmission electron microscopy (TEM) measurements). The produced colloid was stable with the zeta potential of $\xi = -(53.1 \pm 1.1)$ mV and the obtained UV-Vis maximum at 404 nm. The mass concentration of AgNPs in the produced colloid was calculated to be of 220 ± 32 $\mu\text{g/mL}$. The MIC = MBC value is reported as a volume share v of the colloid in the batch culture and was obtained to be $v = (30 \pm 4)\%$. The colloid volume share v correlates to the mass concentration of AgNPs in the batch when it is multiplied by the mass concentration of the produced colloid. Therefore, in further text the colloid volume share v will be referred to as the AgNPs' concentration.

The *E. coli* DH5 α cells, used in this study for all experiments, were grown in the nutritionally impoverished Luria Bertani (LB) medium (5.0 g of tryptone, 2.5 g of yeast extract and 5.0 g of NaCl per 1 L of deionized sterile water). Overnight bacterial culture, grown at 37 °C and 220 rpm, was diluted

for at least 15 times in the fresh medium. Cells were further grown for 1.5 h in the same conditions. The minimal inhibitory concentration (MIC) and the minimal bactericidal concentration (MBC) of the produced colloid were determined as previously reported [45]. These experiments were repeated for each colloid production and are reported in terms of volume shares v of the colloid in the batch culture.

2.1. Time-Killing Assay

The assay was performed as explained in Blažević et al. [46]. Exponentially grown bacterial cells were adjusted spectrophotometrically to a density of 10^6 CFU/mL and exposed to $\frac{1}{2}$ MIC, MIC, and 2MIC values of the produced colloid. The strain viability was determined by plating the serial dilutions after the incubation at 37 °C for 0, 15, 30, 60, 90, 240, 360, and 600 min. Colonies were grown on Mueller Hinton agar (MHA) plates and were counted after 24 h. All measurements were done in duplicates and the reported values are their average.

2.2. Membrane Integrity Assay

The effect of the AgNPs on the bacterial inner membrane integrity was studied by measuring the percentage of propidium iodide (PI) positive cells after exposure to nanoparticles, using an Accuri C6 flow cytometer (BD Biosciences, San Jose, CA, USA). Cells penetrated by this stain are often referred to as the PI-positive cells (PI+). Cell staining was done as described previously in Rončević et al. [47]. The cells were treated by AgNPs in concentrations corresponding to $\frac{1}{2}$ MIC, MIC, and 2MIC, and the measurements were obtained after 0, 15, 30, 60, and 90 min of the treatment. Melittin, a strong membranolytic peptide [48], was used as a positive control, while stained untreated cells were used as the negative control. Non-stained cells and single stained samples were used to compensate fluorescence channels on the cytometer and to adjust appropriate gates on dot-plots. All measurements were done in triplicates, and for each incubation time at least 10,000 cells were collected. Data analysis was carried out with FlowLogic 6.0 software.

2.3. Reactive Oxygen Species (ROS) Detection

The obtained bacterial culture was centrifuged at $4500\times g$ for 5 min at room temperature. Pelleted cells were then resuspended (1:10) in the 1x phosphate-buffered saline (PBS) and the colloid AgNPs were added to the culture in several volume shares v : 0.01, 0.05, 0.10, 0.20, 0.25 and 0.30. The fluorimetric probe 2',7'-dichlorodihydrofluorescein diacetate (DCFH₂-DA) (Sigma-Aldrich, St. Louis, MO, USA) was diluted in dimethyl sulfoxide (DMSO) to the final concentration of 1 mg/mL and 2 μ L of diluted dye was added to the vials while the final volume of the reaction mix was 1 mL. After adding the AgNPs, samples were incubated for 30 min with shaking at 37 °C in the dark. The 0.33 mM H₂O₂ bacterial treatment was used as a positive control. Finally, 200 μ L of the reaction mix was transferred to the microtiter plate (Porvair Science, Wrexham, UK) and the fluorescence signal was obtained every 3 min using the spectrofluorometer (LS 55, Perkin Elmer, Waltham, MA, USA) at the 492 nm excitation and 523 nm emission wavelengths.

To measure the time dependence of the fluorescence signal without the cells, another set of samples was prepared in the same way while cell suspension was replaced by PBS. Also, two control data sets were obtained for the stained non-treated culture suspension and the stained PBS samples. All experiments were done in quadruplicates and the reported values are their averages.

2.4. AFM Measurements

A 50 μ L aliquot of the prepared culture was applied to the sterile Petri dishes (WPI, Sarasota, FL, USA) coated with the Cell-Tak (Corning, New York, NY, USA) solution prepared as we have previously reported [49]. To eliminate non-attached and loosely attached bacterial cells, the culture was thoroughly rinsed with the sterile medium 10 min after the application. This was done taking care not to dry out the sample during rising.

AFM measurements were carried out using a Nanowizard IV system (JPK/Bruker, Berlin, Germany) operating in the quantitative imaging (QI) mode (force-distance curve-based mode) using the pre-calibrated PFQNM-LC-A-CAL probes (Bruker, Billerica, MA, USA). The setpoint was kept at 1.2 nN while the extend/retract speed was up to 150 $\mu\text{m/s}$. Each measurement was done with a resolution of 128×128 pixels and with 10 μm scan sizes. Several AFM measurements were obtained before the treatment to make sure that the AFM probing does not influence the bacterial viability. The rinsing of the sample with the fresh medium followed this step. AFM probing was then done for cells treated with AgNPs at the concentration corresponding to 2MIC at several time points. All AFM measurements were done in the growth medium at 37 °C. The AFM data processing was carried out by the JPK data processing software. This software allows batch processing of the obtained force-distance curves. The processing was done to obtain the YM of the treated and non-treated bacterial cells for several time points. The YM was calculated by applying the Hertz model to the first 50 nm of the indentation made by the spherical indenter that has an end radius of 65 nm. The distribution of the bacterial YM was obtained from modulus data points whose corresponding height data were in the 5% of the highest points for each scan line. The baseline was taken to be the highest point belonging to the substrate.

2.5. Fluorescence and Bright-Field Microscopy

The used AFM system is integrated with the inverted optical fluorescence microscope IX73 (Olympus, Tokyo, Japan). The integration allows the overlay of the bright-field and the AFM image. Bright-field images were taken during the pre-treatment and treatment periods. Fluorescence images were obtained immediately after the final AFM measurements. The growth medium and the colloid mixture were replaced by the physiological saline solution and the cells were stained by the green-fluorescent nucleic stain SYTO 9 and the red-fluorescent nucleic PI (LIVE/DEAD BacLight Bacterial Viability Kit L7012; Invitrogen, Carlsbad, CA, USA). The staining was done by adding 1.5 μL of each dye per mL of the bacterial culture.

3. Results

Results of the time-killing assay are given in Figure 1a where cell count for bacteria treated with different concentrations of AgNPs and for non-treated bacteria are plotted in a logarithmic scale as a function of time. The inset shows the first 90 min of the experiment. The non-treated bacteria exhibit exponential growth, while the viable cells' data obtained for $v = 0.15$ treatment develop a broad minimum before the growth prevails. The viable cells data obtained for the MIC treatment show a continuous decrease until the complete population inactivation after 600 min of treatment. As expected, the 2MIC ($v = 0.60$) treatment caused much faster viable-cell decrease, and the complete population inactivation occurs after about 100 min of treatment.

The effect of AgNPs on the *E. coli* membrane integrity is shown in Figure 1b. The symbols are the percentages of the PI-positive cells as a function of time upon the produced colloid treatment. The cells were incubated with the AgNPs for 90 min at concentrations of $\frac{1}{2}$ MIC ($v = 0.15$), MIC ($v = 0.30$), and 2MIC ($v = 0.60$). Melittin was used as a positive control. The data are expressed as the mean values of percentages of the PI-positive cells \pm SD. PI, commonly used fluorescent stain for identifying permeabilized cells in a population, penetrates only cells with disrupted membranes and is generally excluded from viable cells [50]. The increase of the PI signal shows that the treatment of *E. coli* cells with the AgNPs caused significant inner membrane permeability at all tested concentrations (Figure 1b). This effect was dose and time-dependent with $\sim 40\%$ PI-positive cells after 15 min of treatment with AgNPs at $\frac{1}{2}$ MIC concentration, increasing to almost 90% after 90 min of treatment. Treatment with the AgNPs at the MIC concentration caused somewhat more damage with 94% PI-positive cells after 90 min of incubation. Interestingly, the treatment with AgNPs at the 2 MIC concentration resulted in a more rapid response, i.e., over 90% of all cells were PI-positive after 60 min of incubation. However,

after 90 min of treatment at the 2MIC concentration, the percentage of PI-positive cells did not change compared to treatment with AgNPs at MIC concentration.

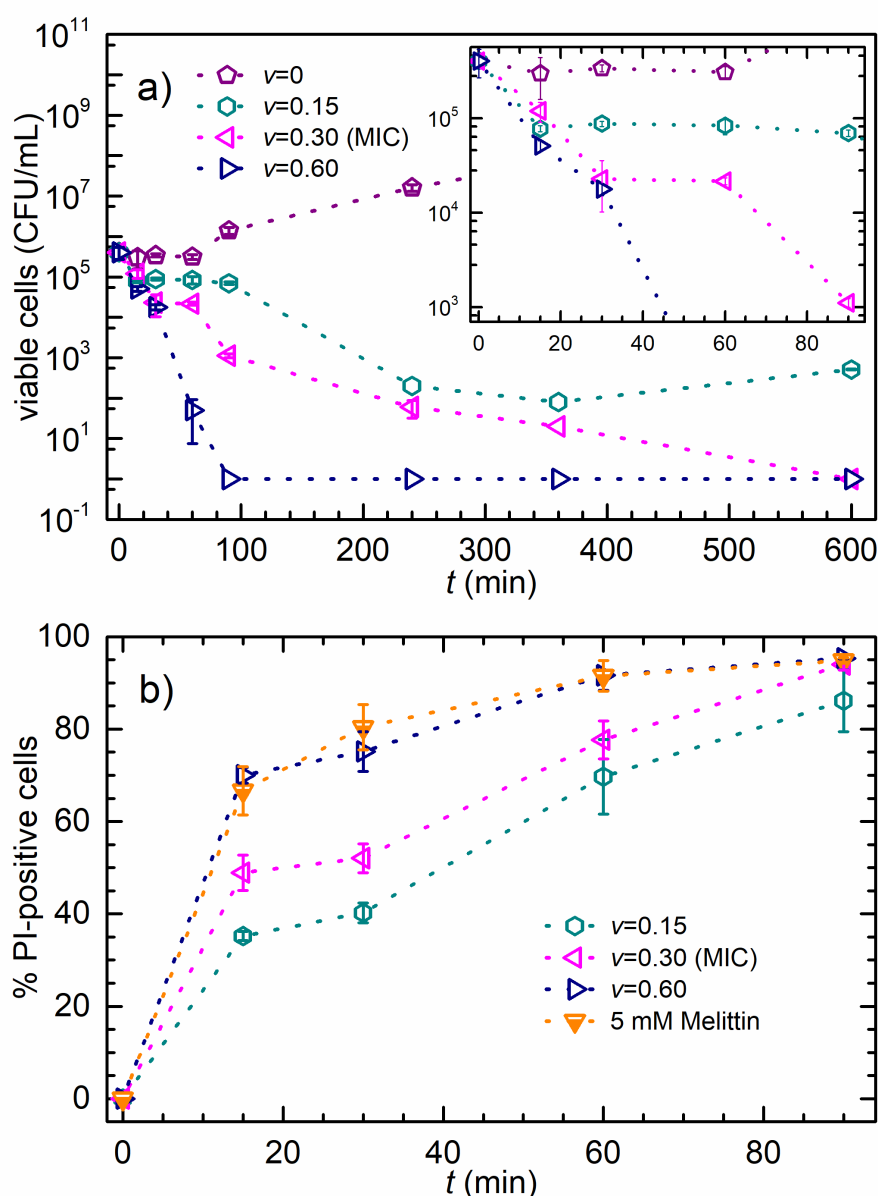


Figure 1. The time-killing and membrane integrity assays. (a) Viable-cell concentration versus time. The mean values of viable-cell concentration \pm SD for *E. coli* incubated with different AgNPs concentrations, as given in the legend. The inset is the first 90 min of the experiment. (b) Percentage of PI-positive cells versus time. The data represent the percentage of PI-positive cells \pm SD for *E. coli* incubated with different AgNPs concentrations, or with Melittin, as given in the legend.

Melittin was used as a positive control since it has a strong membranolytic effect [48]. Figure 1b shows that the 2MIC AgNPs and the 5 mM Melittin treatment have almost the same effect on bacterial membrane integrity. After 90 min of treatment with Melittin and AgNPs, most of the cells endured damage and the percentage of the PI+ cells is almost the same, for both MIC and 2MIC treatments.

Figure 2 shows the time dependence of the fluorescence signal developed when the DCFH₂-DA dye is added to samples containing different concentrations of AgNPs and H₂O₂. Figure 2a reveals the fluorescence signal obtained for non-inoculated dyed PBS and different AgNPs concentrations mixtures. All curves exhibit an increase in the fluorescence signal. The sample without nanoparticles

exhibits the highest signal at all-time points. The signal of each curve reduces as the concentration of the AgNPs increases. Figure 2a shows the mean values of the obtained quadruplet measurements for which the standard deviations were expressed as a percentage of the mean value. The mean values of standard deviations for each data set are: 6.9% ($v = 0$), 5.8% ($v = 0.01$), 7.0% ($v = 0.05$), 6.4% ($v = 0.10$), 7.1% ($v = 0.20$), 6.7% ($v = 0.25$) and 5.0% ($v = 0.30$). The inset shows the correlation between the non-inoculated and inoculated sample without AgNPs. Best linear fit for this correlation gives $y = (0.66x + 46)$ a.u., with $R^2 = 0.97$.

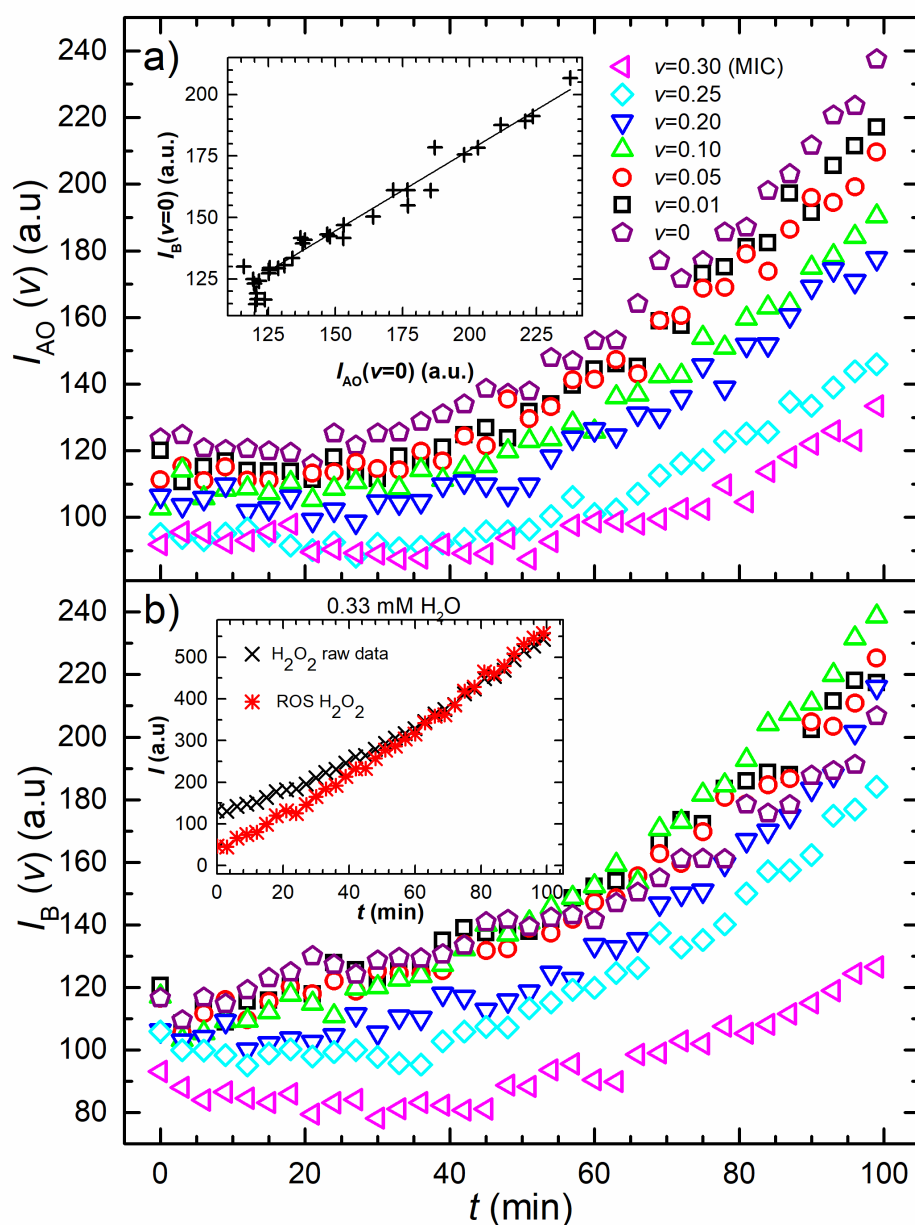


Figure 2. Evolution of the raw fluorescence data. (a) Raw fluorescence intensity versus time. Time dependence of the fluorescence signal developed when the DCFH₂-DA dye is diluted in non-inoculated PBS and mixed with the produced colloid. The legend reveals AgNPs concentrations in the mixture. The inset shows the correlation between the non-inoculated and inoculated samples raw fluorescence data that are AgNP-free ($v = 0$) and its linear fit. (b) Raw fluorescence intensity versus time. Time development of the fluorescence signal of the same mixture given in (a) when inoculated with *E. coli* cells. The cross-shaped symbols in the inset are the raw fluorescence signal of H₂O₂ treated *E. coli* cells and the double cross-shaped symbols are the cellular ROS data.

Figure 2b depicts the fluorescence data of the inoculated samples for the same AgNPs concentrations. The highest signal is obtained for $v = 0.15$ while the signals for $v = 0.05$ and $v = 0.01$ treatments are slightly smaller. The fluorescence signal initially decreases for $v = 0.25$ and $v = (\text{MIC})$ samples, before the increase prevails. When compared with the fluorescence data given in Figure 2a, the change in the total signal is expected to occur due to the intracellular ROS production, induced by the presence of AgNPs. Interestingly, the final fluorescence signal of inoculated samples is higher than the non-inoculated ones for all samples except two; the MIC-treated and the non-treated sample signal. The mean values of standard deviations for each data set are: 4.6% ($v = 0$), 6.7% ($v = 0.01$), 4.3% ($v = 0.05$), 4.0% ($v = 0.10$), 5.2% ($v = 0.20$), 4.5% ($v = 0.25$) and 5.9% ($v = 0.30$).

H_2O_2 is a known oxidizing and antibacterial agent to which the membranes are semi-permeable [51]. The fluorescence results obtained for the bacterial H_2O_2 treatment are shown in the inset of Figure 2b. The cross-shaped symbols are the raw fluorescence signal of H_2O_2 treated *E. coli* cells and the double cross-shaped symbols are the bacterial ROS fluorescence data, obtained as explained in the Discussion section. The mean value of standard deviations for the H_2O_2 raw data was obtained to be 4.2%.

The correlations between $v = 0$ and $v \neq 0$ fluorescence data of non-inoculated samples are given in Figure 3a. For all concentrations, the linear correlation is found with $R^2 \geq 0.98$. Please note that the $v = \text{MIC}$, $v = 0.25$, and $v = 0.20$ sample data deviate from linearity for $t < 36$ min. For these concentrations, the linear fit is applied for the $t \geq 36$ min. The concentration dependencies of the correlations' coefficient (slope) and the intercept are given in the inset of Figure 3a. The symbols are the data and the full lines are the one-parameter linear fits. The correlations' slope decreases with the concentration and the best linear fit, with intercept fixed to 1, is found to be $y = 1 - 1.92x$, with $R^2 = 0.99$.

Figure 3b shows the time evolution of the bacterial ROS signal extracted from the raw data, as explained in the Discussion section. Initially, the signal is higher for higher AgNPs concentrations. It increases in time with the concentration-dependent rate, except for the MIC sample, which initially decreases, and then increases, exhibiting a broad minimum at about 50 min. For the smallest tested AgNPs concentrations ($v = 0.01$, $v = 0.05$), the increase is low but for the higher concentrations ($v = 0.10$, $v = 0.20$, $v = 0.25$) it is rather significant. The highest final ROS signals were obtained for $v = 0.20$ and $v = 0.25$ samples. The inset shows concentration dependency of the ROS signal obtained at the beginning (full stars) and the end (full circles) of the treatment. The values are the signal averages of the three consecutive points. The ROS signal increases proportionally with concentration v , for $0.20 < v < 0.25$ assumes the maximal value of about 200 a.u. and then for $v = 0.30$ suddenly drops to about 50 a.u. Notably, the MIC treatment induces a significantly lower ROS level.

AFM data acquisition and analysis were used to obtain topography and YM of untreated and AgNP-treated cells. The obtained data are shown in Figure 4. All images have the 128×128 resolution, scan size of 10×10 micrometers and height color scale up to 1.5 micrometers, while the YM maps have the color scale up to 1 MPa. It takes about 40 min to collect a full AFM data set. For every pixel, the height of the sample is obtained, and the force-distance curve is measured. The YM of each pixel is calculated by fitting those curves. All redundant data points are excluded from the calculations since our interest is only in the YM of the bacterial cell and not of the surrounding substrate. YM data in Figure 4a–c reveal that the substrate/glass is very stiff with some randomly distributed soft points that can be attributed to the Cell-Tak coating.

The correlations' intercept increases proportionally with the concentration, and the best proportional fit is found to be $y = 107x$, with $R^2 = 0.92$.

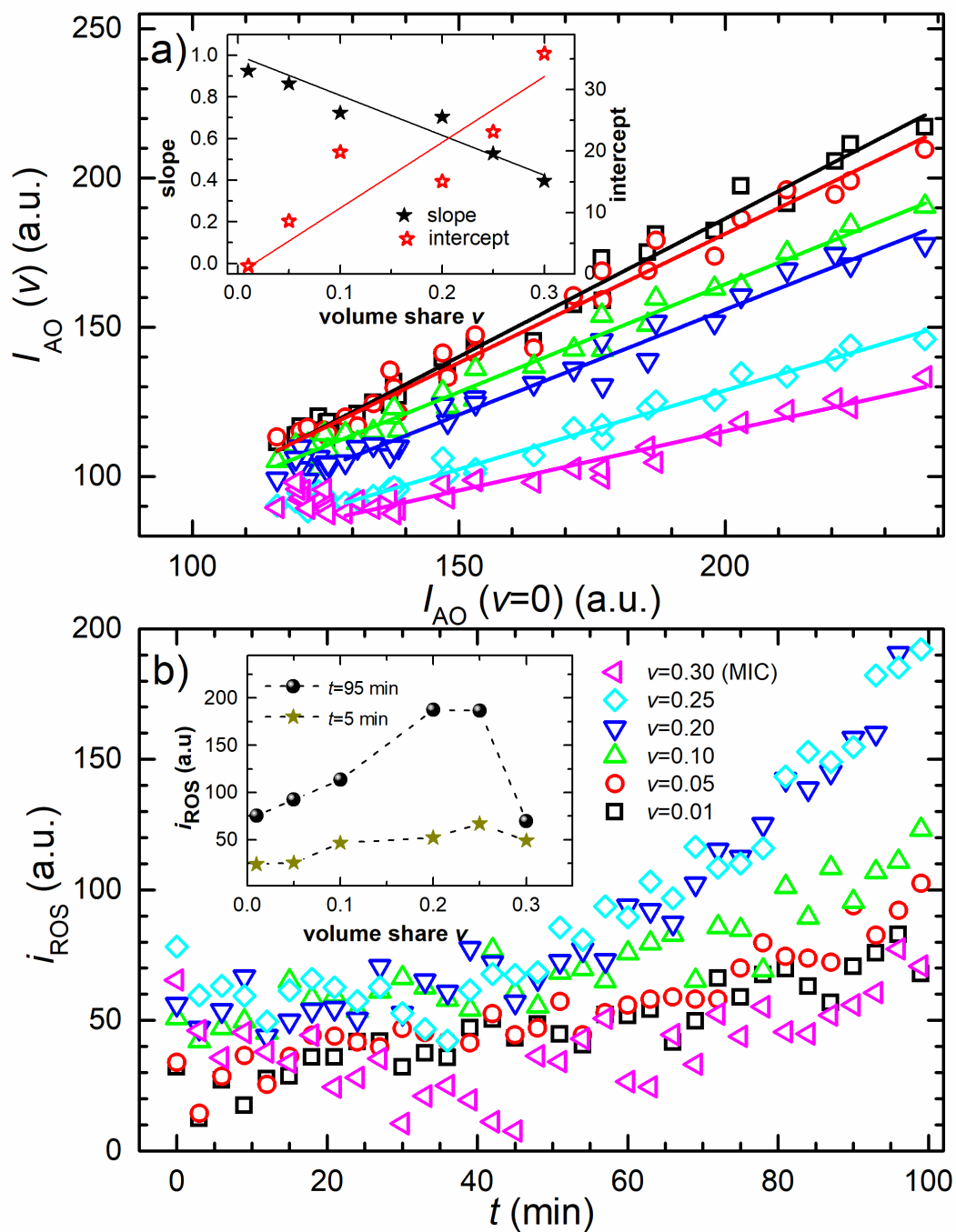


Figure 3. Fluorescence data analysis. (a) The correlation between $v = 0$ and $v \neq 0$ fluorescence intensity data from Figure 2a. The symbols are the experimental data and the lines are the best linear fits where the lines' length denotes the data range selected for each fit. The inset gives the slope (full stars) and the intercept (open stars) of the fits as a function of AgNPs concentration. Each data set is fitted to a line. (b) ROS fluorescence intensity versus time. Time evolution of the AgNP-induced bacterial ROS fluorescence (i_{ROS}) signal extracted from the raw data, as described in the Discussion section. The inset shows the concentration dependence of the i_{ROS} average for the first and last three time points. The AgNPs concentration is given in the legend.

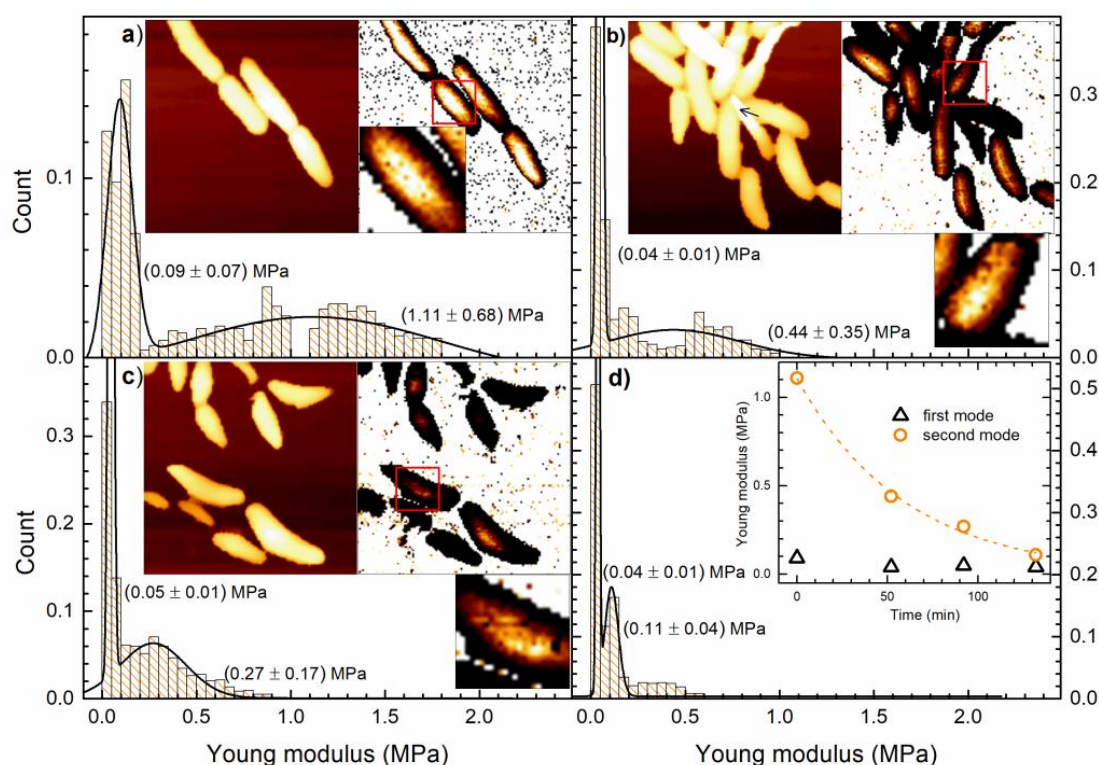


Figure 4. AFM data of non-treated and AgNPs treated *E. coli* cells at different times. Topography and YM maps are obtained for the same cell group and the data are collected at different pre- and post-treatment times. Larger images have 128×128 resolution, $10 \times 10 \mu\text{m}$ scan size, 0 to $1.5 \mu\text{m}$ height color scale, and 0 to 1 MPa YM color scale. Histograms, representing count versus Young modulus, are the distributions of the YM data selected within the 5% of the highest points for each scan line. The full lines are the bimodal normal distribution fits with means and the standard deviations given in parentheses. Parts of the YM maps marked with red squares are enlarged. (a) Non-treated bacterial cells height data (left image) and the corresponding calculated YM data (right image). (b) Treated bacterial cells height data (left image) and the corresponding calculated YM data (right image) whose scan began after 50 min of treatment. (c) The same as in (b) with the scan beginning after 90 min of treatment (d) The same as in (b) with the scan beginning after 130 min of treatment.

Figure 4a reveals the AFM topography image of non-treated bacteria given on the left side and the corresponding YM map on the right side. These cells are “the mother cells” of all other cells that are given in Figure 4b–d. It can be noticed that the YM increases as the height of the bacteria increases, i.e., the YM is apparently lower on the cells’ edges.

Due to the oval shape of the cell, the tip of the AFM probe is far from being perpendicular to the cell surface on the edges. Therefore, the Hertz model, for which the calculations of YM are performed, is not valid. Consequently, only data obtained on the top of the cell provide correct information on the bacterial YM. We have extracted and considered only the YM data that correspond to the top 5% of the height points of each scan line. This was done for all obtained YM data sets.

Figure 4a also gives the normalized distribution of the YM values, selected as described above, whose number is found to be 798. The normalized histogram indicates that the YM has a bimodal distribution. The full line is the corresponding bimodal normal distribution fit with the following mean values and standard deviations: (0.09 ± 0.07) MPa and (1.11 ± 0.69) MPa. The enlarged part of the map shows that the softer (darker) points, for which the YM is within (0.09 ± 0.07) MPa, are evenly distributed on the bacterial surface. Rough estimate is that the softer points (first four bins of the histogram) make about 30% of all scanned points.

Figure 4b shows the height and YM map for the AgNPs treated cells. Data collection started about 50 min after the start of the treatment. It can be noted, by comparing the cell morphologies in Figure 4a,b, that the bacterial overall shape and appearance has not changed. In Figure 4b, there are a few cells (denoted by an arrow) that appear to be narrower on one end since this end is loosely attached. This occurs when bacteria stop growing in a monolayer and are stacked on top of each other. The YM data that correspond to these loosely attached parts of bacterial cells were excluded from the histogram. The number of YM points selected for the analysis is 598.

Figure 4b shows that after the treatment, the distribution of YM data remains bimodal, but with modified means and the standard deviations: (0.04 ± 0.01) MPa and (0.44 ± 0.35) MPa. It should be noted that both YM means are now shifted to lower values. The YM data reveal the softening of the bacterial cells. The YM distribution for the softer regions is narrower. These softer regions on top of the cells are evenly distributed and more numerous (when compared to non-treated cells), as can be observed on the enlarged YM map. The rough estimate is that the softer YM population (first two bins of the histogram) now makes about 50% of all YM points.

Figure 4c shows the topography and YM maps obtained for the same cell group. The data acquisition started after 90 min of treatment. By comparing this topography with the topography of untreated cells of Figure 4a, it can be noted that some cells are now shorter and that the YM modulus data reveal further softening of the cells. It can also be seen that some cells are surrounded by some soft matter. The mean values and the standard deviations obtained from the bimodal YM distribution are (0.04 ± 0.01) MPa and (0.27 ± 0.17) MPa, and the number of the used YM points is 834. The softer regions retain the same stiffness, while the stiffer regions become even softer with the sharper distribution. The softer YM population, which makes about 50% of all YM points, remains unchanged. These softer regions of the cell may be observed on the enlarged YM map.

The acquisition of the data presented in Figure 4d began 130 min after the AgNPs have been added to the culture. The means and the standard deviations obtained for the YM histogram are (0.04 ± 0.01) MPa and (0.13 ± 0.24) MPa, and the number of selected YM points is 729. Once again, the softer regions are unaltered, while the stiffer ones become softer. The population of the softer YM points (first bin of the histogram) makes about 50% of all YM points and its distribution sharpens.

The inset of Figure 4d shows the change of the YM mean values with time. The triangles are the YM mean values for softer regions (first mode), while the circles are the YM mean values for stiffer regions (second mode). It can be noted that soon after the beginning of the treatment, the YM of the soft regions drops to half its initial value and then remains constant, while YM of the stiff regions decreases all the time. The dotted line is the exponential fit of the YM data of the stiffer region. The fit is given by the equation $y = 1.1e^{-0.02x}$ with $R^2 = 0.99$.

Bright-field images were obtained before and after the AgNPs treatment. Figure 5a,b show untreated cells before and after AFM scans, respectively. It is visible that the cells have divided proving that the probe does not interfere with the cells' viability. Bacteria given in Figure 5a are "the mother cells" to all bacteria in subsequent Figure 5b–f. Figure 5c shows the region of interest immediately after the treatment. Figure 5d, taken after 3 h of treatment, shows that the cell division does not cease immediately after the treatment. The image reveals that the cells' number has increased sometime during the treatment. Figure 5e,f are the fluorescence signal of SYTO 9 and PI, respectively. SYTO 9 stains all bacterial cells, while the PI signal of bacteria appears only if the membrane is permeabilized. When both dyes are present at once, PI exhibits a stronger affinity towards nucleic acids than SYTO 9, so SYTO 9 is displaced by PI [50]. Figure 5e reveals that the green signal of *E. coli* is reduced, and the signal seems to be shifted towards the yellow. Figure 5f shows that all *E. coli* cells have been permeabilized and every red-colored region of the image belongs to a rod-shaped bacterial cell.

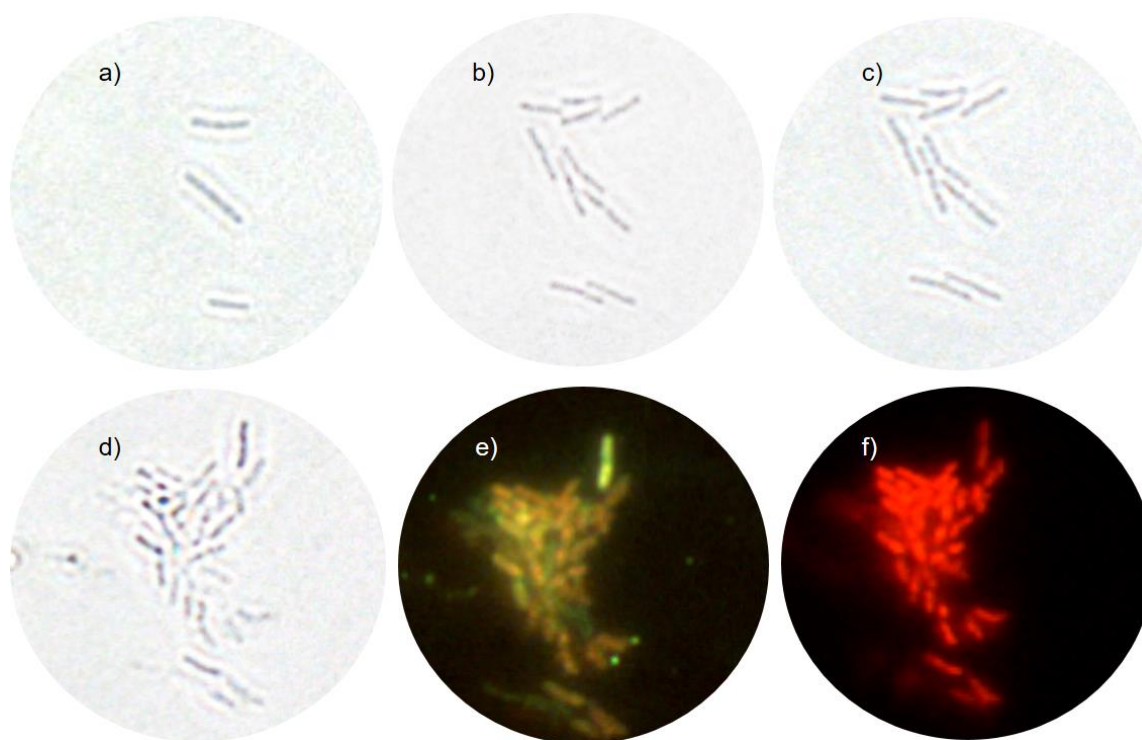


Figure 5. Optical microscopy data of non-treated and treated *E. coli* cells. (a) Bright-field image of the initial “mother cells” before AFM imaging. (b) Bright-field image taken after AFM of non-treated cells, about 1.5 h after the (a) image. (c) Bright-field image taken after a few minutes of treatment. (d) Bright-field image taken after 3 h of treatment. (e) SYTO 9 fluorescence image taken after 3 h of treatment. (f) PI fluorescence image taken after 3 h of treatment.

4. Discussion

The consistency of *E. coli* cell membrane and bacterial viability were studied upon AgNPs’ treatment to elucidate possible correlation of membrane perturbation with the observed bactericidal effect. The important question is whether the AgNPs permeabilize the cells and if so, how this influences the cell viability. Please note that the PI molecule enters the cells only if they are membrane-permeabilized. After 90 min of the treatment with $\frac{1}{2}$ MIC dose, we found that 86% of cells were PI-positive, as shown in Figure 1b. After the same period, the time-killing assay revealed the 80% reduction of the viable-cell population, as shown in the inset of Figure 1a. These results demonstrate that the PI-positive cells are also non-viable and that the membrane permeabilization is closely related to the AgNPs’ antibacterial mode of action. The 90-min treatment at a concentration corresponding to the MIC value induced PI permeabilization for 94% of the bacterial population, i.e., only 6% of the population remained possibly viable, while the time-killing assay indicated less than 0.3% of viable cells. These MIC data reveal that not all non-viable cells are also PI-positive, so we conclude that the permeabilization of the membrane might not be the only killing mechanism.

It was not possible to compare the AFM data with the time-killing assay data at 2MIC since the growing conditions for the two experiments were quite different, due to the impossibility of shaking the AFM sample during incubation. However, Figure 5f clearly shows that after 3 h of treatment all cells (shown in Figure 5e) are PI-positive, which means that scanned cells in Figure 4d were not viable.

It is widely accepted that cell stress is related to the intracellular ROS level. DCFH₂-DA fluorescence probe, which diffuses through the cell membrane, is used to measure the bacterial ROS creation during the AgNPs treatment. Due to the intracellular esterases, DCFH₂-DA deacetylates to non-fluorescent but membrane-impermeable DCFH₂, which reacts with intracellular ROS to produce the fluorescent DCF [27]. This probe was proved to be suitable as a marker for the total ROS production [27] and is the

most widely used fluorescent probe for detecting intracellular H_2O_2 [52]. However, it is difficult to extract the ROS fluorescence signal from the total signal generated in the sample. There are two main reasons for this. The first is that the cellular ROS must be resolved from the contribution of the probe's autooxidation signal. The second is the attenuation of the light by absorption and/or scattering on both the nanoparticles and the cells, which are present in the measured sample.

Two fluorescence experiments were performed to obtain the dependence of the bacterial ROS signal $i_{ROS}(v,t)$ on the AgNPs' concentration and time: first for different concentrations of AgNPs in dyed PBS without bacteria and the second for the same samples but inoculated with bacteria. The results are shown in Figure 2. Figure 2a shows the time dependence of the signal $I_{AO}(v,t)$ that appears in the non-inoculated sample, due to the self-oxidation of the probe for different AgNPs concentrations. The signal increases in time as the oxidation progresses. It also decreases with the AgNPs concentration increase due to their absorption/scattering of the light. A similar masking effect for the DCF fluorescence signal has been reported for iron oxide nanoparticles [53] while coated AgNPs were shown to decrease ROS level due to fluorescence quenching and adsorption of the fluorescent dye [28].

To obtain the influence of bacteria on the fluorescence signal, we compare the signal of the inoculated dyed PBS buffer $I_B(0,t)$ with the autooxidation signal $I_{AO}(0,t)$ of the non-inoculated dyed PBS buffer. As shown in the inset of Figure 2a, the correlation between the two signals is linear and it can be written in the form:

$$I_B(0,t) = k_B I_{AO}(0,t) + I_{B0}, \quad (1)$$

where $k_B = 0.66$ is the attenuation coefficient and the intercept $I_{B0} = 46$ a.u. is the constant which depends on the time of preparation of the samples and the offset of the instrument. Bacteria attenuate the existing fluorescence signal throughout the absorption/scattering of the light. This correlation (Equation (1)) proves that within the accuracy of the experiment, there is no additional fluorescence signal generated by bacteria, i.e., bacteria in the dyed PBS buffer do not produce ROS.

The nanoparticles act similarly. They absorb and scatter both the incident light, coming from the instrument's lamp to the probe in the sample, and the fluorescent light emitted by the molecule. It is reasonable to assume that for low concentrations of the AgNPs, the absorption/scattering coefficient is proportional to the concentration v so that the intensity of the incident light on its path to the molecule is reduced by the factor $(1 - k_i v)$. Similarly, the intensity of the fluorescent light on its path out the sample is reduced by the factor $(1 - k_f v)$, where k_i and k_f are the constants that for a given sample geometry, depend on the wavelength. The UV-visible absorption spectrum of the LAL-synthesized AgNPs exhibits a typical sharp peak at 404 nm due to nanoparticle's surface plasmon band absorption [45]. The absorption of the fluorescence light, emitted by DCF at $\lambda = 523$ nm, is about half the maximum but is still strong enough to produce the observed fluorescence signal reduction.

Under these assumptions, the fluorescence signal which should be obtained for AgNPs concentration v ,

$$I_f(v,t) = (1 - k_f v)(1 - k_i v)I_f(0,t) \quad (2)$$

can be related to the fluorescence signal $I_f(0,t)$, obtained for the nanoparticle-free sample. For the low nanoparticle concentrations, the quadratic term in v can be neglected. Therefore, Equation (2) assumes a linear form

$$I_f(v,t) = (1 - k_{NP}v)I_f(0,t), \quad (3)$$

where $k_{NP} = k_f + k_i$.

Taking into account that the measured intensities differ from the actual values by the constant I_0 , which could appear e.g., due to the offset of the instrument, Equation (3) can be rewritten in terms of the measured quantities as

$$I_{AO}(v,t) - I_0 = (1 - k_{NP}v)(I_{AO}(0,t) - I_0), \quad (4)$$

where $I_{AO}(v, t)$ is the measured fluorescence for the non-inoculated samples (see Figure 2a). Equation (4) gives a linear correlation

$$I_{AO}(v, t) = (1 - k_{NP}v)I_{AO}(0, t) + k_{NP}vI_0 \quad (5)$$

between the measured $I_{AO}(v, t)$ and $I_{AO}(0, t)$, with the correlation coefficient being a linear function of v whose intercept is equal to 1. The assumptions on the role of AgNPs in the dyed PBS buffer, as given in Equation (5), are confirmed by the correlation analysis of the fluorescence data shown in Figure 3a. The slopes and intercepts obtained from the linear correlations given in Figure 3a were proven to have linear dependencies on the nanoparticle concentration, as shown in the inset of Figure 3a.

Therefore, we conclude that the influence of the AgNPs on the autooxidation of the dye is negligible. The decrease in fluorescence signal, which appears when the AgNPs are added to the batch, appears only because of light absorption and scattering by the nanoparticles.

The evolution of the fluorescence signal for the inoculated samples $I_B(v, t)$ is shown in Figure 2b. The non-treated-bacteria signal starts with the highest intensity and then gradually drops below the signals obtained for the treated cells. For the MIC-treated bacteria, the signal starts with the lowest intensity and is almost constant for about 40 min after which it increases. These results can be explained in terms of the AgNPs' double effect. They stimulate cells' ROS creation, which increases the fluorescence signal, but they also absorb and scatter the incident/emitted light which results in signal reduction. The latter applies to both fluorescence signals: the abiotic one $I_{AO}(0, t) - I_0$ that appears in the sample without the cells and the ROS related signal $i_{ROS}(v, t)$ coming from inside the cell. The total measured signal $I_B(v, t)$ is the sum of those two signals multiplied by reduction factors of the nanoparticles and the bacteria and, similarly as for Equation (4), can be written in the form:

$$I_B(v, t) - I_0 = k_B(1 - k_{NP}v)(I_{AO}(0, t) - I_0 + i_{ROS}(v, t)). \quad (6)$$

Please note that the actual and measured values differ for the offset I_0 . From Equation (6) we obtain

$$i_{ROS}(v, t) = \frac{I_B(v, t) - I_0}{k_B(1 - k_{NP}v)} - I_{AO}(0, t) + I_0. \quad (7)$$

Knowing the parameters k_B , k_{NP} and I_0 , and obtaining the fluorescence response of the $I_{AO}(0, t)$ sample, Equation (7) enables the extraction of the fluorescence signal due to the intercellular ROS from the $I_B(v, t)$ raw data. The parameter $k_B = 0.66$, which is related to the fluorescence signal attenuation due to the scattering on the bacterial cells, is the correlation coefficient of the fit given in the inset of Figure 2a. The parameter $k_{NP} = 1.92$, which refers to the fluorescence signal attenuation due to the scattering/absorption of the AgNPs, is the correlation coefficient of the slopes' fit given in the inset of Figure 3a. According to Equation (5), the parameter I_0 is obtained by dividing the correlation coefficients of the linear fits given in the inset of Figure 3a, i.e., $I_0 = \frac{107}{1.92} = 55.8$ a.u.

It is reasonable to presume that the extracted $i_{ROS}(v, t)$, shown in Figure 3b, is proportional to the level of the cellular ROS which is dose- and time-dependent. Sub-MIC treatments, for which the bacterial population is not terminally threatened, gives the response of metabolically active cells on a chosen time scale. If the ROS production would be the dominant antibacterial mode of action, the ROS level should increase with the AgNPs concentration and the MIC treatment should result in the highest ROS level. The ROS level dependency is given in the inset of Figure 3b, for $t = 5$ min and $t = 95$ min. It can be seen (for $t = 95$ min) that the ROS level increases with the AgNPs concentration up to 2/3 MIC ($v = 0.20$), assumes the maximum, and then suddenly drops for the MIC treatment. ROS level obtained at $t = 95$ min for the MIC treatment is 3 times lower than for 5/6 MIC ($v = 0.25$) treatment. The highest ROS level is significantly (about 3 times) lower than the ROS level developed for the treatment with 0.33 mM H_2O_2 . Please note that the later time-dependent level of ROS was obtained from Equation (7) for $v = 0$, and is given in double cross-shaped symbols in the inset of Figure 2b.

Altogether, it is reasonable to conclude that the ROS induced oxidative stress is not the predominant antibacterial mode of action of the LAL-synthesized AgNPs against *E. coli*. The ROS level does

significantly increase with the AgNPs dose and time, but only for the sub-MIC dose and is still notably lower when compared to the H₂O₂ induced ROS level. Our results show that ROS production is related to the antibacterial mode of action for sub-MIC AgNPs treatments, but not for the MIC treatment.

The results on the time evolution of the DCF fluorescence signal in *E. coli* treated with AgNPs [33] are scarce. Published data are raw, which cannot be compared with our ROS data obtained by careful analysis of the fluorescence signal. Interestingly, time dependency of the DCF fluorescence signal given in Figure 2a reveals functional dependency similar to the DCF fluorescence signal of the graphene oxide (GO) and poly (methyl 2-methylpropenoate) (PMMA) fiber mixture [54]. However, the DCF signal of GO/PMMA develops longer lag with the final intensity very close to the H₂O₂ DCF signal. Also, according to the baseline data, it seems that the GO/PMMA mixture does not induce the scattering/absorbance effect as AgNPs do.

To explore the possible treatment-induced alterations, the AgNP-treated bacterial cells were inspected by AFM. The YM was measured since the inspection of the morphology did not give a significant difference between the non-treated and treated cells for all times. We used the QI mode which enables simultaneous imaging and measurement of mechanical properties of bacterial cells [55]. YM was obtained from the force–distance curves by applying the Hertz model for spherical indenters [56].

The YM map of viable non-treated cells, given in Figure 4a, reveals that the periphery of the bacterial cell is apparently more deformable than the apex. This effect occurs due to the curvature of the cell, i.e., the applied force is not normal to the cell [57]. To avoid this artifact the analysis was performed only for the curves obtained from the central region of the cells [58].

The reported average values of YM for untreated *E. coli* vary by several orders of magnitude, as shown in Table 1 in [59]. This might be attributed to the conditions under which the data were obtained such as measurements on the dried bacterial samples. Our YM data are obtained on viable *E. coli* cells in the growth medium. The novel result in our AFM study, which could be of particular interest, is the bimodal distribution of the YM of untreated *E. coli* cells. The distribution has two clearly split maxima that differ in value for an order of magnitude. The softer regions are randomly distributed on the cell surface and cannot be attributed to, for example, an ongoing cell division, which would induce localized YM alterations.

Some findings in the literature could be related to the observed YM variation and inhomogeneity of untreated cells. It is worth noting that DH5 α strain is commonly used to maintain and amplify small plasmid DNA [60]. Also, it has been shown that induction of competence for transformation causes pores which can be entry points for macromolecules [61]. Production of calcium competent cells results in pore formation during the heating step [62] and the shockwave transformation causes an increase in YM of dehydrated cells [63]. We speculate that softer parts of the cell could be predestined as the future points of pore formation. However, this hypothesis demands thorough research.

Post-treatment YM histograms, given in Figure 4, reveal the narrowing of the stiffer YM distribution and the shift of its maximum towards the lower values. We presume that the narrowing of the YM distribution is an indicator of metabolic activity reduction. YM map given in Figure 4c, obtained for 90 min of bacterial treatment, reveal softer regions next to the cells. This might be an indicator of the intracellular matter leakage due to cell membrane damage/lysis. It is also worth noting that the YM maximum of stiffer regions decreases exponentially in time with the time constant of about 50 min, as indicated in the inset of Figure 4d. Since the data given in the histogram in Figure 4d are obtained for non-viable cells, it is clear that the cell viability can be related to the softening of the stiffer parts of the cell.

It has been found that the 4 nm SiO₂ NPs induce the de-structuration of the peptidoglycan layer and lead to the cell lysis [64]. Our results reveal that the mode of antibacterial action of AgNPs is related to the time-dependent softening of the treated cell and possible cell lysis, which might be due to the de-structuration of the peptidoglycan layer.

The treated cells were monitored by the bright-field and fluorescence microscopy to obtain additional cell viability data before and after AFM data acquisition. Figure 5a,b of untreated cells show

that AFM imaging does not influence bacterial viability. Figure 5c,d prove that cell growth does not cease immediately upon treatment. This finding is in line with the dynamic nature of the population lag as reported in the model of the AgNP-treated *E. coli* growth [45], which assumes that cells that have not been inactivated continue to grow during treatment. A broad minimum in viable-cell number for the $\frac{1}{2}$ MIC treatment (Figure 1a) is also per the model. The fluorescence data in Figure 5e,f reveals that all cells are non-viable after 3 h of treatment.

5. Conclusions

The effect of AgNPs treatment on the consistency of the cell membrane and the cell viability is studied through the fluorescence of the PI probe and plating, respectively. The obtained data reveal that PI-positive cells are non-viable, but at the same time, some non-viable bacteria were not PI-positive, leading to the conclusion that permeabilization of the membrane might not be the only killing mechanism.

The change in bacterial ROS level during the AgNPs treatment was obtained from the DCF fluorescence signal. Two experiments were performed to resolve the cellular ROS from the total fluorescence signal: for different concentrations of AgNPs in dyed PBS without bacteria and for the same samples but inoculated with *E. coli* cells. The results showed that the fluorescence signal increases in time but reduces with nanoparticle concentration. Besides the contribution of the probe's autooxidation effect, these results can be explained in terms of the nanoparticles' double effect. Specifically, AgNPs stimulate cellular ROS production which increases the fluorescence signal, but they also absorb and scatter the incident/emitted light which results in a signal reduction.

From the linear correlation between the inoculated dyed PBS buffer signal and the autooxidation signal of the non-inoculated dyed PBS buffer, we conclude that non-treated bacteria do not produce ROS. Similarly, from a linear correlation between dyed PBS buffer signals with different AgNPs concentrations, we conclude that the influence of the AgNPs on the autooxidation of the dye is negligible. The decrease in the fluorescence signal, which appears when the AgNPs are added to the non-inoculated batch, appears only because of light absorption and scattering by the nanoparticles.

This analysis enables the extraction of the cellular ROS level from the total fluorescence signal and further conclusions.

The obtained cellular ROS level is dose- and time-dependent. The ROS level does significantly increase with the AgNPs dose and time, but only for the sub-MIC dose and is still about 3 times lower when compared to the H₂O₂ induced ROS level. Given the fact that ROS assumes the highest level for the sub-lethal dose, we conclude that the ROS induced oxidative stress is not the predominant antibacterial mode of action of LAL-synthesized AgNPs against *E. coli*.

YM was obtained from the force–distance curves measured at the topmost parts of bacteria. We found that the distribution of the YM data of untreated *E. coli* cells is bimodal, which is particularly interesting. The distribution has two clearly split maxima that differ in value for an order of magnitude. The softer regions are randomly distributed on the cell's surface.

During the AgNPs treatment, the bacterial YM histograms reveal the narrowing of the stiffer YM maximum and its softening, i.e., shift towards the lower values, which can indicate the metabolic activity reduction. YM data of treated cells also reveal softer regions next to the cells, which might be an indicator of the intracellular matter leakage due to cell lysis. Fluorescence microscopy images of the AFM-inspected AgNPs treated cells have shown that all cells have been PI permeabilized i.e., inactivated.

Bright-field microscopy of the treated cells shows that the cells' growth does not cease immediately upon treatment. This finding is in line with the dynamic nature of the population lag as reported in the model of the AgNP-treated *E. coli* growth [45], which assumes that cells that have not been inactivated continue to grow.

Altogether, our results indicate that the LAL-synthesized AgNPs mode of antibacterial action includes an increase of the cellular ROS level and destabilization of the cell membrane which includes

reduction of its YM and possible cell leakage. We found ROS induced oxidative stress not to be the main killing mechanism.

The bimodal distribution of YM found for the untreated *E. coli* cells is a novel result that could be of general interest in understanding the membrane structure and motivate us for further work.

Author Contributions: Conceptualization, L.K. and I.A.; methodology, L.K. and I.A.; validation, L.K.; formal analysis, L.K. and I.A.; investigation, L.K., M.Š., A.M., T.R., V.Č.Č., D.B. and N.K.; writing—original draft preparation, L.K. and I.A.; writing—review and editing, L.K. and I.A.; visualization, L.K.; funding acquisition, I.A. and N.K. All authors have read and agreed to the published version of the manuscript.

Funding: This research was supported by the Croatian Science Foundation under the project IP-2019-04-6418. This research was supported by the Croatian Science Foundation under the project PZS-2019-02-5276. This research was supported by the bilateral CRO-SAD project 2/2019. This research was partially supported under the project STIM-REI, Contract Number: KK.01.1.1.01.0003, a project funded by the European Union through the European Regional Development Fund—the Operational Programme Competitiveness and Cohesion 2014–2020 (KK.01.1.1.01).

Conflicts of Interest: The authors declare no conflict of interest.

References

1. Panáček, A.; Smékalová, M.; Kilianová, M.; Pucek, R.; Bogdanová, K.; Věčerová, R.; Kolár, M.; Havrdová, M.; Płaza, G.A.; Chojniak, J.; et al. Strong and nonspecific synergistic antibacterial efficiency of antibiotics combined with silver nanoparticles at very low concentrations showing no cytotoxic effect. *Molecules* **2016**, *21*, 1–17.
2. Masri, A.; Anwar, A.; Ahmed, D.; Siddiqui, R.B.; Shah, M.R.; Khan, N.A. Silver nanoparticle conjugation-enhanced antibacterial efficacy of clinically approved drugs cephadrine and vildagliptin. *Antibiotics* **2018**, *7*, 100. [[CrossRef](#)] [[PubMed](#)]
3. Ahonen, M.; Kahru, A.; Ivask, A.; Kasemets, K.; Kõljalg, S.; Mantecca, P.; Vinković Vrček, I.; Keinänen-Toivola, M.; Crijns, F. Proactive Approach for Safe Use of Antimicrobial Coatings in Healthcare Settings: Opinion of the COST Action Network AMiCI. *Int. J. Environ. Res. Public Health* **2017**, *14*, 366. [[CrossRef](#)] [[PubMed](#)]
4. Zorraquín-Peña, I.; Cueva, C.; Bartolomé, B.; Moreno-Arribas, M.V. Silver Nanoparticles against Foodborne Bacteria. Effects at Intestinal Level and Health Limitations. *Microorganisms* **2020**, *8*, 132.
5. Ivask, A.; ElBadawy, A.; Kaweeteerawat, C.; Boren, D.; Fischer, H.; Ji, Z.; Chang, C.H.; Liu, R.; Tolaymat, T.; Telesca, D.; et al. Toxicity Mechanisms in Escherichia coli Vary for Silver Nanoparticles and Differ from Ionic Silver. *ACS Nano* **2014**, *8*, 374–386. [[PubMed](#)]
6. Kubo, A.L.; Capjak, I.; Vrček, I.V.; Bondarenko, O.M.; Kurvet, I.; Vija, H.; Ivask, A.; Kasemets, K.; Kahru, A. Antimicrobial potency of differently coated 10 and 50 nm silver nanoparticles against clinically relevant bacteria Escherichia coli and Staphylococcus aureus. *Colloids Surfaces B Biointerfaces* **2018**, *170*, 401–410.
7. Slavin, Y.N.; Asnis, J.; Häfeli, U.O.; Bach, H. Metal nanoparticles: Understanding the mechanisms behind antibacterial activity. *J. Nanobiotechnol.* **2017**, *15*, 1–20. [[CrossRef](#)]
8. Bondarenko, O.; Ivask, A.; Käkinen, A.; Kurvet, I.; Kahru, A. Particle-Cell Contact Enhances Antibacterial Activity of Silver Nanoparticles. *PLoS ONE* **2013**, *8*, e64060. [[CrossRef](#)]
9. Xiu, Z.; Zhang, Q.; Puppala, H.L.; Colvin, V.L.; Alvarez, P.J.J. Negligible Particle-Specific Antibacterial Activity of Silver Nanoparticles. *Nano Lett.* **2012**, *12*, 4271–4275. [[CrossRef](#)]
10. Durán, N.; Durán, M.; de Jesus, M.B.; Seabra, A.B.; Fávaro, W.J.; Nakazato, G. Silver nanoparticles: A new view on mechanistic aspects on antimicrobial activity. *Nanomed. Nanotechnol. Biol. Med.* **2016**, *12*, 789–799. [[CrossRef](#)]
11. Dakal, T.C.; Kumar, A.; Majumdar, R.S.; Yadav, V. Mechanistic Basis of Antimicrobial Actions of Silver Nanoparticles. *Front. Microbiol.* **2016**, *7*, 1–17.
12. Cui, Y.; Zhao, Y.; Tian, Y.; Zhang, W.; Lü, X.; Jiang, X. The molecular mechanism of action of bactericidal gold nanoparticles on Escherichia coli. *Biomaterials* **2012**, *33*, 2327–2333. [[CrossRef](#)] [[PubMed](#)]
13. Zhao, Y.; Ye, C.; Liu, W.; Chen, R.; Jiang, X. Tuning the composition of AuPt bimetallic nanoparticles for antibacterial application. *Angew. Chem. Int. Ed.* **2014**, *53*, 8127–8131.

14. Li, M.; Ma, Z.; Zhu, Y.; Xia, H.; Yao, M.; Chu, X.; Wang, X.; Yang, K.; Yang, M.; Zhang, Y.; et al. Toward a Molecular Understanding of the Antibacterial Mechanism of Copper-Bearing Titanium Alloys against *Staphylococcus aureus*. *Adv. Healthc. Mater.* **2016**, *5*, 557–566. [[PubMed](#)]
15. Liu, S.; Zeng, T.H.; Hofmann, M.; Burcombe, E.; Wei, J.; Jiang, R.; Kong, J.; Chen, Y. Antibacterial activity of graphite, graphite oxide, graphene oxide, and reduced graphene oxide: Membrane and oxidative stress. *ACS Nano* **2011**, *5*, 6971–6980. [[CrossRef](#)] [[PubMed](#)]
16. Leung, Y.H.; Xu, X.; Ma, A.P.Y.; Liu, F.; Ng, A.M.C.; Shen, Z.; Gethings, L.A.; Guo, M.Y.; Djurišić, A.B.; Lee, P.K.H.; et al. Toxicity of ZnO and TiO₂ to *Escherichia coli* cells. *Sci. Rep.* **2016**, *6*, 1–13.
17. Siddiqi, K.S.; Husen, A.; Rao, R.A.K. A review on biosynthesis of silver nanoparticles and their biocidal properties. *J. Nanobiotechnol.* **2018**, *16*, 14. [[CrossRef](#)]
18. Slepíčka, P.; Kasálková, N.S.; Siegel, J.; Kolská, Z.; Švorčík, V. Methods of gold and silver nanoparticles preparation. *Materials (Basel)* **2020**, *13*, 1. [[CrossRef](#)]
19. Lugarà, P.; Volpe, A.; Sportelli, M.; Ancona, A.; Picca, R.; Palazzo, G.; Clemente, M.; Cioffi, N.; Izzi, M. The Pros and Cons of the Use of Laser Ablation Synthesis for the Production of Silver Nano-Antimicrobials. *Antibiotics* **2018**, *7*, 67.
20. Li, W.-R.; Xie, X.-B.; Shi, Q.-S.; Zeng, H.-Y.; OU-Yang, Y.-S.; Chen, Y.-B. Antibacterial activity and mechanism of silver nanoparticles on *Escherichia coli*. *Appl. Microbiol. Biotechnol.* **2010**, *85*, 1115–1122. [[CrossRef](#)]
21. SonDI, I.; Salopek-Sondi, B. Silver nanoparticles as antimicrobial agent: A case study on *E. coli* as a model for Gram-negative bacteria. *J. Colloid Interface Sci.* **2004**, *275*, 177–182. [[CrossRef](#)] [[PubMed](#)]
22. Chwalibog, A.; Sawosz, E.; Hotowy, A.; Szeliga, J.; Mitura, S.; Mitura, K.; Grodzik, M.; Orłowski, P.; Sokolowska, A. Visualization of interaction between inorganic nanoparticles and bacteria or fungi. *Int. J. Nanomed.* **2010**, *5*, 1085–1094. [[CrossRef](#)] [[PubMed](#)]
23. Korshed, P.; Li, L.; Liu, Z.; Wang, T. The Molecular Mechanisms of the Antibacterial Effect of Picosecond Laser Generated Silver Nanoparticles and Their Toxicity to Human Cells. *PLoS ONE* **2016**, *11*, e0160078. [[CrossRef](#)] [[PubMed](#)]
24. Ali, S.; Perveen, S.; Ali, M.; Jiao, T.; Sharma, A.S.; Hassan, H.; Devaraj, S.; Li, H.; Chen, Q. Bioinspired morphology-controlled silver nanoparticles for antimicrobial application. *Mater. Sci. Eng. C* **2020**, *108*, 110421. [[CrossRef](#)]
25. Składanowski, M.; Wypij, M.; Laskowski, D.; Golińska, P.; Dahm, H.; Rai, M. Silver and gold nanoparticles synthesized from *Streptomyces* sp. isolated from acid forest soil with special reference to its antibacterial activity against pathogens. *J. Clust. Sci.* **2017**, *28*, 59–79. [[CrossRef](#)]
26. Ramalingam, B.; Parandhaman, T.; Das, S.K. Antibacterial Effects of Biosynthesized Silver Nanoparticles on Surface Ultrastructure and Nanomechanical Properties of Gram-Negative Bacteria viz. *Escherichia coli* and *Pseudomonas aeruginosa*. *ACS Appl. Mater. Interfaces* **2016**, *8*, 4963–4976. [[CrossRef](#)]
27. Chen, X.; Zhong, Z.; Xu, Z.; Chen, L.; Wang, Y. 2',7'-Dichlorodihydrofluorescein as a fluorescent probe for reactive oxygen species measurement: Forty years of application and controversy. *Free Radic. Res.* **2010**, *44*, 587–604. [[CrossRef](#)]
28. Vinković Vrček, I.; Pavičić, I.; Crnković, T.; Jurašin, D.; Babić, M.; Horák, D.; Lovrić, M.; Ferhatović, L.; Ćurlin, M.; Gajović, S. Does surface coating of metallic nanoparticles modulate their interference with in vitro assays? *RSC Adv.* **2015**, *5*, 70787–70807. [[CrossRef](#)]
29. Al-Sharqi, A.; Apun, K.; Vincent, M.; Kanakaraju, D.; Bilung, L.M. Enhancement of the Antibacterial Efficiency of Silver Nanoparticles against Gram-Positive and Gram-Negative Bacteria Using Blue Laser Light. *Int. J. Photoenergy* **2019**, *2019*, 1–12. [[CrossRef](#)]
30. Chatterjee, T.; Chatterjee, B.K.; Majumdar, D.; Chakrabarti, P. Antibacterial effect of silver nanoparticles and the modeling of bacterial growth kinetics using a modified Gompertz model. *Biochim. Biophys. Acta Gen. Subj.* **2015**, *1850*, 299–306. [[CrossRef](#)]
31. Vila Domínguez, A.; Ayerbe Algaba, R.; Miró Canturri, A.; Rodríguez Villodres, Á.; Smani, Y. Antibacterial Activity of Colloidal Silver against Gram-Negative and Gram-Positive Bacteria. *Antibiotics* **2020**, *9*, 36. [[CrossRef](#)] [[PubMed](#)]
32. Xu, H.; Qu, F.; Xu, H.; Lai, W.; Andrew Wang, Y.; Aguilar, Z.P.; Wei, H. Role of reactive oxygen species in the antibacterial mechanism of silver nanoparticles on *Escherichia coli* O157:H7. *BioMetals* **2012**, *25*, 45–53. [[CrossRef](#)] [[PubMed](#)]

33. Quinteros, M.A.; Cano Aristizábal, V.; Dalmasso, P.R.; Paraje, M.G.; Páez, P.L. Oxidative stress generation of silver nanoparticles in three bacterial genera and its relationship with the antimicrobial activity. *Toxicol. Vitro* **2016**, *36*, 216–223. [[CrossRef](#)] [[PubMed](#)]
34. Ninganagouda, S.; Rathod, V.; Singh, D.; Hiremath, J.; Singh, A.K.; Mathew, J.; Ul-Haq, M. Growth Kinetics and Mechanistic Action of Reactive Oxygen Species Released by Silver Nanoparticles from *Aspergillus niger* on *Escherichia coli*. *Biomed. Res. Int.* **2014**, *2014*, 1–9. [[CrossRef](#)]
35. Korshed, P.; Li, L.; Liu, Z.; Mironov, A.; Wang, T. Size-dependent antibacterial activity for laser-generated silver nanoparticles. *J. Interdiscip. Nanomed.* **2019**, *4*, 24–33. [[CrossRef](#)]
36. Xiu, Z.; Ma, J.; Alvarez, P.J.J. Differential Effect of Common Ligands and Molecular Oxygen on Antimicrobial Activity of Silver Nanoparticles versus Silver Ions. *Environ. Sci. Technol.* **2011**, *45*, 9003–9008. [[CrossRef](#)]
37. Lee, S.; Jun, B.-H. Silver Nanoparticles: Synthesis and Application for Nanomedicine. *Int. J. Mol. Sci.* **2019**, *20*, 865. [[CrossRef](#)]
38. Schlemmer, W.; Fischer, W.; Zankel, A.; Vukušić, T.; Filipič, G.; Jurov, A.; Blažeka, D.; Goessler, W.; Bauer, W.; Spirk, S.; et al. Green Procedure to Manufacture Nanoparticle-Decorated Paper Substrates. *Materials (Basel)* **2018**, *11*, 2412. [[CrossRef](#)]
39. Ivanova, N.; Gugleva, V.; Dobрева, M.; Pehlivanov, I.; Stefanov, S.; Andonova, V. Silver Nanoparticles as Multi-Functional Drug Delivery Systems. In *Nanomedicines*; IntechOpen: London, UK, 2019; pp. 72–92.
40. Alenezi, H.; Cam, M.E.; Edirisinghe, M. Experimental and theoretical investigation of the fluid behavior during polymeric fiber formation with and without pressure. *Appl. Phys. Rev.* **2019**, *6*, 041401. [[CrossRef](#)]
41. Parhizkar, M.; Sofokleous, P.; Stride, E.; Edirisinghe, M. Novel preparation of controlled porosity particle/fibre loaded scaffolds using a hybrid micro-fluidic and electrohydrodynamic technique. *Biofabrication* **2014**, *6*, 45010. [[CrossRef](#)]
42. SCCS. Scientific Committee on Consumer Safety SCCS OPINION on Colloidal Silver (nano). In Proceedings of the SCCS, Luxembourg, 24–25 October 2018.
43. Committee, E.S. Guidance on the risk assessment of the application of nanoscience and nanotechnologies in the food and feed chain. *EFSA J.* **2011**, *9*, 2140. [[CrossRef](#)]
44. Bondarenko, O.; Juganson, K.; Ivask, A.; Kasemets, K.; Mortimer, M.; Kahru, A. Toxicity of Ag, CuO and ZnO nanoparticles to selected environmentally relevant test organisms and mammalian cells in vitro: A critical review. *Arch. Toxicol.* **2013**, *87*, 1181–1200. [[CrossRef](#)]
45. Krce, L.; Šprung, M.; Maravić, A.; Umek, P.; Salamon, K.; Krstulović, N.; Aviani, I. Bacteria Exposed to Silver Nanoparticles Synthesized by Laser Ablation in Water: Modelling *E. coli* Growth and Inactivation. *Materials (Basel)* **2020**, *13*, 653. [[CrossRef](#)]
46. Blažević, I.; Đulović, A.; Maravić, A.; Čikeš Čulić, V.; Montaut, S.; Rollin, P. Antimicrobial and Cytotoxic Activities of *Lepidium latifolium* L. Hydrodistillate, Extract and Its Major Sulfur Volatile Allyl Isothiocyanate. *Chem. Biodivers.* **2019**, *16*, e1800661. [[CrossRef](#)]
47. Rončević, T.; Krce, L.; Gerdol, M.; Pacor, S.; Benincasa, M.; Guida, F.; Aviani, I.; Čikeš-Čulić, V.; Pallavicini, A.; Maravić, A.; et al. Membrane-active antimicrobial peptide identified in *Rana arvalis* by targeted DNA sequencing. *Biochim. Biophys. Acta Biomembr.* **2019**, *1861*, 651–659. [[PubMed](#)]
48. Lee, M.-T.; Sun, T.-L.; Hung, W.-C.; Huang, H.W. Process of inducing pores in membranes by melittin. *Proc. Natl. Acad. Sci. USA* **2013**, *110*, 14243–14248. [[CrossRef](#)] [[PubMed](#)]
49. Rončević, T.; Vukičević, D.; Ilić, N.; Krce, L.; Gajski, G.; Tonkić, M.; Goić-Barišić, I.; Zoranić, L.; Sonavane, Y.; Benincasa, M.; et al. Antibacterial Activity Affected by the Conformational Flexibility in Glycine–Lysine Based α -Helical Antimicrobial Peptides. *J. Med. Chem.* **2018**, *61*, 2924–2936. [[CrossRef](#)] [[PubMed](#)]
50. Stiefel, P.; Schmidt-Emrich, S.; Maniura-Weber, K.; Ren, Q. Critical aspects of using bacterial cell viability assays with the fluorophores SYTO9 and propidium iodide. *BMC Microbiol.* **2015**, *15*, 36. [[CrossRef](#)] [[PubMed](#)]
51. Seaver, L.C.; Imlay, J.A. Hydrogen Peroxide Fluxes and Compartmentalization inside Growing *Escherichia coli*. *J. Bacteriol.* **2001**, *183*, 7182–7189. [[CrossRef](#)] [[PubMed](#)]
52. Kalyanaraman, B.; Darley-Usmar, V.; Davies, K.J.A.; Dennery, P.A.; Forman, H.J.; Grisham, M.B.; Mann, G.E.; Moore, K.; Roberts, L.J.; Ischiropoulos, H. Measuring reactive oxygen and nitrogen species with fluorescent probes: Challenges and limitations. *Free Radic. Biol. Med.* **2012**, *52*, 1–6.

53. Aranda, A.; Sequedo, L.; Tolosa, L.; Quintas, G.; Burello, E.; Castell, J.V.; Gombau, L. Dichloro-dihydro-fluorescein diacetate (DCFH-DA) assay: A quantitative method for oxidative stress assessment of nanoparticle-treated cells. *Toxicol. Vitro* **2013**, *27*, 954–963. [[CrossRef](#)] [[PubMed](#)]
54. Matharu, R.K.; Tabish, T.A.; Trakoolwilaiwan, T.; Mansfield, J.; Moger, J.; Wu, T.; Lourenço, C.; Chen, B.; Ciric, L.; Parkin, I.P.; et al. Microstructure and antibacterial efficacy of graphene oxide nanocomposite fibres. *J. Colloid Interface Sci.* **2020**, *571*, 239–252. [[PubMed](#)]
55. Chopinet, L.; Formosa, C.; Rols, M.P.; Duval, R.E.; Dague, E. Imaging living cells surface and quantifying its properties at high resolution using AFM in QITM mode. *Micron* **2013**, *48*, 26–33. [[CrossRef](#)] [[PubMed](#)]
56. Radmacher, M. Studying the Mechanics of Cellular Processes by Atomic Force Microscopy. In *Methods in Cell Biology*; Academic Press: Cambridge, MA, USA, 2007; Volume 83, pp. 347–372. ISBN 0123705002.
57. Gaboriaud, F.; Parcha, B.S.; Gee, M.L.; Holden, J.A.; Strugnell, R.A. Spatially resolved force spectroscopy of bacterial surfaces using force-volume imaging. *Colloids Surfaces B Biointerfaces* **2008**, *62*, 206–213. [[CrossRef](#)] [[PubMed](#)]
58. Bailey, R.G.; Turner, R.D.; Mullin, N.; Clarke, N.; Foster, S.J.; Hobbs, J.K. The Interplay between Cell Wall Mechanical Properties and the Cell Cycle in *Staphylococcus aureus*. *Biophys. J.* **2014**, *107*, 2538–2545. [[CrossRef](#)] [[PubMed](#)]
59. Tuson, H.H.; Auer, G.K.; Renner, L.D.; Hasebe, M.; Tropini, C.; Salick, M.; Crone, W.C.; Gopinathan, A.; Huang, K.C.; Weibel, D.B. Measuring the stiffness of bacterial cells from growth rates in hydrogels of tunable elasticity. *Mol. Microbiol.* **2012**, *84*, 874–891. [[CrossRef](#)]
60. Kostylev, M.; Otwell, A.E.; Richardson, R.E.; Suzuki, Y. Cloning Should Be Simple: *Escherichia coli* DH5 α -Mediated Assembly of Multiple DNA Fragments with Short End Homologies. *PLoS ONE* **2015**, *10*, e0137466. [[CrossRef](#)]
61. Hanahan, D.; Jessee, J.; Bloom, F.R. Plasmid transformation of *Escherichia coli* and other bacteria. *Methods Enzymol.* **1991**, *204*, 63–113.
62. Panja, S.; Aich, P.; Jana, B.; Basu, T. How does plasmid DNA penetrate cell membranes in artificial transformation process of *Escherichia coli*? *Mol. Membr. Biol.* **2008**, *25*, 411–422. [[CrossRef](#)]
63. Datey, A.; Subburaj, J.; Gopalan, J.; Chakravorty, D. Mechanism of transformation in *Mycobacteria* using a novel shockwave assisted technique driven by in-situ generated oxyhydrogen. *Sci. Rep.* **2017**, *7*, 8645.
64. Mathelié-Guinlet, M.; Grauby-Heywang, C.; Martin, A.; Février, H.; Moroté, F.; Vilquin, A.; Béven, L.; Delville, M.-H.; Cohen-Bouhacina, T. Detrimental impact of silica nanoparticles on the nanomechanical properties of *Escherichia coli*, studied by AFM. *J. Colloid Interface Sci.* **2018**, *529*, 53–64. [[CrossRef](#)] [[PubMed](#)]



© 2020 by the authors. Licensee MDPI, Basel, Switzerland. This article is an open access article distributed under the terms and conditions of the Creative Commons Attribution (CC BY) license (<http://creativecommons.org/licenses/by/4.0/>).

V. CONCLUSIONS

The topic of the papers that are included in this study can be divided into three parts: modelling bacterial growth curves, experimental characterization of the produced colloid and probing the mode of antibacterial action of laser-synthesized AgNPs.

Firstly, it was necessary to understand the growth and inactivation of viable bacterial cells. Understanding this growth enables recognizing, describing and explaining population growth/inactivation features obtained when the cells are treated with AgNPs. For that reason, viable *E. coli* growth data were obtained by measuring the time change of the optical density of the sample, for different initial nutrients concentrations and different inoculum sizes.

Our data showed that the main effect of the inoculum change is a shift of the growth curve along the time axis without affecting the overall curve shape while growth stop is caused by a lack of nutrients governing maximal cell concentration. The variation of inoculum and initial nutrients concentration did not induce a lag phase. The absence of a lag phase is a convenient starting point for studying the influence bactericide has on inducing a lag phase. The simple interaction-based *E. coli* growth model was developed and applied to the acquired data.

The bacterial population is described by the two mutually dependent first-order nonlinear differential equations which constitute the model. These equations give the time change of bacteria and nutrients concentrations. The introduction of a negative bacterium–bacterium interaction term, leading to population decay, is specific for our model. This is a novel mathematical approach for describing bacterial inactivation and the onset of the death phase which can be explained on a microscopic basis. The model can easily be extended to include additional bacterial interactions. Furthermore, a simple method for data analysis and identifying model parameters is given. This method can be used by researchers possessing minimum mathematical skills.

The silver nanoparticle colloid was synthesized using laser ablation in deionized water. XRD, DLS, AFM, TEM, UV–VIS and zeta potential measurements were performed to determine the NPs composition, structure, size, concentration and stability. The concentration of the AgNPs in the colloid was estimated from the volume of the LAL-ejected material. The colloid was tested against *E. coli* cells which showed sensitivity towards it. Growth curves of bacteria treated with sub-lethal and lethal AgNP concentrations were obtained from OD measurements.

The main effects of the AgNP treatment are an increase in the baseline of the bacterial growth curve, increase in apparent lag time, reduction of the maximal OD, without significant change to the growth rate. Growth curves of bacteria treated with higher sub-lethal concentrations exhibit a minimum, before exponential growth prevails.

To analyze the obtained data, a novel growth model is designed as an extension of our interaction-based model for non-treated cells. The main assumption of the model is that treated bacteria uptake nanoparticles, resulting in a decrease of both nanoparticles and bacteria concentrations. The time change of bacterial, nutrients, and nanoparticles concentrations depends on strengths of the bacteria–nutrients, bacteria–bacteria, and bacteria–nanoparticles interactions.

Experimental growth data reflect the concentration of both bacterial cells and nanoparticles which in turn shows that, for lethal treatment, a decrease in OD mostly reflects a change in nanoparticle concentration.

The model comprehensively describes concentration-dependent postponed growth, with very good fits for the apparent lag and exponential phase. It also describes the concentration-dependent reduction of the maximal population, and the decrease of the bacterial population in the death phase. According to the model, the postponed exponential growth is not due to a classic lag in which bacteria do not divide. This state can be characterized as a dynamic lag phase, or a near-steady state for which the bacterial growth rate is close to the bacterial death rate. In the lag phase, bacteria divide due to nutrients consumption and are inactivated due to the uptake of silver nanoparticles, all at the same time. The duration of the dynamic lag time increases with nanoparticle concentration and becomes infinite at the lethal concentration, representing a transition between bacterial life and death conditions.

To summarize, the main contributions of modelling AgNP-treated bacteria growth curves can be emphasized as follows. The observed lag phase induced by AgNPs is not postponed bacterial growth and the predominant mode of antibacterial action of laser-synthesized AgNPs is AgNP penetration inside the cell.

The experimental probing of the AgNP bactericidal mechanism was mostly done using the obtained fluorescence data and AFM data. The findings indicate that some non-viable AgNP-treated *E. coli* cells are not membrane-permeabilized, leading to the conclusion that permeabilization of the membrane might not be the only killing mechanism.

The change in bacterial ROS levels during AgNP treatment was obtained from the DCF fluorescence signal. Two experiments were performed to resolve the cellular ROS from

the total fluorescence signal: for different concentrations of AgNPs in dyed PBS without bacteria and for the same samples but inoculated with *E. coli* cells. The results show that the fluorescence signal increases in time but reduces with nanoparticle concentration. When eliminating the contribution of the probe autooxidation, these results can be explained in terms of the nanoparticle double effect. Specifically, AgNPs stimulate cellular ROS production which increases the fluorescence signal, but they also absorb and scatter the incident/emitted light which results in signal reduction. The findings also show that non-treated bacteria do not produce ROS and the influence of AgNPs on autooxidation of the dye is negligible. A decrease in the fluorescence signal, occurring when AgNPs are added to the non-inoculated batch, appears because of light absorption and scattering from the nanoparticles.

This careful analysis of data enables extraction of the cellular ROS level from the total fluorescence signal. The obtained cellular ROS level is dose- and time-dependent. Given the fact that ROS assumes the highest level for the sub-lethal dose, we conclude that ROS-induced oxidative stress is not the predominant antibacterial mode of action of LAL-synthesized AgNPs against *E. coli*.

YM data were obtained from the force–distance curves measured at the topmost parts of bacteria. The findings show that the distribution of the YM data of untreated *E. coli* cells is bimodal, which is particularly interesting. The distribution has two clearly split maxima that differ in value by an order of magnitude. The softer regions are randomly distributed on the cell surface.

During AgNP treatment, bacterial YM histograms reveal the narrowing of the stiffer YM maximum and its softening, i.e., a shift towards the lower values, possibly indicating a reduction of metabolic activity. YM data of treated cells also reveal softer regions next to the cells, which may be an indicator of intracellular matter leaking due to cell lysis. Bright-field microscopy of treated cells shows that cell growth does not cease immediately upon treatment. This finding is in line with the dynamic nature of the population lag as reported in the model on AgNP-treated *E. coli* growth, which assumes that cells which have not been inactivated continue to grow.

To summarize, our results indicate that the mode of AgNP antibacterial action is an interplay of multiple factors. The LAL-synthesized AgNP bactericidal mechanism includes AgNP penetration inside the membrane/cell, destabilization of the cell membrane, including a reduction of its YM and possible cell leakage, with an increase in the cellular ROS level.

VI. APPENDIX

SUPPLEMENTARY MATERIAL TO CHAPTER II

E. coli DH5 α strain was grown overnight at 37 °C with shaking in 50 % Mueller-Hinton Broth (MHB) broth (Biolife, Italy), while *E. coli* ATCC 29213 was grown in 50 % Luria-Bertani (LB) medium (5.0 g/L of tryptone, 2.5 g/L of yeast extract and 5.0 g/L of NaCl per 1 liter of deionized sterile water) in the same conditions. The following steps were done in the same way as describes in the Methods section in the paper. The experiments were done in triplicates.

Viable cell count of *E. coli* ATCC 29213 growing in 50 % LB was done as described in the paper. The experiments were done in triplicates.

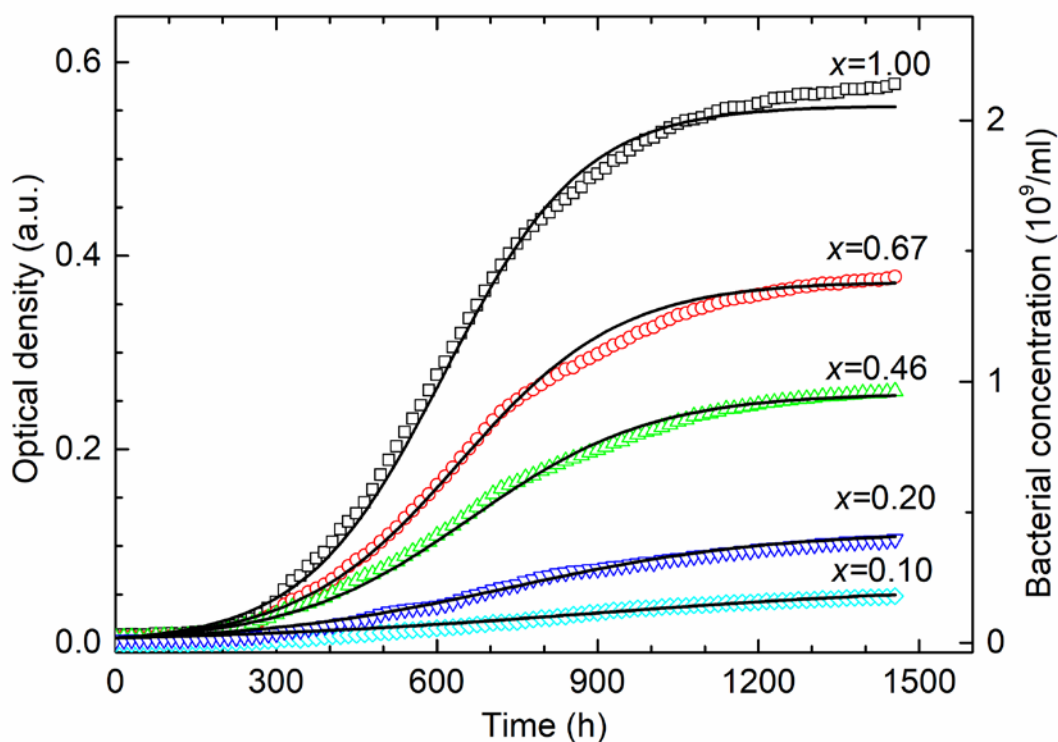


Fig S1. DH5 α in MHB: different initial nutrients concentration. Growth curves of *E. coli* DH5 α in 50 % MHB obtained for different initial dilution factors x but with the same inoculum size. The presented curves are the average of OD data obtained from three separate experiments, conducted under the same conditions. Symbols are the experimental data and full lines are the theoretical fits. The OD in absorbance units is given on the left axis and the corresponding bacterial concentrations in CFU/ml are given on the right axes.

Fig S1 shows experimental and theoretical growth curves of *E. coli* DH5 α in 50 % MHB obtained for different initial concentrations of nutrients N_0 , i.e. different initial nutrients dilution factors x . The experimental growth curves are given by symbols. Bacterial concentration in CFU/ml is given on the right axes. The baseline, i.e. OD of

the vial and the corresponding sterile growth medium, is subtracted from the raw data so that the OD reflects only the change in the bacterial concentration. It can be noted that the maximum of bacterial OD, as well as the growth rate follow the reduction of the nutrients concentration in the same way as they do for *E. coli* DH5 α in 50 % LB. The lines are the best fits obtained from the solutions of model equations (1) and (2). The fitting procedure requires variation of the four parameters: $B_0 = 0.005$ a.u., $N_M = 0.55$ a.u., α and β . The fitting procedure was done as explained in the paper. The figure shows that the cells have not gone into the stationary or the mortality phase within the first 24 hours. For this reason, β parameter was taken to be zero for these fits. Interaction strength parameters α was obtained as described in the paper. As seen in the figure, these theoretical curves follow the experimental data very well.

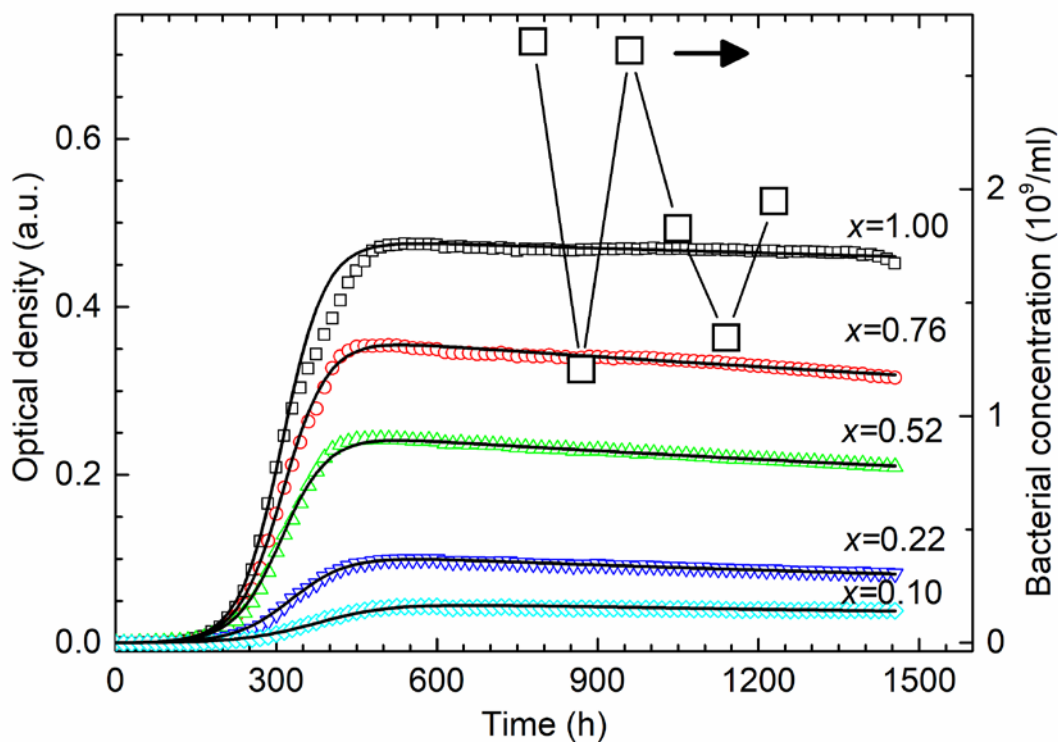


Fig S2. ATCC 29213 in LB: different initial nutrients concentration. Growth curves of *E. coli* ATCC 29213 in 50 % LB obtained for different initial dilution factors x but with the same inoculum size. The presented curves are the average of OD data obtained from three separate experiments, conducted under the same conditions. Smaller symbols are the experimental OD data and full lines are the theoretical fits. Larger symbols are the viable cell count data. The OD in absorbance units is given on the left axis and the corresponding bacterial concentrations in CFU/ml are given on the right axes.

Fig S2 shows growth curves of *E. coli* ATCC 29213 in 50 % LB obtained for different initial concentrations of nutrients N_0 , i.e. different initial nutrients dilution factors x . The experimental data manipulation and the fitting procedure was as previously explained. Once again it can be noted that the maximum of bacterial OD, as well as the growth rate follow the reduction of the initial nutrients concentration in the same way as they do for the data given above. The initial fitting parameters were: $B_0 = 0.0002$ a.u. and $N_M = 0.55$ a.u. This figure shows that this strain in these growing conditions undergoes the death phase after approximately 8 hours. The fits of the experimental data (given by solid lines) explain the experimental growth (given by symbols) curves nicely. In order to inspect the viability of the cells in the death phase, viable cell counting assay was performed. These data are presented by large squares in the figure. The viable cell data follow the same trend as the OD data even though they are somewhat dispersed around the OD curve since the OD measurements are much more precise.

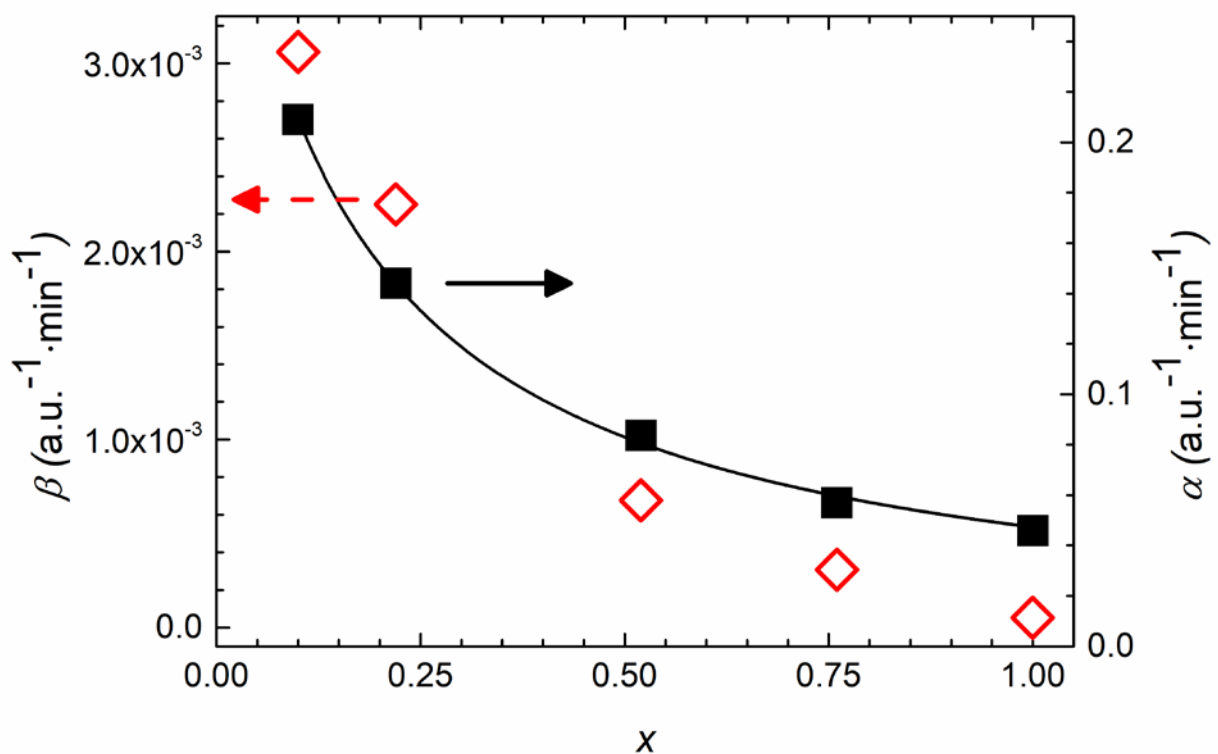


Fig S3. ATCC 29213 in LB: interaction strength parameters. Interaction strength parameters α and β for *E. coli* ATCC 29213 in 50 % LB. Bacterial interaction strength parameter β (open diamonds and left axis), as function of the initial nutrients dilution factor x obtained as described in the paper. Parameter α as a function of x (full squares and right axis) is presented for comparison. The full line is the fit of β and α to a rational function.

In order to further validate the model, interaction strength parameters α and β of *E. coli* ATCC 29213 in 50 % LB for different initial nutrients dilution factors x were obtained according to the described procedure. The data shows that the interaction strength parameter $\beta(x)$ strongly decreases with x , with the dependence very similar to the concentration dependence of parameter $\alpha(x)$ as shown in Fig S3 in the appropriate scale. These data were fitted to the same rational function $f(x) = a / (x_{1/2} + x)$ as given in the paper. The functions for α and β differ only in the value of the parameter a . The full line in Fig S3 is the least-square fit of parameter $\alpha(x)$. This fit yielded: $a = 5.51 \cdot 10^{-2} \text{ min}^{-1} \text{ a.u.}^{-1}$, $a' = 7.45 \cdot 10^{-4} \text{ min}^{-1} \text{ a.u.}^{-1}$ and $x_{1/2} = 0.163$.

SUPPLEMENTARY MATERIAL TO CHAPTER III

We further analyze the system for $\beta = 0$. By inserting equations (2) and (3) into (1), we obtain the expression for the growth capacity of the habitat which is constant in time:

$$\frac{d}{dt} [B(t) + N(t) - P(t)] = 0 \quad (1')$$

$$B(0) + N(0) - P(0) = B(t) + N(t) - P(t) \quad (2')$$

Combination of equations (2) and (3), and integration, gives the relationship between the nutrients and the nanoparticles concentrations:

$$N(t) = N(0) \cdot \left(\frac{P(t)}{P(0)}\right)^{\frac{\alpha}{\gamma}}. \quad (3')$$

As seen in Figures 7 a) and 7 b), by increasing the initial nanoparticles concentration of the batch, $B(t)$ develops a broad minimum which moves to the right on the time axis. Let τ be the time at which the curves reach its minimum. At the minimum, for $t = \tau$, $\frac{d}{dt} B(t) = 0$ is valid and equation (1') becomes

$$\frac{d}{dt} N(t) = \frac{d}{dt} P(t). \quad (4')$$

After inserting equations (2) and (3) into (4'), we obtain the relationship between the nutrients and the nanoparticles concentrations at the minimum

$$N(\tau) = \frac{\gamma}{\alpha} \cdot P(\tau), \quad (5')$$

which combined with (3') gives the nanoparticles concentration at the minimum

$$P(\tau) = \left[\frac{\gamma}{\alpha} \cdot \frac{P(0)^{\frac{\alpha}{\gamma}}}{N(0)} \right]^{\frac{\gamma}{\alpha-\gamma}}. \quad (6')$$

Finally, after inserting (5') and (6') into (2'), for $t = \tau$, equation (2') reads

$$B_0 + N_M(1 - v) - P_M \cdot v = B(\tau) + \left(\frac{\gamma}{\alpha(v)} - 1\right) \cdot \left[\frac{\gamma}{\alpha(v)} \cdot \frac{(P_M \cdot v)^{\frac{\alpha(v)}{\gamma}}}{N_M(1-v)} \right]^{\frac{\gamma}{\alpha(v)-\gamma}}, \quad (7')$$

For known $B(\tau)$ this equation can be numerically solved for v .

The first solution is $v_1 = 0.186$ is found for $\tau = 0$ and $B(\tau) = B_0$. The second solution, $v_2 = 0.345$ for $\tau = \infty$ and $B(\tau) = 0$. We conclude that with the nanoparticles volume share increase, for $v \in [0.186, 0.345]$ and $t = \tau$, a minimum in $B(t)$ is developed, where the dynamic lag time is increasing and assumes infinite value for $v = v_2$. The volume share v_2 is the calculated lethal dosage which is in excellent accordance with the experimental value.

CURRICULUM VITAE

LUCIJA KRCE

Date of birth: 27.09.1985.

Place of birth: Split, Croatia

Nationality: Croatian

EMPLOYMENT

2013-present Teaching assistant, Faculty of Science, University of Split

EDUCATION

2013-present Doctoral program in Biophysics, Faculty of Science, University of Split

2004-2011. Magister of physics, Faculty of Science, University of Split

PUBLICATION LIST**LUCIJA KRCE**

- [1] Krce L, Šprung M, Rončević T, Maravić A, Čikeš Čulić V, Blažeka D, Krstulović N, Aviani I. Probing the Mode of Antibacterial Action of Silver Nanoparticles Synthesized by Laser Ablation in Water: What Fluorescence and AFM Data Tell Us. *Nanomaterials* 2020;10:1040. <https://doi.org/10.3390/nano10061040>.
- [2] Krce L, Šprung M, Maravić A, Umek P, Salamon K, Krstulović N, Aviani I. Bacteria Exposed to Silver Nanoparticles Synthesized by Laser Ablation in Water: Modelling *E. coli* Growth and Inactivation. *Materials (Basel)* 2020;13:653. <https://doi.org/10.3390/ma13030653>.
- [3] Krce L, Šprung M, Maravić A, Aviani I. A simple interaction-based *E. coli* growth model. *Phys Biol* 2019;16:066005. <https://doi.org/10.1088/1478-3975/ab3d51>.
- [4] Maravić A, Rončević T, Krce L, Ilić N, Galić B, Čulić Čikeš V, Carev I. Halogenated boroxine dipotassium trioxohydroxytetrafluorotriborate K₂ [B₃O₃F₄OH] inhibits emerging multidrug-resistant and β -lactamase-producing opportunistic pathogens. *Drug Dev Ind Pharm* 2019;0:1–7. <https://doi.org/10.1080/03639045.2019.1656736>.
- [5] Rončević T, Vukičević D, Krce L, Benincasa M, Aviani I, Maravić A, Tossi A. Selection and redesign for high selectivity of membrane-active antimicrobial peptides from a dedicated sequence/function database. *Biochim Biophys Acta - Biomembr* 2019;1861:827–34. <https://doi.org/10.1016/j.bbamem.2019.01.017>.
- [6] Rončević T, Krce L, Gerdol M, Pacor S, Benincasa M, Guida F, Aviani I, Čikeš-Čulić V, Pallavicini A, Maravić A, Tossi A. Membrane-active antimicrobial peptide identified in *Rana arvalis* by targeted DNA sequencing. *Biochim Biophys Acta - Biomembr* 2019;1861:651–9. <https://doi.org/10.1016/j.bbamem.2018.12.014>.
- [7] Bazina L, Maravić A, Krce L, Soldo B, Odžak R, Popović VB, Aviani I, Primožič I, Šprung M. Discovery of novel quaternary ammonium compounds based on

- quinuclidine-3-ol as new potential antimicrobial candidates. *Eur J Med Chem* 2019;163:626–35. <https://doi.org/10.1016/j.ejmech.2018.12.023>.
- [8] Rončević T, Vukičević D, Ilić N, Krce L, Gajski G, Tonkić M, Goić-Barišić I, Zoranić L, Sonavane Y, Benincasa M, Juretić D, Maravić A, Tossi A. Antibacterial Activity Affected by the Conformational Flexibility in Glycine–Lysine Based α -Helical Antimicrobial Peptides. *J Med Chem* 2018;61:2924–36. <https://doi.org/10.1021/acs.jmedchem.7b01831>.

